MODELING AND SIMULATION OF OXIDATIVE COUPLING OF METHANE IN A HEAT-EXCHANGE INTEGRATED MICROCHANNEL REACTOR

by

Funda İdil Tezcan

B.S., Chemical Engineering, Boğaziçi University, 2011

Submitted to the Institute for Graduate Studies in
Science and Engineering in partial fulfillment of
the requirements for the degree of
Master of Science

Graduate Program in Chemical Engineering

Boğaziçi University

2013

MODELING AND SIMULATION OF OXIDATIVE COUPLING OF METHANE IN A HEAT-EXCHANGE INTEGRATED MICROCHANNEL REACTOR

APPROVED BY:

Assoc. Prof. Ahmet Kerim Avcı .....

(Thesis Supervisor)

Assoc. Prof. Hasan Bedir .....

Prof. Ramazan Yıldırım .....

DATE OF APPROVAL: 23.08.2013

ACKNOWLEDGEMENTS

I would like to express my deepest thanks to my supervisor Assoc. Prof. Ahmet Kerim Avcı, for his support, encouragement and guidance which always comforted me throughout my study. I am very grateful to have the opportunity to work with him.

I also would like to thank my committee members, Prof. Ramazan Yıldırım and Assoc. Prof. Hasan Bedir for devoting their valuable time to read and comment on my thesis.

I want to express my blessings to İrem Şen for helping me with my research, answering all of my questions with endless patience and teaching me everything I needed for my thesis. I feel grateful to share a working environment with her and witness her positive energy and encouragement.

My special thanks go to Hayri Onur Kavaklı, my best friend, for being there whenever I need him. Without his fellowship, it would have been much harder to leave behind the challenges that I have been through. I am so happy for sharing every moment of my life with him.

I want to thank my mates Can Ekici and Didem Büşra Kabakçı from KB 404 for their friendship. Without them, working in the laboratory wouldn't have been so much fun. I would like to thank the people who make each day in KB more enjoyable, especially Oya Gürsoy Yılmaz, Erge Akbaş, Melis Yıldırım, Serhat Erşahin and Cihan Kaya.

I want to thank my dorm mate Ş. İrem Tatar for her friendship where we share joys, sorrows and pastimes. With her presence, each day in room 410-A have been more enjoyable. I was so lucky to share the two years of my life with her and feel her support at every moment for better or for worse. I also want to express my gratitude to Gizem Sarpça and Sinan Baysal for being my precious friends. Their fellowships have been my biggest motivation and source of energy during my graduate years.

These paragraphs are not enough to express my blessings to my mother Füsun and my father Mustafa. I just want to thank them for their unconditional love, support and patience. I

want to thank my twin sisters İlay and Ayda with all my heart for being the light of my life. I desperately miss them while they are turning into such great individuals but I never stopped feeling their love and support even when I am miles away from home. This thesis is dedicated to my family.

Finally, I would like to acknowledge Boğaziçi University Research Fund for financial support they provided through the project BAP-6349.

ABSTRACT

MODELING AND SIMULATION OF OXIDATIVE COUPLING OF METHANE IN A HEAT-EXCHANGE INTEGRATED MICROCHANNEL REACTOR

Oxidative coupling of methane (OCM) involves catalytic conversion of methane into C_2 hydrocarbons (ethane and ethylene) and offers an alternative oil-free production of important feedstock used in petrochemical industry. OCM requires effective temperature control since the product distribution depends strongly on temperature. Integration of OCM with microchannel reactor technology can lead to a novel process, since the micro-technology has advantages like significant intensification of the process which minimizes the transport resistances and allows robust temperature control. The aim of this study is to investigate OCM in a cooling flow enabled heat-exchange integrated microchannel reactor by computer-based modeling and simulation techniques, and to demonstrate the effects of different operational and structural parameters on the reaction performance by means of temperature profile and C_2 hydrocarbon yield. Steady-state simulations conducted using computational fluid dynamics (CFD) show that effective heat transfer and improved temperature distributions can be obtained in the microchannel reactor. The results indicate that, using walls with high thermal conductivity regulates temperature profile and improves the C_2 hydrocarbon yield at the same time. Using thicker walls increases the average reaction temperature, but decreases the C_2 hydrocarbon yield. It is observed that increasing the molar methane-to-oxygen ratio in the feed decreases the reaction temperature and conversion immediately due to reduced release of exothermal heat, resulting in lower C_2 hydrocarbon yield. In contrast with the cooling channel inlet temperature, reaction channel inlet temperature has much lower effect on temperature profile. It is also observed that increasing the mass flow rate of cooling channel decreases the reaction temperature and increases the C_2 hydrocarbon yield, whereas increasing the mass flow rate of the reaction channel has the opposite effect on the reaction temperature profile, leading to the oxidation of C_2 hydrocarbons. The possibility of obtaining 46.8% methane conversion and 23.9% C_2 yield is demonstrated.

ÖZET

METANIN OKSİJEN VARLIĞINDA KATALİTİK OLARAK YÜKSEK MOLEKÜLLÜ BİLEŞENLERE DÖNÜŞTÜRÜLMESİ REAKSİYONUNUN ISI DEĞİŞTİRİCİ ÖZELLİKLİ BİR MİKROKANAL REAKTÖRDE MODELLENMESİ VE BENZETİMİ

Metanın oksijen varlığında katalitik olarak yüksek moleküllü bileşenlere dönüştürülmesi reaksiyonu, metanın katalitik olarak etan ve etilen hidrokarbonlarına dönüştürülmesini içerir ve petrokimyasal endüstrilerinde kullanılan hammaddelerin alternatif petrolsüz üretimini sunar. Ürün dağılımı yüksek oranda sıcaktığa bağlı olduğundan, bu reaksiyon etkili sıcaklık kontrolü gerektirir. Bu reaksiyonun mikrokanal reaktör teknolojisi ile bütünleşmesi, mikrokanal reaktörlerin prosesi önemli ölçüde yoğunlaştırarak ulaşım direncini düşürme ve güçlü sıcaklık kontrolü sağlama gibi avantajları sayesinde yenilikçi bir proses ortaya çıkarır. Bu çalışmanın amacı, bu reaksiyonu hesaplamalı olarak bir soğutma akışı varlığında, ısı değiştirici özellikli bir mikrokanal reaktörde modellemek ve farklı operasyonel ve yapısal parametrelerin reaksiyon performansı üzerindeki etkilerini göstermektir. Hesaplamalı kararlı-hal benzetmeleri, mikrokanal reaktörlerde etkili ısı transferinin ve geliştirilmiş sıcaklık dağılımının elde edilebileceğini göstermektedir. Sonuçlara göre, ısı iletkenliği yüksek duvar kullanmak sıcaklık profilini düzenlemekte ve ürün verimini geliştirmektedir. Daha kalın duvar kullanmak ortalama reaksiyon sıcaklığını yükseltmekte fakat ürün verimini düşürmektedir. Reaksiyon girişindeki molar metan/oksijen oranını arttırmak, indirgenmiş ekzotermik ısı çıkışı nedeniyle reaksiyon sıcaklığını ve reaktant dönüşümünü düşürmektedir, bu da ürün verimini azaltmaktadır. Soğutma kanalı giriş sıcaklığının tam tersine, reaksiyon kanalı giriş sıcaklığının reaksiyon sıcaklığı profiline etkisi çok azdır. Soğutma kanalı akış hızının arttırılması reaksiyon sıcaklığını azaltıp ürün verimini arttırır iken, reaksiyon kanalı akış hızının arttırılmasının sıcaklık profili üzerinde tersi etkiye sahip olduğu ve ürünlerin oksidasyonuna neden olduğu gözlenmiştir. 46.8% metan dönüşümü ile 23.9% ürün veriminin elde edildiği gösterilmiştir.

TABLE OF CONTENTS

LIST OF FIGURES

LIST OF TABLES

LIST OF SYMBOLS

A_s	Active surface area of catalytic washcoat in channel (m^{-1})
$D_{eff,i,m}$	Effective diffusivity of species *i* in the mixture ($m^2\ s^{-1}$)
$D_{i,m}$	Diffusivity of species *i* in the mixture ($m^2\ s^{-1}$)
c_{p_f}	Heat capacity of the fluid ($J\ kg^{-1}\ K^{-1}$)
E_a	Activation energy ($kJ\ mol^{-1}$)
F_i	Molar flow rate of the species *i* ($kmol\ s^{-1}$)
$\vec{\mathbf{F}}$	Momentum source/sink term ($kg\ m^{-2}\ s^{-2}$)
$\vec{g}$	Gravitational acceleration ($m\ s^{-2}$)
H	Height of the microchannel (m)
h_i	Sensible enthalpy of species *i* in channel ($J\ kg^{-1}$)
I	Unit tensor
i	Species index
j	Reaction number, channel index
$\vec{J_i}$	Fickian diffusive mass flux
k	Thermal conductivity
$k_{0,j}$	Pre-exponential factor for reaction *j*
$k_{eff,j}$	Effective thermal conductivity of the fluid ($W\ m^{-1}\ K^{-1}$)
k_s	Index for the surface reaction
k_v	Index for the volumetric reaction
K_{j,CO_2}	Adsorption constant for CO_2 in reaction *j* (Pa^{-1})
L	Length of the microchannel (m)
M_i	Molecular weight of species i ($kg\ mol^{-1}$)
m_j	Reaction order
$\vec{n}$	Normal vector unit
n_j	Reaction order
q''	Heat flux ($W\ m^{-2}$)
R	Universal gas constant ($J\ mol^{-1}\ K^{-1}$)
r_j	Rate of j^{th} reaction ($kmol\ m^{-3}\ s^{-1}$)
$R_{k_v}^v$	Rate of $k_v{}^{th}$ volumetric reaction ($mol\ m^{-3}\ s^{-1}$)

$R_{k_s}^s$	Rate of $R_{k_s}^s$ th surface reaction (mol m^{-2} s^{-1})
S_i	Selectivity of species *i*
S	Source of energy
T	Temperature
v	Velocity (m s^{-1})
$\vec{\mathbf{v}}$	Velocity field (m s^{-1})
W	Width of the microchannel (m)
X_{CH4}	Methane conversion
x, y, z	Cartesian coordinates (m)
Y_i	Yield of species *i*
Y_i	Mass fraction of species *i*
α	Permeability of the catalytic washcoat in channel (m^2)
ΔH_{298}^0	Standard enthalpy of reaction (kJ mol^{-1})
$\Delta H_{ad,CO_{2,j}}$	Adsorption enthalpy for CO_2, (J mol^{-1})
$\Delta H_{ad,O_{2,j}}$	Adsorption enthalpy for O_2, (J mol^{-1})
ϵ	Porosity of catalyst in channel
μ	Viscosity (kg m^{-1} s^{-1})
ρ_f	Fluid density (kg m^{-3})
$\bar{\bar{\tau}}$	Stress tensor due to flow (kg m^{-2} s^{-2})

LIST OF ACRONYMS/ABBREVIATIONS

2D	Two Dimensional
ad	Adsorption
CFD	Computational Fluid Dynamics
CH_4/O_2	Molar methane-to-oxygen ratio at the reactor inlet
cooling	Cooling channel
DMR	Dense Membrane Reactor
ENM	Enamel
FBR	Fixed Bed Reactor
in	Inlet
MIEMR	Mixed Ionic and Electronic conducting Membrane Reactors
OCM	Oxidative Coupling of Methane
PMR	Porous Membrane Reactor
rxn	Reaction channel
SOFCR	Solid Oxide Fuel Cell Reactors

1. INTRODUCTION

Crude oil being the essential source of energy has a vital importance for the continuity of our daily life. With the transportation advantage, crude oil replaced the application of coal and triggers the growth of industrialization decades ago. It is functional, global and incredibly valuable. However, it is expected that the remaining oil reserves will be insufficient to meet the ongoing needs by year of 2050 [1]. The quality of crude oil gets lower day by day, while the depletion of sources makes oil more expensive at the same time. Therefore, finding synthesis methods and implementing processes to create higher hydrocarbons from resources other than crude oil, such as natural gas, become critical for meeting increasing demands on energy. Considering the fact that natural gas is much cheaper than crude oil, method to convert natural gas, i.e. methane, to value added products seems to be a promising option for addressing the problems associated with crude oil.

Oxidative coupling of methane (OCM) to C_2-hydrocarbons is one of the alternative methods offering oil-free production of ethylene, a critical feedstock for petrochemical industries which is normally produced by steam cracking. Many scientific researches have been done in order to improve the exothermic catalytic OCM reaction since early 1980s [2]. The main challenge of OCM is to get ethylene, an intermediate species, as a product before it decomposes further into steam and carbon dioxide. This challenge can potentially be overcome by effective control of the reaction temperature. As the temperature rises, the degree of methane conversion increases. Due to the higher reactivity of C_2 products as compared with methane, combustion of C_2-hydrocarbons becomes the main route of CO_x formation [2]. Another way to produce ethylene is to run the operation at very short and narrow residence times, so that its decomposition into the products of oxidation is minimized. Considering these requirements, process intensification by using microchannel reactors which offer improved temperature control over the reactor with narrow residence time distributions can lead to increased ethylene selectivity, which is still a major challenge in conventional packed-bed reactors.

Process intensification is an innovative concept which aims to optimize energy, capital and safety by radical reduction in the physical size of the process. One of the ways of

intensification is to employ micro-structured equipments such as microchannel reactors and heat exchangers. In microchannel reactors, which have channels of sizes in the range of 10^{-4} to 10^{-3} m, heat and mass transfer rates are significantly improved with high surface area-to-volume ratios in the range of 10,000 to 50,000 m^2/m^3 [3]. Since the flow is laminar due to very small channel diameters, pressure drop is usually very small, and, therefore, millisecond contact times can be achieved. This configuration also favors narrow residence time distributions. Catalyst is usually incorporated to the reactor by coating it onto the inner channel walls. These advantages of microchannel units offer running the operation at short contact times with a well-defined flow distribution, and achieving effective temperature control over the reaction system, all of which are expected to favor ethylene selectivity in OCM. Ideal scale-up performance of the microchannel reactors is another feature which is attractive for the OCM process. Among all the research done for OCM in the past, there is no study other than the implementation of laboratory scale test reactors. Scale-up of the laboratory scale reactors causes significant performance loss for OCM. However, in microchannel technology, scaling-up is done simply by "numbering-up" of the unit cells, with identical channel hydrodynamics at all scales [3].

In this work, it is demonstrated by means of numerical simulations that OCM can be operated effectively in a heat-exchange integrated microchannel reactor. The modeling and simulation domain presented here involves groups of parallel reaction (OCM) and cooling channels, which are separated by thin solid walls. Since the flow in microchannels is described by laminar flow conditions, simultaneous modeling of reactive flow and heat exchange requires the composition and solution of a comprehensive mathematical model. For this purpose Computational Fluid Dynamics (CFD) technique is used to solve the model equations, i.e. mass, energy, momentum and continuity balances governing the phases involved such as fluid, solid and porous catalyst phases. The effect of operational and structural parameters of the reaction system on temperature distribution, methane conversion and ethylene selectivity are studied in the context of a parametric plan.

The literature survey about microchannel reactors and OCM reaction is given in Chapter 2. In Chapter 3 simulation studies about OCM are described in detail by giving a complete explanation of the mathematical model, reaction kinetics, and the parameters which will be investigated in the simulations. Results of computational simulations are given in Chapter 4

together with the discussions of the outcomes. In Appendix section, detailed numerical results of the simulations are given together with reaction rates of all steps in the OCM mechanism. Finally, major conclusions are explained and recommendations are given for the future studies.

2. LITERATURE SURVEY

2.1. Microchannel Reactors

Process intensification using microtechnology is a novel system for miniaturizing the macroscale chemical equipments in a process. Microtechnology provides significant size reduction while facilitating better control over the entire system. Microtechnologies such as micro-heat-exchangers and microreactors favor achieving higher heat and mass transfer rates in microfluidic conditions, resulting in enhanced product yields [4]. The advantages of microreaction technology, like increased efficiency and productivity makes it an attractive option for chemical processes involving highly exothermic/endothermic reactions [5].

Microreactors consist of structured channels with typical widths of 50 μm to 500 μm. The main advantage of microchannel reactors is improved flow patterns due to reduction of physical size. As a result of the decrease in the fluid layer thickness, surface-to-volume ratio of the fluid element also increases. Specific surfaces of microchannel reactors are in the range of 10,000 to 50,000 m^2/m^3, whereas conventional vessel type reactors usually do not exceed 100 m^2/m^3 [3]. Due to the presence of laminar flow conditions and constant (asymptotic) values of the Nusselt number, heat transfer coefficients become inversely proportional to the channel width. For a typical microchannel reactor, heat transfer coefficients for liquids are about 10 kW m^{-2} K^{-1}. Heat transfer coefficient around 25 kW m^{-2} K^{-1} with water as cooling medium is also reported which exceed those of conventional heat exchangers by at least one order of magnitude [3]. High heat transfer avoids hot-spot formation and allows to benefit the full potential of the catalysts during highly exothermic or endothermic reactions.

In microchannel reactors, higher reaction temperatures are achieved with lower reaction volumes and less amount of catalysts which not only improves the energy efficiency of the system, but also reduce the operational cost. Radial diffusion time in microchannel reactors is directly proportional to the channel sizes. Short radial diffusion time leads to a narrow residence time distribution which is favorable for consecutive reactions since the selectivity of desired intermediate product is increased [6].

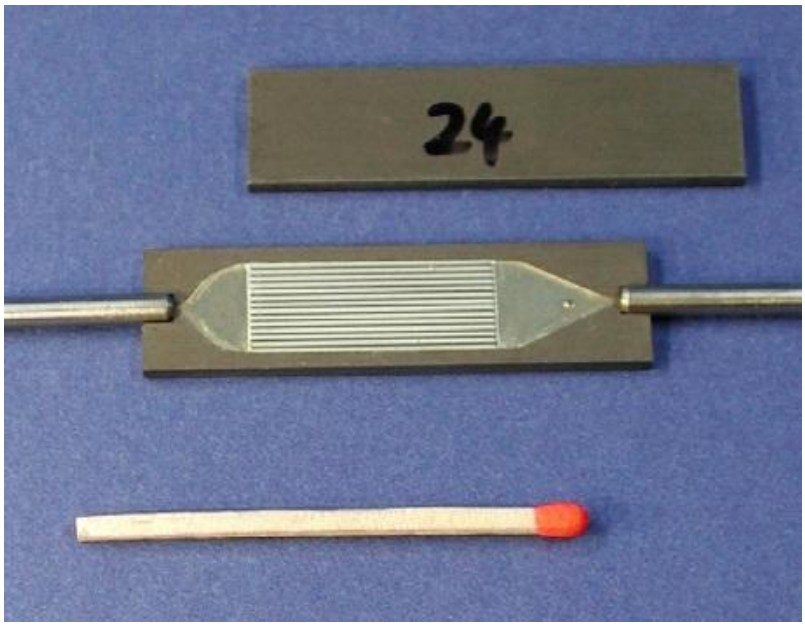

Figure 2.1. Multi-layer microreactor [7].

The ratio of heat transfer to pressure loss is an important factor while considering heat exchangers. In micro-heat-exchangers, pressure drop is minimum due to laminar flow regime while heat transfer is improved with high specific surface area. These advantages make the application of microtechnology on heat exchangers favorable. Heat exchange and reactor integration in the same volume has been applied to microchannel reactors in recent years. Microchannel reactors can be customized to handle multiple reactions in the same volume. By this way, two reactions with extreme conditions like high exothermicity and endothermicity can run together in the same unit. Good heat transfer capability of micro reactors helps such dual reaction system to converge in the desired manner.

The coupling of an exothermic combustion reaction with an endothermic synthesis reaction, both running in adjacent channels of the same micro reactor has received many researchers' attention. In that kind of reaction systems, heat is exchanged between two different reactions simultaneously [8-10]. Apart from coupling of endothermic and exothermic reactions, cooling systems can be implemented within the same reactor in order to obtain temperature control over the reaction. In the computer-based study of Gümüşlü and Avci [11], exothermic Fischer-Tropsch synthesis channels are coupled with cooling channels to improve temperature control. With the heat-exchange between the reaction and the cooling channels, it is aimed to achieve near-isothermal conditions.

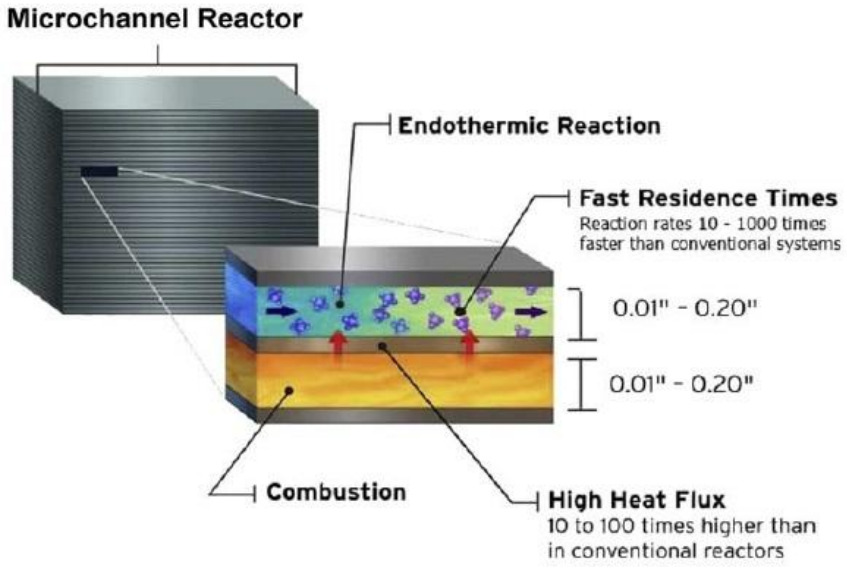

Figure 2.2. Coupling of endothermic/exothermic reactions in the same microreactor [12].

The main purpose of using microchannel technology is implementation to industrial production, which requires maintaining the efficiency found in pilot applications. Unlike the conventional type of reactors, scale-up of microchannel reactors can be done by numbering-up of microchannel units keeping the channel hydrodynamics identical at all scales without losing efficiency [3].

The properties of microchannel reactors discussed in this section make it a promising option for the application of OCM reaction. Heat transfer and residence time distribution have critical importance for OCM, since the exothermal heat is detrimental to the yield of ethylene, while narrow residence time distribution is crucial to take ethylene intermediate before it decomposes further in the reactor.

2.2. Oxidative Coupling of Methane

The pioneering study of Keller and Bhasin [13] initiated an intensive research on the topic of OCM. Neither OCM nor other natural gas conversion methods, which can be found in Gesser and Hunter [14], have found a commercial application yet. The studies on the subject of OCM are focused on two major paths, namely catalyst design and reaction engineering. Hundreds of different catalysts have been developed by scientists and companies to achieve high product selectivity and high ethylene yield. Also different reactor types have been

studied to find the most efficient reactor configuration suitable for OCM. Before reviewing the literature about different catalyst designs and reaction engineering studies, it is important to know the mechanism of OCM reaction for a better understanding of the following research studies.

2.2.1. Mechanistic Aspects

The OCM reaction occurs via a heterogeneous-homogeneous mechanism. Ethane is a primary product and ethylene is an intermediate product both of which are converted into undesired CO_x with further oxidation. Ethylene is formed via homogeneous and heterogeneous ethane dehydrogenation reactions. However, existence of methane in the reactive flow inhibits the homogeneous step due to its high binding energy. Undesired CO_x products are formed via consecutive transformations of ethane and ethylene. Since the reactivities of ethane and ethylene are high compared with methane, combustion of C_2 products into CO_x becomes the main route of CO_x formation when the degree of methane conversion increases [2].

The existence of oxygen species in the reacting fluid is required for methane activation. However, the nature of these oxygen species is found to be important for high C_2 selectivity. Oxygen adsorption over OCM catalysts decreases the reaction activity. On the other hand, the high temperature profile of OCM reaction is also detrimental for C_2 product yield, because the high temperature together with excess oxygen in the medium triggers the consecutive transformation of C_2 hydrocarbons into CO_x products.

2.2.2. Catalyst Design

The aim of all studies done for new catalyst designs are to achieve high selectivity towards C_2 products at methane conversions as high as possible. The OCM performance over different catalyst materials is summarized in Table 2.1 [2]. It can be seen from this summary that, the yield of C_2 hydrocarbons does not exceed 30%, with methane conversions between the ranges 20-45%. These yield amounts are insufficient for a commercial application of OCM, since in the industrial scale implementation limits of the OCM reaction involves 30%

or higher C_2 yields [15]. Therefore, the yield of C_2 hydrocarbons should be improved with different reactor configurations using reaction engineering concepts.

Table 2.1. OCM Performance over different catalytic materials [2].

Catalyst	**T / K**	**X(CH_4)[a] / %**	**S(C_2)[b] /%**	**Y(C_2)[c] /%**
Li/MgO	1013	37.8	50.3	19
30% BaO/Ga_2O_3	1023	32	54	17.3
95mol% BaF_2/Y_2O_3	1023	36.1	62.1	22.4
La/MgO	1073	29.3	58.8	17.2
Rb_2WO_4/SiO_2	1123	32	78	25
$Bi_{1.5}Y_{0.3}Sm_{0.2}O_{3-\delta}$	1223	43.5	62	27
La_2O_3-CeO_2	1048	22.3	66	14.7
Na_2WO_4/SiO_2	1123	44	52	22.9
Sm_2O_3	1053	20	65.4	13.1
[a] X(CH_4) = methane conversion, $x_{CH_4} = 100 \times \frac{F_{CH_4}^{in} - F_{CH_4}^{out}}{F_{CH_4}^{in}}$				
[b] S(C_2) = selectivity towards C_2H_6 and C_2H_4, $S_{C_2} = 100 \times \frac{2F_{C_2H_6} + 2F_{C_2H_4}}{F_{CH_4}^{in} - F_{CH_4}}$				
[c] Y(C_2) = yield of C_2H_6 and C_2H_4, $Y_{C_2} = 100 \times \frac{2F_{C_2H_6} + 2F_{C_2H_4}}{F_{CH_4}^{in}}$				

In a recent study by Schuurman and coworkers [16], a novel catalyst for microchannel reactors is developed specially for the OCM reaction. It is stated that lanthanum based catalysts, which have the good performance for OCM reaction compared to other catalysts, are likely to lose activity when applied in stainless steel microchannel reactors due to incorporation of chromium into the catalyst surface. In order to solve this problem, they coated enamel at the inner walls of the stainless steel microchannel and then applied the catalyst coating on top of enamel surface. They performed activity experiments shown in Figure 2.3. In the case of the unprotected catalyst sample (Figure 2.3b), a low C_2 selectivity is observed which is rapidly dropping to zero and the main product was carbon dioxide. The enamel protected sample (Figure 2.3a) shows higher C_2 selectivity up to 35% that only slightly declines with time on stream. In the final case where one of the walls is left unprotected and uncoated (Figure 2.3c), again very low C_2 selectivity is observed which proves the chromium contamination can occur through gaseous intermediates.

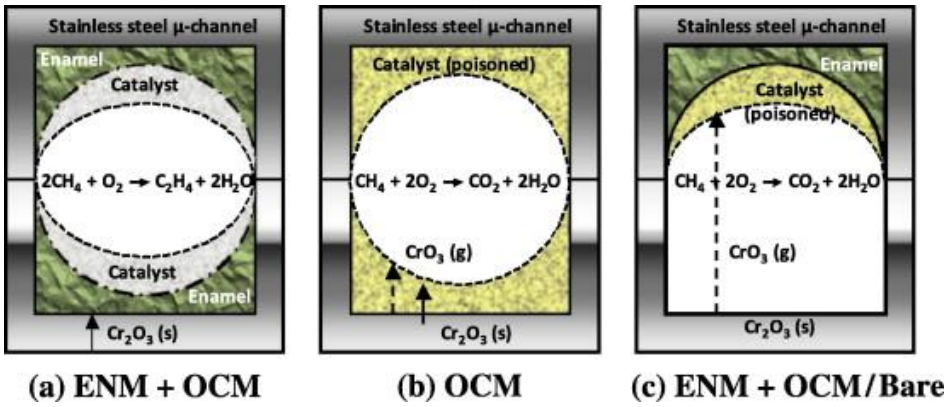

Figure 2.3. Scheme of catalyst poisoning in microchannel walls with different enamel/catalyst configurations (a) ENM+OCM, (b) OCM and (c) ENM+OCM/Bare.

2.2.3. Reaction and Process Engineering

The knowledge of the reaction kinetics describing the reaction mechanism within OCM network is essential for modeling and simulation of the system. The intrinsic kinetic data for OCM is difficult to obtain due to the high exothermicity and operating temperatures [2]. Early kinetic analysis of the OCM reaction was developed over sodium based catalysts [17, 18]. However, the most comprehensive intrinsic kinetics up to date, which consists of three primary and seven consecutive reactions was reported in 1997 by Stansch *et al.* [19]. The kinetics developed is based on a La_2O_3/CaO catalyst for the reaction network presented in Figure 2.4. This reaction mechanism considers the formation of ethane and ethylene and also of CO and CO_2 via different reaction pathways, including one gas-phase reaction step.

The reactor choice for OCM is crucial due to high exothermicity. The very first reactors used to test OCM were catalytic fixed-bed type. The studies showed that axial and radial temperature gradients existed in the reactor due to the high exothermicity and highest C_2 yields resulted to 15.5% with 31% of methane conversion and 51% of C_2 selectivity, which is too far from commercial application limits [20].

Comparable or even higher C_2 yields are achieved in the application of fluidized-bed reactor (Y_{C2} = 17%). Pannek and Mleczko [21, 22] have modeled a fluidized-bed reactor using the kinetics of Stansch *et al.* [19] for the La_2O_3/CaO catalyst. In their study they concluded that in an industrial fluidized-bed reactor C_{2+} yields will be lower when compared

to a lab-scale reactor, due to larger contact times. Their results also showed that the neglection of consecutive gas phase reactions proposed for lab-scale reactors is not justified when scaling up to an industrial reactor.

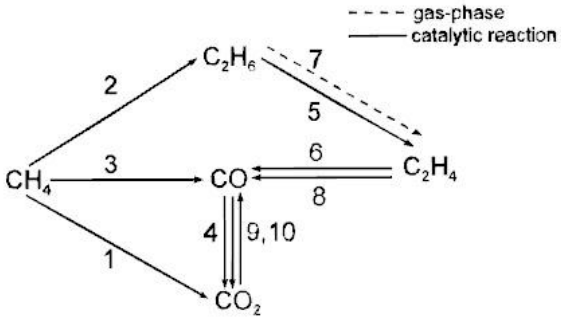

Figure 2.4. Reaction scheme and pathways [19].

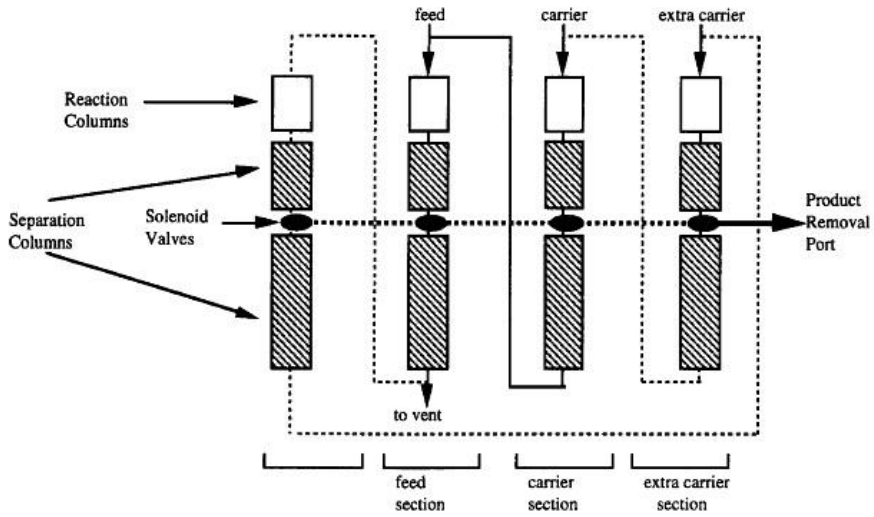

Figure 2.5. Schematic overview of the counter-current moving-bed chromatographic reactor [23].

A different approach to optimize the OCM reaction is to separate C_2 hydrocarbons simultaneously from the unreacted feed. This concept is studied in a counter-current moving bed chromatographic reactor by Kruglov and coworkers [23]. This reactor, shown in Figure 2.5, consists of four identical sections connected in series, each including a high temperature reaction column packed with catalyst, followed by two low temperature separation columns in

which intermediate C_2 hydrocarbon products are separated from the product flow. A C_2 yield of 55% at a methane conversion of 75% was achieved over $YBa_2Zr_3O_{9.5}$ catalyst under optimal operating conditions. This results exceeds the commercial feasibility limits. However, it is not possible for such a process can become economically viable due to the requirement for recycling huge amounts of unconverted methane.

Apart from residence time and temperature control, the inlet concentration of oxygen is also of great importance since high oxygen concentrations have negative impact on C_{2+} selectivity whereas low concentrations are unfavorable for high degrees of methane conversion and high C_{2+} yields. An alternative solution to oxygen feeding problem is to provide distributed oxygen delivery along the reactor. Kao and coworkers [24] have studied the comparison of OCM performances of a co-fed fixed-bed reactor (FBR) and a ceramic dense-membrane reactor (DMR). The concentration of the oxygen transported through the membrane was lower within the DMR than in the FBR and it is almost at a uniform level thought the reactor length in DMR. The results showed that the DMR is able to achieve better C_2-selectivity at the same yield with FBR (S_{C2} = 87%, Y_{C2} = 21% in DMR). In a following study of the same group [25], it was reported that bulk diffusion of the electron holes is the rate-limiting step for oxygen permeation. It was shown experimentally that membrane reactors are able to achieve higher selectivities than in the FBR, supporting the results of the simulation study. However, none of the studies reached commercial feasibility limits, i.e., single pass methane conversions of 35-37% and C_2 yields of 30%.

One of the most extensive comparative study of different kinds of reactor applications for the OCM reaction is done by Kiatkittipong and coworkers [26]. They concluded that FBR (Figure 2.6-a) is not recommendable for OCM in commercial applications, whereas porous membrane reactors (PMR) and mixed ionic and electronic conducting membrane reactors (MIEMR) are applicable at temperatures lower than 1150 K and higher than 1150 K, respectively (Figure 2.6-b-c). However, the use of PMR is not recommended in the case of air feed or oxygen feed contains impurities. High pressure operation was beneficial only to MIEMR and solid oxide fuel cell reactor (SOFCR). The drawback of PMR was the methane loss through the non-selective porous membrane and that of SOFCR (Figure 2.6-d) was the requirement for nearly 200 K higher operating temperatures compared with the others, but the electricity generated as by-product might make SOFCR still attractive.

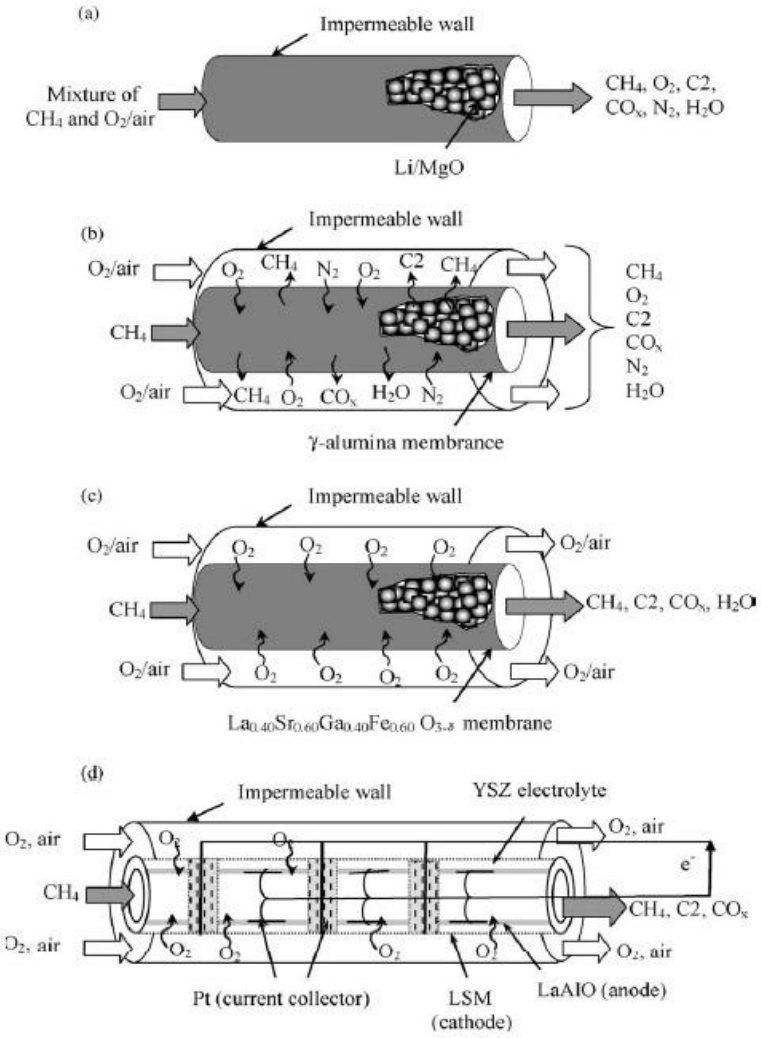

Figure 2.6. Schematic overview of (a) FBR, (b) PMR, (c) MIEMR and (d) SOFCR [26].

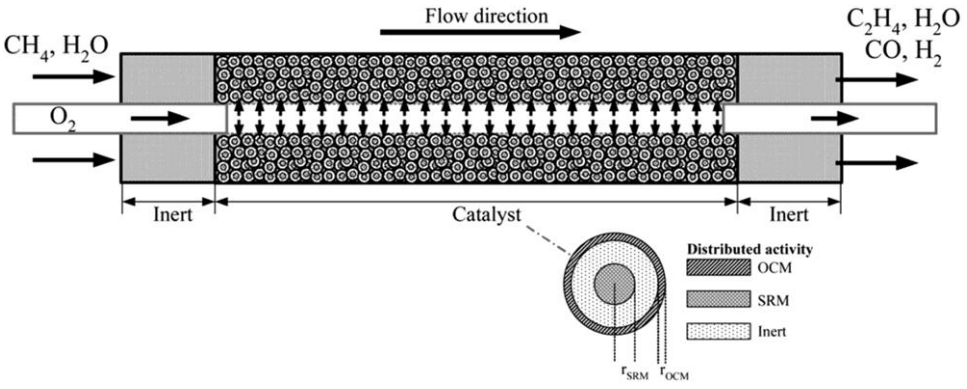

Figure 2.7. Schematic of the dual function catalyst particle implemented in a packed bed membrane reactor with distributed O_2 feeding [28]

In the subject of temperature control over the OCM reaction, coupling of endothermic and exothermic reactions is a new concept that attracted the interest of researchers. In the recent studies of van Sint Annaland and coworkers [27, 28], a packed bed membrane reactor was developed for exothermic oxidative coupling and endothermic steam reforming of methane with a dual function catalyst. In the first part of the study, the authors first designed a dual-function catalyst that works for both coupling and reforming reactions, and with numerical simulations they showed the improvement of ethylene synthesis. In the second part of the study, they run the reactions in a packed bed membrane reactor in different layers (Figure 2.7), catalyst being in the between, and again by numerical solutions, they showed that temperature profiles of the reactor is reduced by employing such autothermal operation and an enhanced methane conversion of 48% is obtained with a maximum C_2 yield of 39%.

The main challenge facing the commercialization of methane oxidative coupling is to avoid the complete oxidation of methane and increase the yield of desired products, C_2 hydrocarbons, which show progress with intensive research. However, almost all studies done in this field state that, lower C_2 hydrocarbon production yields will be achieved when the scale-up to the conventional reactor sizes are performed. Microchannel technology seems to be a promising solution to the problems in scaling-up of OCM reaction with numbering-up principle which keeps the characteristics of a single unit cell at all scales.

3. MODELING AND SIMULATION

In this chapter, the construction of the mathematical model of the heat exchange integrated microchannel reactor is explained in detail. Computational fluid dynamics (CFD) model is used to solve governing mass, energy and momentum equations, and the reactive flow is simulated inside the system. In this work, oxidative coupling reactions of methane inside the heat exchange integrated microchannel reactor with La_2O_3/CaO catalyst is examined. Microchannel geometry, reaction kinetics and physical properties of the materials are obtained from the literature.

3.1. OCM Reaction Mechanism

In this study, the OCM reaction mechanism, proposed by Stansch *et al.* [19], is considered to run over La_2O_3/CaO catalyst. In this mechanism, there are nine heterogeneous reactions (R1-R6, R8-R10) and one gas-phase reaction (R7). First three reactions are primary reactions where ethane, carbon monoxide, water and hydrogen are produced. Ethane is produced via reaction R2 as a primary product and ethylene is the product of dehydrogenation reactions of ethane (R5, R7). Since ethylene is formed in consecutive reactions it is an intermediate product. CO and CO_2 are also primary products, formed via reactions R1 and R3.

$$CH_4 + 2O_2 \rightarrow CO_2 + 2H_2O \qquad \Delta H^0_{298} = \text{-802.6 kJ mol}^{-1} \qquad \text{(R1)}$$

$$2CH_4 + 0.5O_2 \rightarrow C_2H_6 + H_2O \qquad \Delta H^0_{298} = \text{-176.6 kJ mol}^{-1} \qquad \text{(R2)}$$

$$CH_4 + O_2 \rightarrow CO + H_2O + H_2 \qquad \Delta H^0_{298} = \text{-277.8 kJ mol}^{-1} \qquad \text{(R3)}$$

$$CO + 0.5O_2 \rightarrow CO_2 \qquad \Delta H^0_{298} = \text{-283 kJ mol}^{-1} \qquad \text{(R4)}$$

$$C_2H_6 + 0.5O_2 \rightarrow C_2H_4 + H_2O \qquad \Delta H^0_{298} = \text{-105.5 kJ mol}^{-1} \qquad \text{(R5)}$$

$$C_2H_4 + 2O_2 \rightarrow 2CO + 2H_2O \qquad \Delta H^0_{298} = \text{-757.1 kJ mol}^{-1} \qquad \text{(R6)}$$

$$C_2H_6 \rightarrow C_2H_4 + H_2 \qquad \Delta H^0_{298} = 136.3 \text{ kJ mol}^{-1} \qquad \text{(R7)}$$

$$C_2H_4 + 2H_2O \rightarrow 2CO + 4H_2 \qquad \Delta H^0_{298} = 210.1 \text{ kJ mol}^{-1} \qquad \text{(R8)}$$

$$CO + H_2O \rightarrow CO_2 + H_2 \qquad \Delta H^0_{298} = \text{-41.2 kJ mol}^{-1} \qquad \text{(R9)}$$

$$CO_2 + H_2 \rightarrow CO + H_2O \qquad \Delta H^0_{298} = 41.2 \text{ kJ mol}^{-1} \qquad \text{(R10)}$$

The reaction mechanism is separated into heterogeneous and gas-phase mechanisms. It is assumed that heterogeneous reactions occur only in the catalyst washcoat domain, and the gas-phase reaction (R7) occurs in the fluid phase, i.e., reaction channel domain. The fluids are assumed to be ideal and incompressible Newtonian type fluid. The flows are in the laminar regime. The whole system is considered to be at steady-state.

The operational parameters of the reaction system are selected consistent with the experimental conditions proposed by Stansch *et al*. [19]. The inlet pressures of the reactor and cooling channels are taken as atmospheric pressure. Inlet temperatures of the reactor and cooling flows are taken as 1023 K and 823 K respectively. At the reaction inlet, methane and oxygen are fed to the system with a molar ratio of 2.5 (CH_4/O_2). Nitrogen is also fed as an inert gas with methane and oxygen to the reaction channel. The minimum reaction temperatures observed in all simulations are above 850 K. In these conditions liquid-phase formation does not occur in the reaction channel. Similarly, the steam in cooling channel is also in gas-phase at the inlet condition and will be heated further by exothermic OCM reactions. Based on these facts, the mathematical model is constructed for gas-solid type of operation with fluid (gas) and catalyst washcoat phases. Porosity of the catalytic washcoat is taken as 4 x 10^{-1}. The density of the La_2O_3/CaO catalyst layer is adopted from its particulate counterpart, and is taken as 3600 kg m^{-3} [19].

3.2. Heat Exchange Integrated Microchannel Reactor

3.2.1. Microchannel Reactor Model

The heat exchange integrated microreactor system proposed for OCM reaction is presented in Figure 3.1. The system is composed of parallel reactor and cooling channels with dimensions of height $H = 6 \times 10^{-4}$ m, width $W = 2 \times 10^{-2}$ m and length $L = 5 \times 10^{-2}$ m which are separated by a solid stainless steel wall.

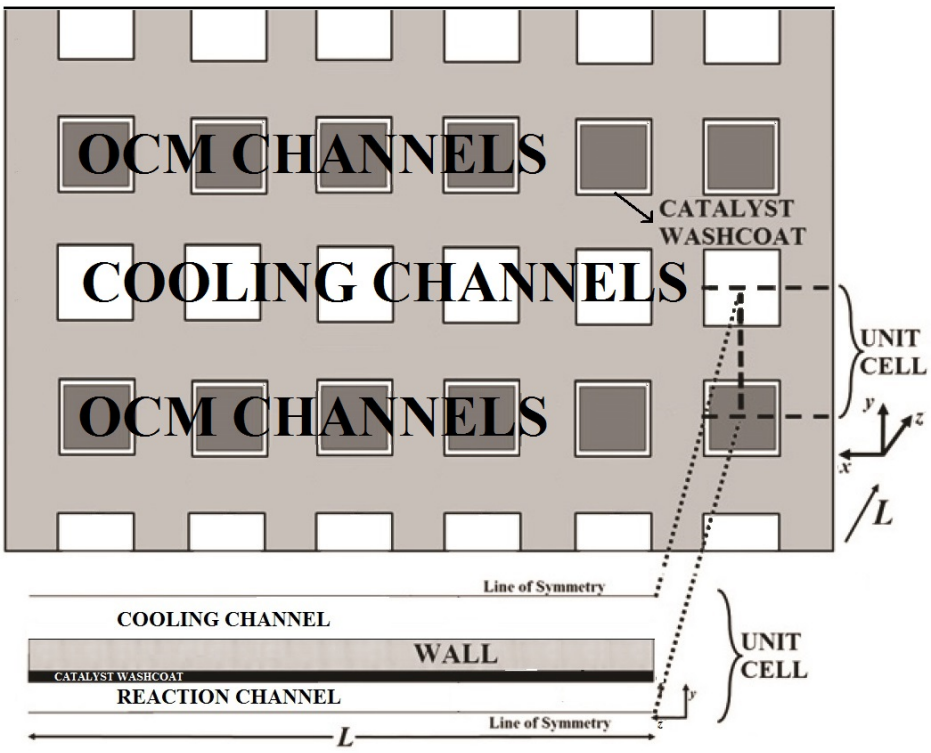

Figure 3.1. Schematic representation of the heat-exchange integrated microchannel reactor system (channel dimensions in the drawing are not to scale).

The cooling channel carries the cooling fluid steam, running in the counter current direction to that of the reaction channel which is shown in Figure 3.2. It is assumed that the heat transfer between the channels in the same horizontal line (in x-direction) is negligible when compared with the heat transfer between cooling and reaction channels. Since the gradients in x-direction are eliminated, the system can be simulated based on two dimensional unit cell. Unit cell is defined as the region between the centerlines of the cooling channel and the reaction channel along the channel length. Only the half channel regions are considered due to repeating pattern of the system in the y-direction.

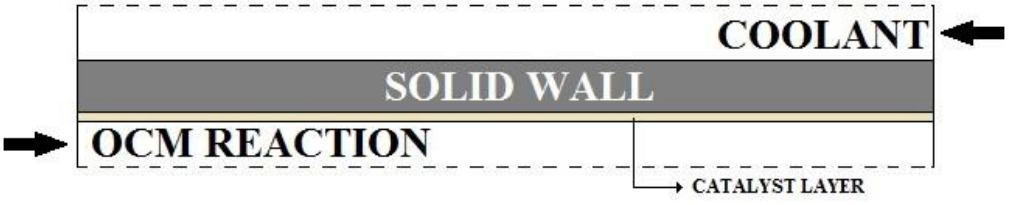

Figure 3.2. 2D representation of the unit cell.

3.2.2. Working Equations

2D Navier-Stokes partial differential equations describing mass, energy and momentum conservation within the reactor are used to simulate the OCM reaction in the microchannel reactor shown in Figure 3.1. Solution of these governing equations gives the temperature, velocity, species concentration and pressure regime in the channels. The physical properties like viscosity, diffusivity, and thermal conductivity are calculated using the correlations given in the literature [29]. Momentum equations are modified in order to simulate the reactive flow in porous layer. Reaction rates are introduced to the model as source terms in species mass and energy equations.

3.2.2.1. Continuity Equation. The continuity equation in 2D Cartesian coordinates is given in Equation 3.1.

$$\frac{\partial}{\partial x}\left(\rho_f v_x\right) + \frac{\partial}{\partial y}\left(\rho_f v_y\right) = 0 \tag{3.1}$$

3.2.2.2. Momentum Conservation Equation. The conservation of momentum is considered in cooling and reaction channels where fluid flows and also in catalyst washcoat phase. 2D Navier-Stokes equations for Newtonian fluids are solved in order to obtain momentum balance through the system. The general form of the Navier-Stokes equation for Newtonian fluids is:

$$\nabla \cdot \left(\rho_f \vec{\mathbf{v}}\vec{\mathbf{v}}\right) = \vec{\mathbf{F}} - \nabla \mathrm{p} + \nabla \cdot \bar{\bar{\tau}} + \rho_f \vec{g} \tag{3.2}$$

where the stress tensor $\bar{\bar{\tau}}$ is defined as:

$$\bar{\bar{\tau}} = \mu \left[\left(\nabla \vec{\mathbf{v}} + \nabla \vec{\mathbf{v}}^{\mathrm{T}}\right) - \frac{2}{3} \nabla \cdot \vec{\mathbf{v}}\mathbf{I}\right] \tag{3.3}$$

In Equation 3.3, μ is the molecular viscosity of the gas mixture inside the channel, **I** is the unit tensor. The second term on the right-hand side of the equation is the effect of volume dilation which contributes to dissipation of momentum due to viscous forces. This term can be

dropped out from the stress tensor, since its effect on the velocity field and viscous heating of the fluid is negligible. The simplified form of the momentum conservation equation together with stress tensor term for two dimensional Cartesian coordinates is given by Equations below;

$$v_x \frac{\partial}{\partial x}(\rho_f v_x) + v_y \frac{\partial}{\partial y}(\rho_f v_y) = -\frac{\partial p}{\partial x} + \frac{\partial}{\partial x}\left(\mu \frac{\partial v_x}{\partial x}\right) + \frac{\partial}{\partial y}\left(\mu \frac{\partial v_x}{\partial y}\right) \tag{3.4}$$

$$v_x \frac{\partial}{\partial x}(\rho_f v_y) + v_y \frac{\partial}{\partial y}(\rho_f v_y) = -\frac{\partial p}{\partial y} + \frac{\partial}{\partial x}\left(\mu \frac{\partial v_y}{\partial x}\right) + \frac{\partial}{\partial y}\left(\mu \frac{\partial v_y}{\partial y}\right) \tag{3.5}$$

In order to model the flow in porous region, standard fluid flow equations are replaced with Brinkman-extended Darcy equations. The coupling between Navier-Stokes equations in the gas phase and the Brinkman-extended Darcy equations in the catalyst layer is made possible by means of the conditions that the velocity and the normal component of the stress tensor are continuous through the gas-solid boundary. Modified momentum equations in order to simulate the flow in porous media are given by Equations below:

$$\left(\frac{\mu}{\alpha}\right) v_x = -\frac{\partial p}{\partial x} + \frac{\partial}{\partial x}\left[\left(\frac{\mu_{eff}}{\epsilon}\right)\frac{\partial v_x}{\partial x}\right] + \frac{\partial}{\partial y}\left[\left(\frac{\mu_{eff}}{\epsilon}\right)\frac{\partial v_x}{\partial y}\right] \tag{3.6}$$

$$\left(\frac{\mu}{\alpha}\right) v_y = -\frac{\partial p}{\partial y} + \frac{\partial}{\partial x}\left[\left(\frac{\mu_{eff}}{\epsilon}\right)\frac{\partial v_y}{\partial x}\right] + \frac{\partial}{\partial y}\left[\left(\frac{\mu_{eff}}{\epsilon}\right)\frac{\partial v_y}{\partial y}\right] \tag{3.7}$$

In the Darcy model, the second term on the left hand side of each equation corresponds to viscous fluid motion due to pressure gradient. The flow in porous region is not due to inertial effects but due to the combination of viscous and pressure effects. The viscous Brinkman terms appear on the right-hand sides of Equations 3.6 and 3.7. These equations include terms accounting for the boundary frictional drag on the impermeable walls of the channels. The Brinkman-extended Darcy equations make use of an effective viscosity μ_{eff} which depends on the geometry of the medium [30]. This value is taken to be equal to the fluid viscosity in the gas phase.

3.2.2.3. Species Mass Conservation Equations. The general form of species mass conservation equation in 2D Cartesian coordinates is given as

$$\nabla \cdot \left(\rho_f \vec{\mathbf{v}} Y_i\right) = -\nabla \cdot \overrightarrow{\boldsymbol{J_\iota}} + M_i R_{k_v}^v + M_i R_{k_s}^s A_s \tag{3.8}$$

In the above equation i is used to identify the species. $\overrightarrow{\boldsymbol{J_\iota}}$ is the Fickian diffusive mass flux given by:

$$\overrightarrow{\boldsymbol{J_\iota}} = -\rho_f \, D_{eff,i,m} \, \nabla Y_i \tag{3.9}$$

where $D_{eff,i,m}$ is the effective diffusivity of species i in the mixture. By inserting the Fickian diffusive mass flux equation into Equation 3.8 the species mass conservation equation in 2D Cartesian coordinates is found as follows:

$$\begin{aligned} v_x \frac{\partial}{\partial x}\left(\rho_f Y_i\right) + v_y \frac{\partial}{\partial y}\left(\rho_f Y_i\right) \\ = \frac{\partial}{\partial x}\left[D_{eff,i,m} \frac{\partial}{\partial x}\left(\rho_f Y_i\right)\right] + \frac{\partial}{\partial y}\left[D_{eff,i,m} \frac{\partial}{\partial y}\left(\rho_f Y_i\right)\right] + M_i R_{k_v}^v \\ + M_i R_{k_s}^s A_s \end{aligned} \tag{3.10}$$

In Equation 3.10, $R_{k_v}^v$ and $R_{k_s}^s$ demonstrades the consumption or production rate of the species i during volumetric and wall-surface reactions, respectively. Rate of heterogeneous reactions are calculated within the catalytic washcoat, and the homogeneous reaction R7 is considered to occur only in the reaction channel area. M_i is the molecular weight of species i, and A_s is the active surface area-to-volume ratio of the catalyst. When the flow of gas phase is under consideration, $D_{eff,i,m}$ simply equals $D_{i,m}$. For the flow in porous region, this simplification cannot be done so that $D_{eff,i,m}$ is calculated by using $D_{i,m}$ and the Knudsen diffusion in the pores of the region.

3.2.2.4. Energy Equation. The general form of energy equation in 2D Cartesian coordinates is given as;

$$\nabla . \left(\rho_f c_{p_f} \vec{\mathbf{v}} T\right) = \nabla . \left(k_{eff} \nabla T - \sum_i h_i \overrightarrow{\boldsymbol{J}_\iota} + (\bar{\bar{\tau}} \vec{\mathbf{v}})\right) + S \tag{3.11}$$

The generalized form of the energy conservation can be simplified by dropping out some terms due to their negligible effects on the temperature profile in the system. The term $\sum_i h_i \overrightarrow{\boldsymbol{J}_\iota}$ which indicates the heat transfer by the diffusive flux of all the species and the term $\bar{\bar{\tau}} \vec{\mathbf{v}}$ which shows the heat exchange due to viscous dissipation have much less effect on the temperature profile of the system when compared to the term $\epsilon \frac{\partial}{\partial t}\left(\rho_f c_{p_f} T\right)$ which represents the conduction heat transfer, so they are dropped out. After these assumptions, the energy equation in 2D Cartesian coordinates simplifies to,

$$\begin{aligned} v_x \frac{\partial}{\partial x}\left(\rho_f c_{p_f} T\right) + v_y \frac{\partial}{\partial y}\left(\rho_f c_{p_f} T\right) \\ = \frac{\partial}{\partial x}\left[k_{eff} \frac{\partial}{\partial x}\left(\rho_f T\right)\right] + \frac{\partial}{\partial y}\left[k_{eff} \frac{\partial}{\partial y}\left(\rho_f T\right)\right] + S \end{aligned} \tag{3.12}$$

The effective thermal conductivity k_{eff} is calculated by taking the volume average of fluid (k_f) and solid (k_s) conductivities:

$$k_{eff} = \epsilon k_f + (1 - \epsilon) k_s \tag{3.13}$$

When the flow of gas phase, outside of the porous layer is under consideration, the porosity ϵ is taken as 1 and Equation 3.12 becomes,

$$v_x \frac{\partial}{\partial x}\left(\rho_f c_{p_f} T\right) + v_y \frac{\partial}{\partial y}\left(\rho_f c_{p_f} T\right) = \frac{\partial}{\partial x}\left[k_f \frac{\partial}{\partial x}\left(\rho_f T\right)\right] + \frac{\partial}{\partial y}\left[k_f \frac{\partial}{\partial y}\left(\rho_f T\right)\right] + S \tag{3.14}$$

The term S represents the source of energy (heat generation or consumption) and it is calculated as;

$$S = \sum_{k_v=1}^{N_{v\,rxn}} \left(-\Delta H_{k_v} R_{k_v}^v\right) + \sum_{k_s=1}^{N_{s\,rxn}} \left(-\Delta H_{k_s} A_s R_{k_s}^s\right) \tag{3.15}$$

3.2.3. Boundary Conditions

The mass, momentum and energy conservation equations given in Section 3.2.2 is solved subject to the boundary conditions explained in this section.

3.2.3.1. Channel Entrance. The velocity of flow at the channel inlets is assumed to be unidirectional; therefore, a normal inflow velocity is specified. Mass fraction of each species *i* fed to the channel *j* is also prescribed and a constant, time-independent temperature inlet condition in each channel inlet is also specified.

Table 3.1. Boundary conditions used for channel entrance regions.

Channel entrance: $x_{rxn} = 0$; $x_{cooling} = L$
$u_j = u_j^{in}$
$Y_{ij} = Y_{ij}^{in}$
$T_j = T_j^{in}$

3.2.3.2. Symmetry Lines. There is no convective flux across a symmetry boundary, thus the normal component of velocity is zero. There is no diffusion flux across a symmetry plane either, so the gradients of all flow variables are also zero. Since the shear stress is zero at a symmetry boundary, the wall can assumed to be "slip" wall when used in viscous flow calculations.

Table 3.2. Boundary conditions used for symmetry lines.

Symmetry at the channel centerline
$\vec{\boldsymbol{n}} \cdot \vec{v}_j = 0$
$\vec{\boldsymbol{n}} \cdot \left(\overrightarrow{J_{ij}} + \rho_{fj} \vec{v}_j Y_{ij}\right) = 0$
$\vec{\boldsymbol{n}} \cdot \left(-k_{eff,j} \nabla T_j + \rho_{fj} c_{p_{fj}} \vec{v}_j T_j\right) = 0$

3.2.3.3. Gas-Solid Interface. The general approach associated with gas-solid boundary is the continuity of the vector quantity (i.e. velocity, mass fraction, temperature), and the continuity of the normal component of the diffusion tensor (i.e. momentum, mass, heat).

Table 3.3. Boundary conditions used for gas-solid interface.

Gas-Solid interface
$\vec{v}_j\big\vert_{gas} = \vec{v}_j\big\vert_{solid}$
$\vec{\boldsymbol{n}} \cdot \left(\overrightarrow{J_{\imath J}} + \rho_{fj}\vec{v}_j Y_{ij}\right)\big\vert_{gas} = \vec{\boldsymbol{n}} \cdot \left(\overrightarrow{J_{\imath J}} + \rho_{fj}\vec{v}_j Y_{ij}\right)\big\vert_{solid}$
$\vec{\boldsymbol{n}} \cdot \left(-k_{eff,j}\nabla T_{\mathrm{j}} + \rho_{fj} c_{p_{fj}} \vec{v}_j T_j\right)\Big\vert_{gas} = \vec{\boldsymbol{n}} \cdot \left(-k_{eff,j}\nabla T_{\mathrm{j}} + \rho_{fj} c_{p_{fj}} \vec{v}_j T_j\right)\Big\vert_{solid}$

3.2.3.4. Channel Exit. At the exit regions of the channels, the pressure is set to a value. Reversed flow occurs at the exit while using finite volume method; therefore, backflow conditions consistent with the inlet values support the solution in minimizing convergence difficulties.

Table 3.4. Boundary conditions used for channel exits.

Channel exit: $x_{rxn} = L$; $x_{cooling} = 0$
$p_j = p_j^{out}$
$\vec{\boldsymbol{n}} \cdot \overrightarrow{J_{\imath J}} = 0$
$\vec{\boldsymbol{n}} \cdot \left(-k_{eff,j}\nabla T_{\mathrm{j}}\right) = 0$

3.2.3.5. Other Boundaries. The system or unit cell boundaries other than the ones explained in this section are treated as insulated walls or symmetry boundaries where the velocity is zero and there are no mass or heat fluxes.

Table 3.5. Boundary conditions used for all other boundaries.

Other boundaries
$\vec{\boldsymbol{n}} \cdot \vec{v}_j = 0$
$\vec{\boldsymbol{n}} \cdot \left(\overrightarrow{J_{\imath J}} + \rho_{fj}\vec{v}_j Y_{ij}\right) = 0$
$\vec{\boldsymbol{n}} \cdot \left(-k_{eff,j}\nabla T_{\mathrm{j}} + \rho_{fj} c_{p_{fj}} \vec{v}_j T_j\right) = 0$

3.2.4. Reaction Kinetics

The kinetic expressions of Hougen-Watson and power-law type are used for describing the OCM reaction over La_2O_3/CaO catalyst which is adapted from Stansch *et al.* [19]. The Hougen-Watson type of equations are used in order to consider the inhibiting effect of carbon dioxide on the formation of ethane while power-law rate equations are applied to the reactions R7 to R10. The rate expressions associated with the reactions listed in Section 3.1 are presented in Equations 3.16-3.21. The kinetic parameters used in the governing rate equations are also given in Table 3.6.

$$r_2 = \frac{k_{0,2} e^{-E_{a,2}/RT} (K_{0,O_2} e^{-\Delta H_{ad,O_2}/RT} p_{O_2})^{n_2} p_{CH_4}}{[1 + (K_{0,O_2} e^{-\Delta H_{ad,O_2}/RT} p_{O_2})^{n} + K_{j,CO_2} e^{-\Delta H_{ad,O_{2j}}/RT} p_{O_2}]^2} \tag{3.16}$$

$$r_j = \frac{k_{0,j} e^{-E_a/RT} P_C^{m_j} P_{O_2}^{n_j}}{\left(1 + K_{j,CO_2} e^{-\Delta H_{ad,CO_{2,j}}/RT} p_{CO_2}\right)^2} \qquad j = 1, 3-6 \tag{3.17}$$

$$r_7 = k_{0,7} e^{-E_{a,7}/RT} p_{C_2H_6} \tag{3.18}$$

$$r_8 = k_{0,8} e^{-E_{a,8}/RT} {p_{C_2H_4}}^{m_8} {p_{H_2O}}^{n_8} \tag{3.19}$$

$$r_9 = k_{0,9} e^{-E_{a,9}/RT} {p_{CO}}^{m_9} {p_{H_2O}}^{n_9} \tag{3.20}$$

$$r_{10} = k_{0,10} e^{-E_{a,10}/RT} {p_{CO_2}}^{m_{10}} {p_{H_2}}^{n_{10}} \tag{3.21}$$

Table 3.6. Kinetic parameters used in reaction rates.

Step	$k_{0,j}$	$E_{a,j}$	$K_{j,CO2}$	$K_{j,O2}$	$\Delta H_{ad,CO2,j}$	$\Delta H_{ad,O2,j}$	m_j	n_j
1	0.20×10^{-5}	48	0.25×10^{-12}		-175		0.24	0.76
2	23.2	182	0.83×10^{-13}	0.23×10^{-11}	-186	-124	1	0.40
3	0.52×10^{-6}	68	0.36×10^{-13}		-187		0.57	0.85
4	0.11×10^{-3}	104	0.40×10^{-12}		-168		1	0.55
5	0.17	157	0.45×10^{-12}		-166		0.95	0.37
6	0.06	166	0.16×10^{-12}		-211		1	0.96
7	1.2×10^{7}	226						
8	9.3×10^{3}	300					0.97	0
9	0.19×10^{-3}	173					1	1
10	0.26×10^{-1}	220					1	1
$k_{0,j}$ (mol g^{-1} s^{-1} $Pa^{-(m+n)}$), $E_{a,j}$ (kJ mol^{-1}), $K_{j,CO2}$ (Pa^{-1}), $\Delta H_{ad,CO2,j}$ (kJ mol^{-1})								

The rate equations are introduced to the simulation software with a user defined function, as source terms for the mass and energy equations. The model equations explained in Section 3.2.2 are solved together with the boundary conditions given in Section 3.2.3 using the finite volume method on ANSYS Fluent™ 14.5 platform running on a HP z800 workstation equipped with 12 × 2.67GHz Intel Xeon™ processors and 47 GiB memory. The 2D Cartesian mesh consisting of ~5×10^5 unstructured triangular cell elements is constructed using the software GAMBIT 2.4.6. Higher number of meshing is tested to check the simulation results. The solution of the model is independent from the number of mesh elements. The mesh is refined in the catalytic washcoat domain since steep temperature and concentration gradients are expected to occur due to reaction kinetics.

3.3. Parameters Analyzed During Simulations

At the beginning of the simulations, some test calculations are done in order to obtain default case values for the reactor system. The values are kept in the limits of previously studied parameters found in literature. The default values of the structural parameters which are the dimensions of the microreactor, material of construction and coolant fluid type, are

given in Table 3.7. The changes made in these parameters in the context of parametric analyses are described in the corresponding subsections.

The reaction mixture and coolant gases carry the properties given in the Table 3.8 at the inlet of the channels for all simulations. Any change in these properties is discussed in the corresponding subsection in detail.

Inlet temperature of the reactant flow is chosen as 750°C (1023 K) which is between the reaction temperature ranges of OCM (700°C - 955°C). The volumetric flow rate is varied around the value of $4x10^{-6}$ m^3/s STP in the microchannel which is proposed by Stansch *et al.* [19]. The volumetric flow rate values correspond to actual volumetric flow rate values in experimental studies for microchannel reactor applications [9]. Steam is selected as coolant fluid, and its inlet temperature is taken as 823 K at 100 kPa. Since the steam will be heated further by exothermal heat of OCM reaction, no condensation will occur in the coolant side of the unit cell.

Table 3.7. Default structural properties of the unit cell.

Microreactor Configuration	
Side length of the reaction channel (separate from catalyst layer)	5×10^{-4} m
Thickness of the catalytic washcoat	5×10^{-5} m
Thickness of the separating wall	3×10^{-4} m
Side length of the coolant channel	6×10^{-4} m
Channel length	5×10^{-2} m
Wall material	AISI Steel
Cooling fluid	Steam

For seven different parametric analysis a total of 27 cases is simulated, one being the default case included in each parametric analysis for comparison.

Table 3.8. Default operational properties of the unit cell.

Feed Conditions	
Molar CH_4/O_2 ratio	2.5
OCM mass flow rate	3.5×10^{-6} kg s^{-1}
Coolant mass flow rate	1×10^{-6} kg s^{-1}
Temperature/reaction channel	1023 K
Temperature/cooling channel	823 K
Pressure/reaction channel	1×10^{-5} Pa
Pressure/cooling channel	1×10^{-5} Pa

3.3.1. Methane-to-Oxygen Feed Ratio (CH_4/O_2) in Reaction Channel

Methane-to-oxygen feed ratio is one of the important parameters studied for OCM, since the oxygen content of the feed affects the rates of oxidation reactions inside the mechanism. Feed ratio is varied between the values 2 and 10, while molar fraction of methane is kept constant at 0.65 and the oxygen and inert nitrogen fractions are calculated for each corresponding ratio. Reactant mass flow rate is kept constant at 3.5×10^{-6} kg s^{-1} in order to keep the residence time in reaction channel constant. The feed ratio values studied are selected as 2, 2.5, 4, 6, 8 and 10. Other inlet conditions of the flows, wall thickness and wall material properties are kept constant at their default values. In Table 3.9, the mass flow rate values of methane, oxygen and nitrogen in the feed is given for each different feed ratio case.

Table 3.9. Mass flow rates of reactants for each feed ratio case.

Molar Feed Ratio (CH_4/O_2)	Total mass flow (kg s^{-1}) x 10^6	CH_4 mass flow (kg s^{-1}) x 10^6	O_2 mass flow (kg s^{-1}) x 10^6	N_2 mass flow (kg s^{-1}) x 10^6
2	3.5	1.69	1.69	0.114
2.5	3.5	1.71	1.37	0.415
4	3.5	1.75	0.877	0.881
6	3.5	1.76	0.588	1.15
8	3.5	1.77	0.443	1.28
10	3.5	1.78	0.356	1.37

3.3.2. Reaction Channel Inlet Temperature

Reaction inlet temperature is included in the parametric analysis in order to investigate its effect on the temperature profile of the reaction channel and on the product distribution. The experimental reaction temperature range for OCM is proposed by Stansch *et al.* as 973 K – 1228 K [19]. The inlet temperature values are selected consistent with the proposed temperature ranges. The reaction inlet temperature values studied are selected as 973, 1023, 1073, 1123, 1173 and 1223 K.

3.3.3. Cooling Channel Inlet Temperature

Cooling channel inlet temperature is studied as another parameter in the simulations. Inlet properties of the cooling fluid steam are important for determining the heat transfer between reaction and cooling channels. A temperature range of 773 K to 873 K is applied to steam while keeping the other properties constant. The steam inlet temperature values studied are assigned as 773, 798, 823, 848 and 873 K.

3.3.4. Reaction Channel Mass Flow Rate

The mass flow rate of the reaction channel is an important parameter to be studied because it determines the residence time of the reactants and intermediate products inside the channel, which directly affects the product selectivity and yield values.

Table 3.10. Linear velocity values introduced to the system for reaction channel.

Mass flow rate ($kg\ s^{-1}$) x 10^6	Linear velocity ($m\ s^{-1}$)
3	1.98
3.5	2.31
5	3.29
6	3.95

Mass flow rate of the reaction channel is increased gradually from $3x10^{-6}$ to $6x10^{-6}$ $kg\ s^{-1}$ while all other parameters are kept constant at their default values. Since the reaction

channel thickness is kept constant at $6x10^{-4}$ m, linear velocity values that are introduced to the simulations for reaction channel varied for changing the mass flow rate. The mass flow rate values considered in this study are given in Table 3.10 with the corresponding linear velocity values.

3.3.5. Cooling Channel Mass Flow Rate

Coolant mass flow rate is studied as a parameter in order to investigate the effects of coolant material amount on the system and to see the importance of residence time of steam in the reactor. Mass flow rate of cooling channel is increased gradually from 0.5×10^{-6} to 1.5×10^{-6} kg s^{-1} while all other parameters are kept constant at their default values. Since the cooling channel thickness is kept constant at 6×10^{-4} m, linear velocity of cooling channel is varied and introduced to the simulations in order to change the mass flow rate. The coolant mass flow rate values studied are assigned as 0.5×10^{-6}, 0.7×10^{-6}, 1×10^{-6} and 1.5×10^{-6} kg s^{-1}. The corresponding linear velocities introduced to the system are given in Table 3.11.

Table 3.11. Linear velocity values introduced to the system for cooling channel.

Mass flow rate (kg s^{-1}) x 10^6	Linear velocity (m s^{-1})
0.5	0.313
0.7	0.438
1.0	0.625
1.5	0.938

3.3.6. Reactor Wall Material

Material of construction in microchannels is an important parameter since it affects wall conduction and heat transfer between the channels. It is studied as a parameter while other variables (wall thickness and inlet flow conditions) are kept constant. The change in the material is introduced to the system as the change in wall thermal conductivity.

Table 3.12. Thermal conductivity of the materials of construction of the microchannel reactor.

Material	Thermal conductivity k, W m^{-1} K^{-1}
Alumina (Al_2O_3)	27
AISI Steel	44.5
Silicon Carbide	87

Suitable materials of construction for OCM application and their thermal conductivities are given in Table 3.12. Common wall materials like aluminum and copper are not considered as options in parametric analyses since the temperature range of OCM reaction system is not suitable for their application.

3.3.7. Reactor Wall Thickness

Thickness of the wall separating the channels is studied as a parameter to study its effect on heat transfer between channels and on improvement of OCM product selectivity and yield. Wall thickness is varied between 200 μm and 600 μm with 100 μm increments, while other parameters (wall material and inlet flow conditions) are kept constant. The thickness values studied are assigned as 200, 300, 400, 500 and 600 μm.

3.4. Mathematical Formulations Used in Results

The performance of the reactor is measured by the conversions of the reactants and the selectivity and yields of the products. The conversion is defined as the percent difference between inlet and outlet. For example the conversion of methane is

$$x_{CH_4} = 100 \times \frac{F_{CH_4}^{in} - F_{CH_4}^{out}}{F_{CH_4}^{in}} \tag{3.22}$$

and the selectivity is defined as the product formed per reactant consumed:

$$S_{C_2} = 100 \times \frac{2F_{C_2H_6} + 2F_{C_2H_4}}{F_{CH_4}^{in} - F_{CH_4}} \tag{3.23}$$

while the yield is calculated by the product per reactant fed:

$$Y_{C_2H_4} = 100 \times \frac{2F_{C_2H_4}}{F_{CH_4}^{in}} \tag{3.24}$$

4. RESULTS AND DISCUSSION

Oxidative coupling of methane is simulated in a heat-exchange integrated microchannel reactor. The effects of various operational and structural parameters (Section 3.3) on the reaction temperature and on the CH_4 conversion, C_2 yield and selectivity are investigated. Results of the parametric analyses are given in this section in terms of temperature profiles, reactant conversions, product selectivities and yields. For seven different parameters, a total of 27 cases are simulated, one being the default case which is kept same in each parametric analysis for comparison. The temperature profiles given in the figures are recorded from the centerline of the microchannel. The parameters studied in this work are explained in Section 3.3 and summarized in Table 4.1.

Table 4.1. Summary of the parameters studied in computational analysis.

Molar feed ratio (CH_4/O_2)	2, **2.5**, 4, 6, 8, 10
Reaction channel inlet temperature (K)	973, **1023**, 1073, 1123, 1173, 1223
Cooling channel inlet temperature (K)	773, 798, **823**, 848, 873
Reaction channel mass flow ($x10^6$ kg s^{-1})	3, **3.5**, 5, 6
Cooling channel mass flow ($x10^6$ kg s^{-1})	0.5, 0.7, **1**, 1.5
Wall material[1]	Alumina (27), **AISI Steel (44.5)**, Silicon Carbide (87)
Wall thickness (μm)	200, **300**, 400, 500, 600

[1] Thermal conductivities of each material is given in parenthesis (W/m.K).

4.1. Effect of Molar Feed Ratio of CH_4/O_2

A series of simulations are carried out with varying methane to oxygen ratio between 2 and 10. While varying the feed ratio, molar fraction of methane is kept constant at 0.65 and the oxygen and inert nitrogen fractions are calculated for each corresponding ratio. Reactant mass flow rate is kept constant at 3.5 x 10^{-6} kg s^{-1} in order to keep residence time constant. The highest methane conversion observed is 43% for the feed ratio of 2. The highest

selectivity of C_2 products is calculated as 57.1% for the feed ratio of 4, while highest yield values for ethylene and all C_2 products are found as 9.9% and 21.6% respectively for feed ratio of 2.5.

The effect of feed ratio on the reaction and coolant temperature profiles is given in Figure 4.1 and Figure 4.2, respectively. Below the feed ratio of 2, all hydrocarbons are oxidized to the carbon oxides immediately due to high oxygen amount. Therefore, ratios under 2 are not included in the simulations. The detailed numerical results of all simulations and the reaction rate results are given in Appendix A.

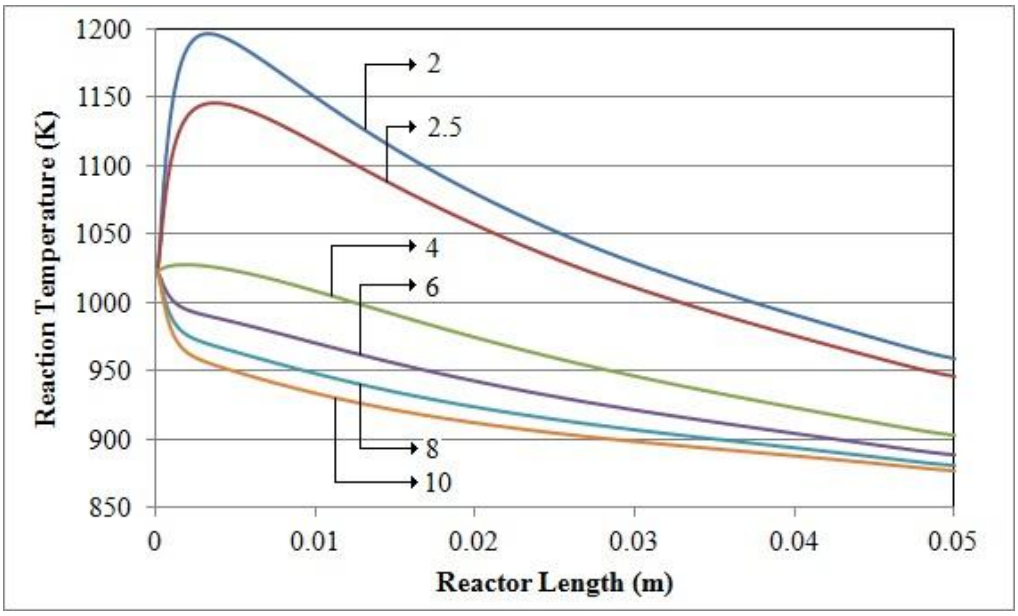

Figure 4.1. Effect of feed ratio on reaction temperature along the reactor.

As the feed ratio is increased, the maximum and outlet temperatures of the reaction channel are decreased as shown in Figure 4.1. The maximum temperature for feed ratio of 2 is found to be 1196 K while for feed ratio of 2.5 the maximum temperature is 1146 K in the reaction channel. The results for reaction temperatures are observed between the limits of experimental reaction conditions [19]. Further increase in feed ratio dampens the reaction temperature profiles. Above feed ratio of 4, maximum reaction temperatures cannot exceed the inlet temperature of 1023 K. The mass flow rate of oxygen in different feed ratio values is given in Table 3.9. When feed ratio is above 2.5, oxygen amount becomes insufficient to proceed the reaction mechanism forward and the rates of all the reactions in the mechanism slow down as shown in Figures A.1-10.

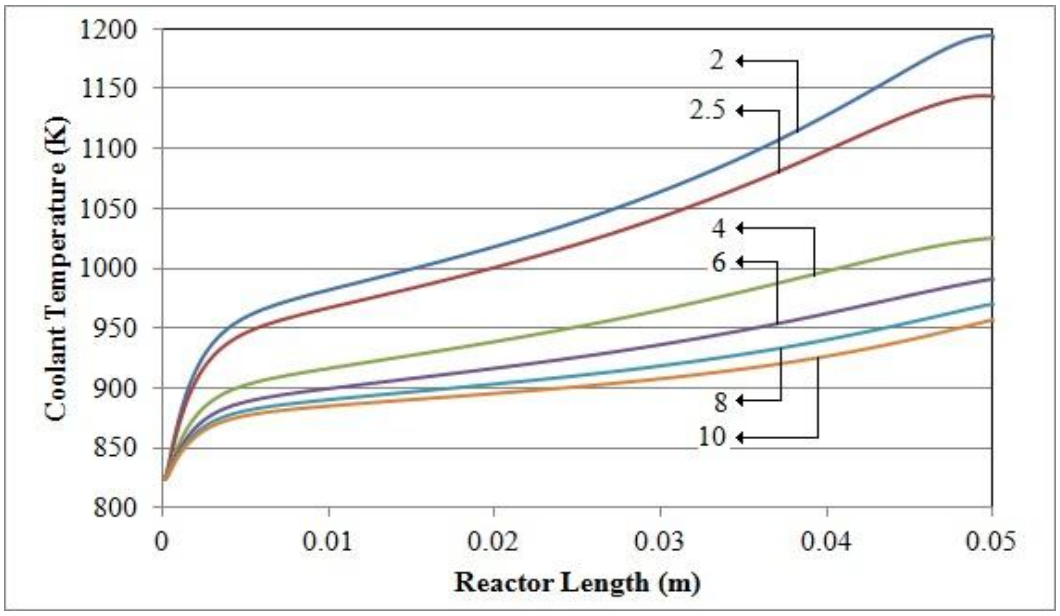

Figure 4.2. Effect of feed ratio on coolant temperature along the reactor.

The temperature profiles obtained in the centerline of the cooling channel at different feed ratios are shown in Figure 4.2. Since the flow direction in the channels is counter-current to each other, the cooling channel temperature profile is switched, i.e. coolant entrance point is taken as 0. At feed ratio of 2 and 2.5, steam temperature increases up to 1192 K and 1142 K respectively. The exothermal heat of OCM reaction increases steam temperature for about 350 K, which is an energy efficient side outcome of the microreactor application.

The methane and oxygen conversion profiles along the reactors which are given in Figure 4.3 and Figure 4.4 show that, when the feed ratio is low, i.e. the oxygen amount in the feed is high, methane and oxygen conversions reaches their maximum values at the very beginning of the reactor. This is due to the fact that, the primary reaction rates (R1, R2 and R3) are higher compared to the rest of the mechanism at low feed ratio values. The trends of conversions in the reactor for different feed ratio values come out as expected. Since the maximum temperature values do not exceed inlet temperatures, conversions of reactants decrease sharply at feed ratio values higher that 2.5 as shown in Figure 4.5. The highest methane conversion observed is 43% for the feed ratio of 2 and 42% for the feed ratio of 2.5.

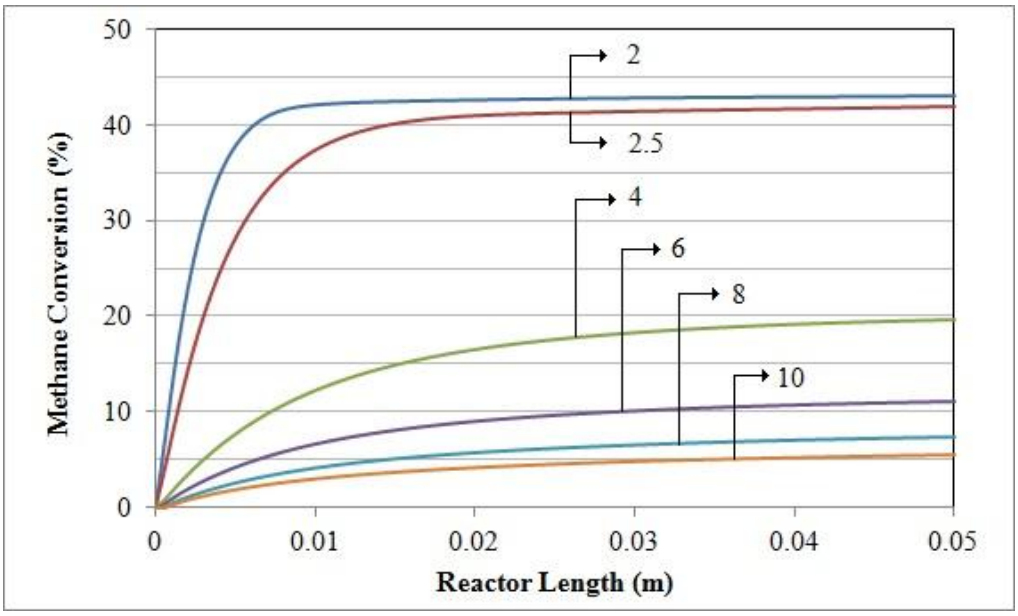

Figure 4.3. Effect of feed ratio on CH_4 conversion along the reactor.

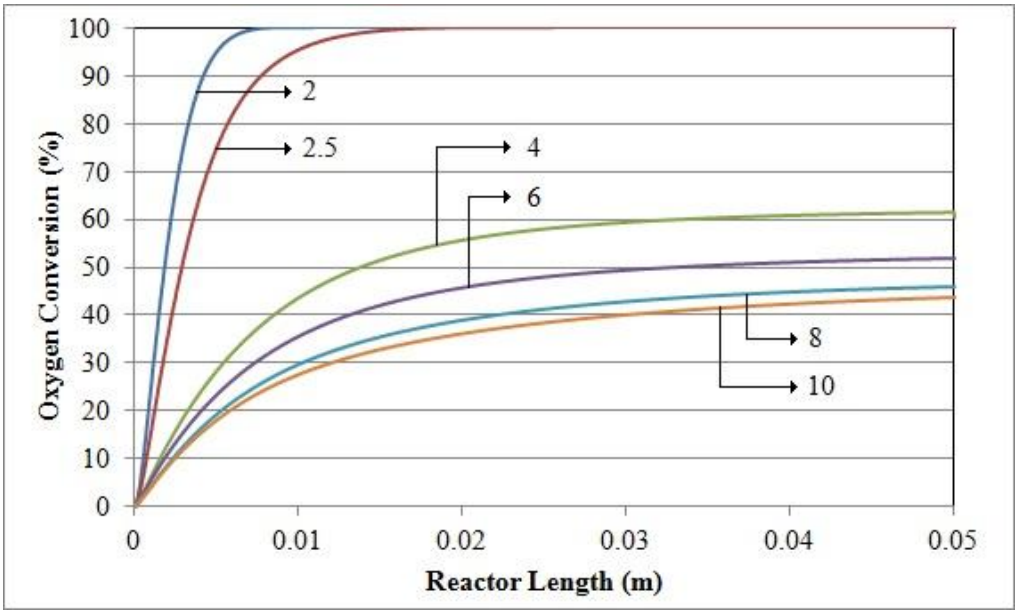

Figure 4.4. Effect of feed ratio on O_2 conversion along the reactor.

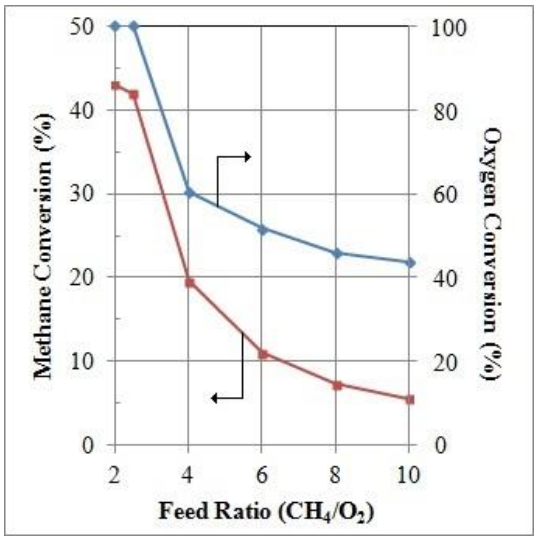

Figure 4.5. Effect of feed ratio on CH_4 and O_2 conversions.

The effects of feed ratio on ethylene selectivity and yield are given in Figure 4.6 and Figure 4.7, respectively. At feed ratio values of 4 and higher, the conversion of reactants decreases and, as a result, ethylene yield becomes very low. Feed ratios of 2 and 2.5 give higher ethylene selectivity and yield due to faster reactions and higher conversion (reaction rates are summarized in Figures A.1-10). The maximum ethylene selectivities observed for feed ratios 2 and 2.5 are 16% and 23%, respectively.

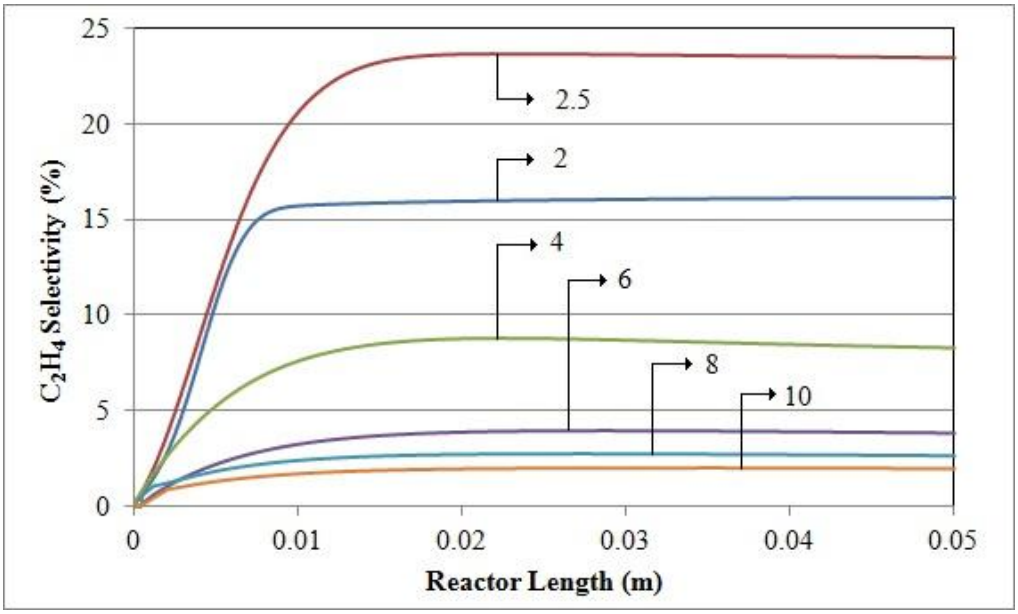

Figure 4.6. Effect of feed ratio on C_2H_4 selectivity along the reactor.

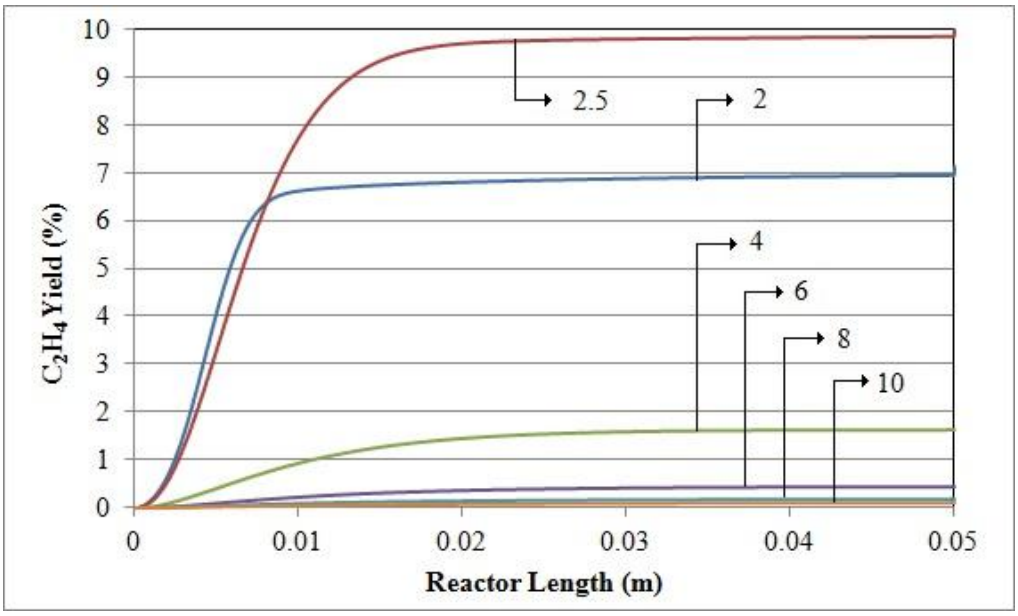

Figure 4.7. Effect of feed ratio on C_2H_4 yield along the reactor.

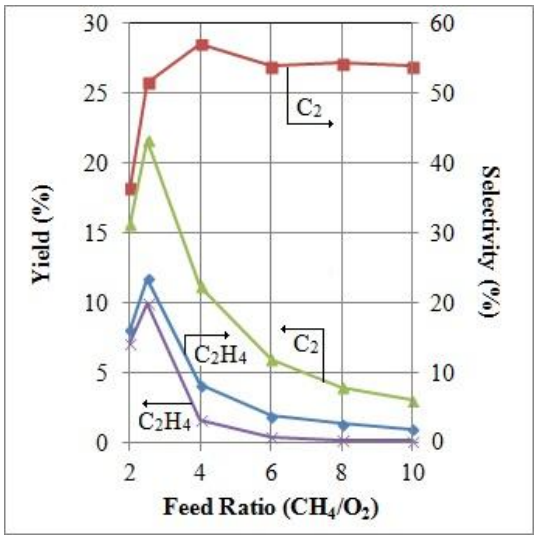

Figure 4.8. Effect of feed ratio on C_2H_4 and C_2 yields and selectivities.

It is observed from Figure 4.6 and Figure 4.7 that, for feed ratios of 2 and 2.5, the selectivity and yield values have similar trends until the first 1 cm part of the reactor. After this section, selectivity and yield of 2.5 feed ratio case continue to increase for the next 1 cm part of the reaction channel. Although the methane conversion in case of 2 feed ratio is higher, the selectivity and yield results in case 2.5 are better.

For total C_2 hydrocarbons similar trend is observed in yield values. As it can be seen from Figure 4.8 above the feed ratio of 2.5, the C_2 yield decreases markedly due to low conversion of reactants. However, the C_2 selectivity increases with increasing feed ratio as C_2 yield is reduced. This is because of the insufficient oxygen in the reaction resulting in low methane conversion. It is observed from the results that 2.5 is the optimum feed ratio value with good temperature distribution, highest C_2 hydrocarbons yield and highest ethylene selectivity and yield. When the ratio is 2, oxidation of C_2 products is favored due to high oxygen content in the feed. However, when the ratio is higher than 2.5, due to the low temperature profile, rates of reactions R2, R5 and R7 are lower and C_2 production is inhibited (Figures A.2, A.5 and A.7, respectively).

4.2. Effect of Reaction Channel Inlet Temperature

The effect of reaction inlet temperature is examined in a series of simulations. Temperature is increased 50 K in each step from 973 K to 1223 K. The maximum methane conversion obtained is 42% at 1023 K reaction inlet temperature, while the ethylene yield and selectivity are 9.9% and 23.5%, respectively in the same simulation. Maximum C_2 hydrocarbons yield is observed as 24% at 973 K inlet temperature.

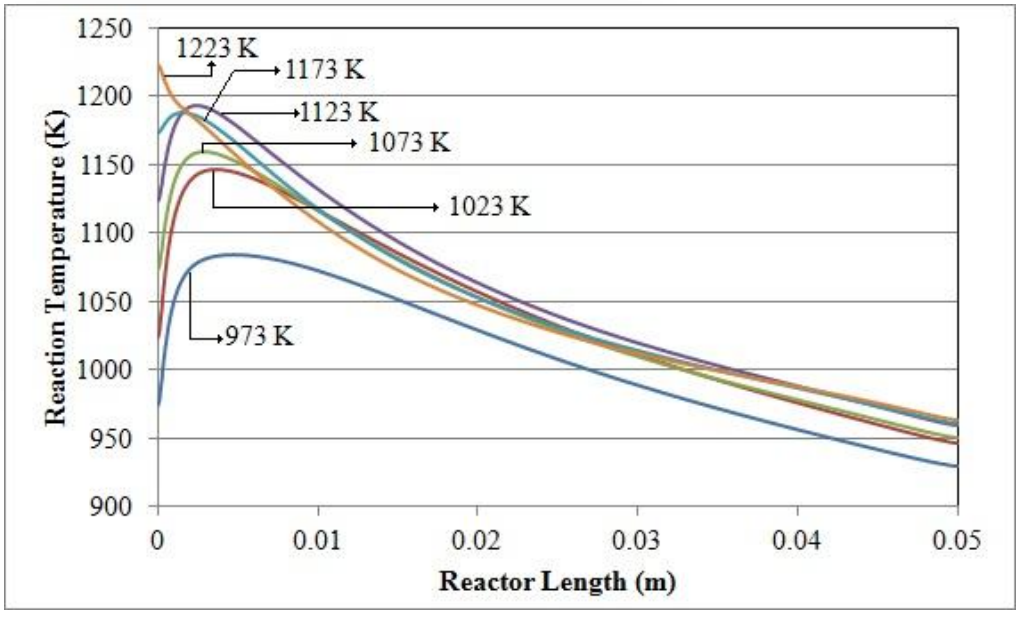

Figure 4.9. Effect of reactant inlet temperature on reaction temperature profile along the reactor.

The effects of OCM inlet temperature on reaction temperature, coolant temperature profiles and on the methane and oxygen conversions are given in Figures 4.9, 4.10, 4.11 and 4.12, respectively. It is observed that increasing inlet temperature does not affect methane conversion dramatically (Figure 4.11), but affects temperature profiles in the reaction channel. The maximum reaction temperature observed in these series of simulation is 1193 K with the 1123 K of reaction inlet temperature case in which the methane conversion has the lowest value as 37% among all cases (Figure 4.11). Reaction with 973 K inlet temperature can only reach to 83% oxygen conversion (Figure 4.12) which proves that reaction rates in this case are lower when compared to other cases as shown in Figures A.11-20.

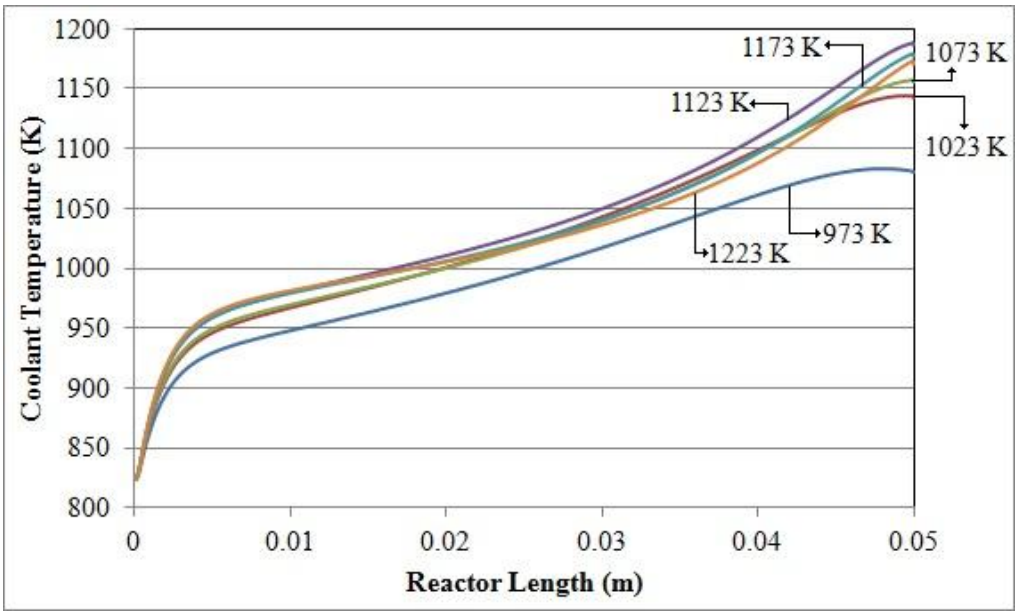

Figure 4.10. Effect of reactant inlet temperature on coolant temperature profile along the reactor.

When reaction inlet temperature is increased, reaction outlet temperatures are increased in the same order (Figure 4.9). However, the same trend is not valid for the maximum temperatures. It is seen that maximum temperatures of the reaction channel increase by increasing inlet temperature until 1123 K. Further increase from this value causes decrease in the maximum temperature. In the case of 1223 K reaction inlet temperature, temperature profile has a continuous decreasing pattern. These observations can be explained by the increasing temperature gradient between the cooling and the reaction channels. Exothermal heat of the OCM reaction have been absorbed by cooling channel starting from the very beginning of the reactor and the temperature cannot increase further.

Reaction inlet temperature does not have a dramatic impact on the cooling channel temperature profile, as shown in Figure 4.10. All profiles are close to each other except from that obtained at 973 K reaction inlet temperature. Since the reaction rates at 973 K of inlet temperature are low, the temperature profile of the entire unit cell becomes lower in this case when compared to other cases.

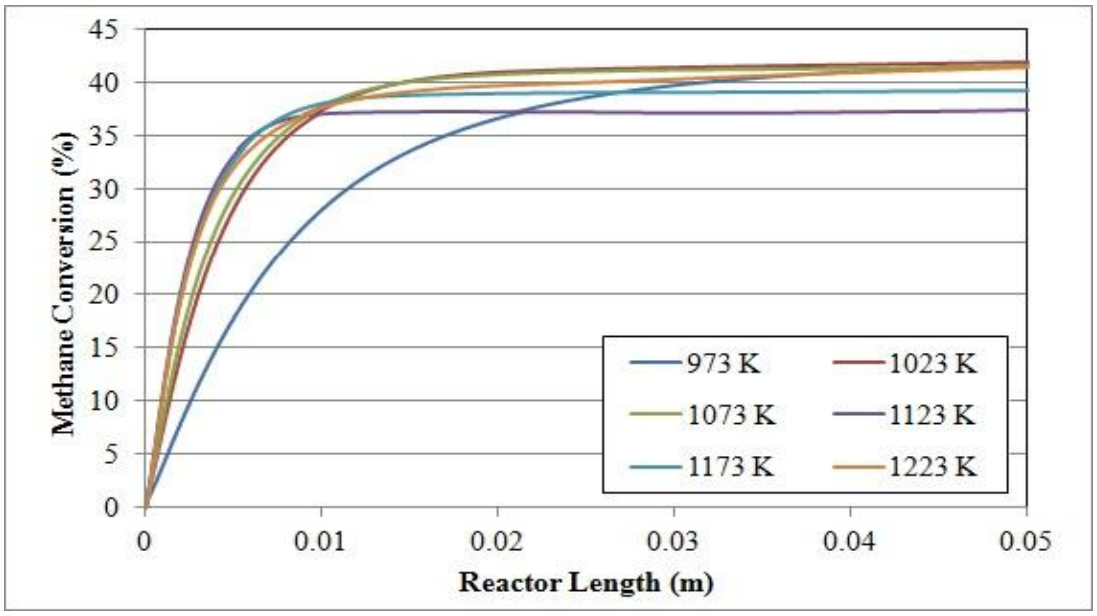

Figure 4.11. Effect of reactant inlet temperature on CH_4 conversion along the reactor.

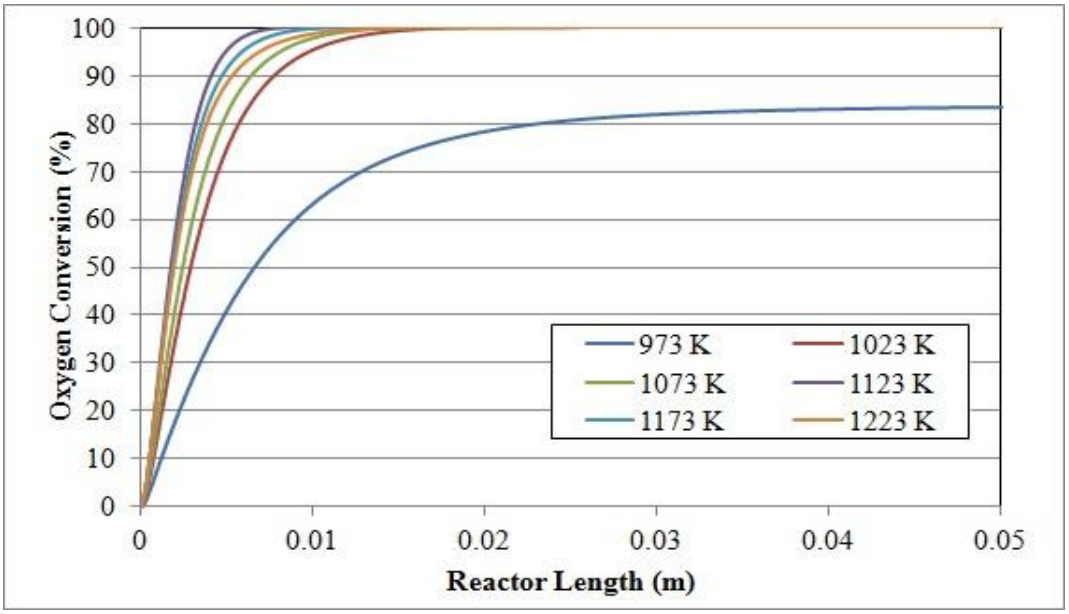

Figure 4.12. Effect of reactant inlet temperature on O_2 conversion along the reactor.

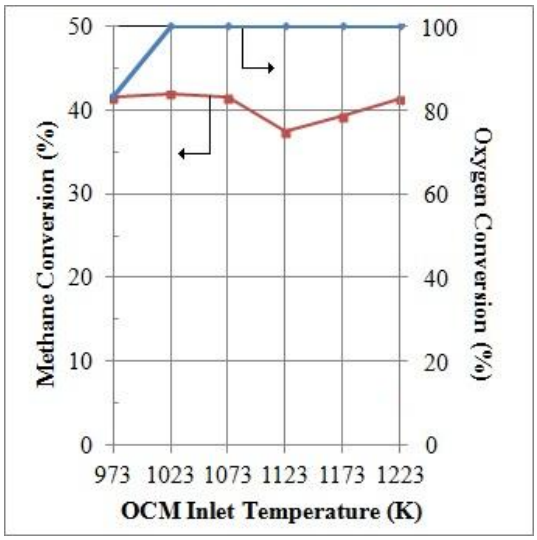

Figure 4.13. Effect of reactant inlet temperature on CH_4 and O_2 conversion.

The conversions of methane and oxygen against OCM inlet temperature and replotted in Figure 4.13. The lowest methane conversion of 37% is observed at 1123 K of reaction inlet temperature case. It is noticed from the oxygen conversion profile along the reactor length (Figure 4.12) that, at 1123 K of inlet temperature, oxygen reaches complete conversion faster that the other cases in the beginning of the reactor. After this point since there is no more oxygen, methane conversion could not increase further. The case with 973 K inlet temperature can only reach to 83% oxygen conversion due to the slow reaction rates which are summarized in Figures A.11-20.

The effects of inlet temperature on ethylene selectivity and yield are shown in Figure 4.14 and Figure 4.15, respectively. Highest ethylene selectivity and yield values are observed for the 1023 K inlet temperature case as 23.5% and 9.9%, respectively. Both yield and selectivity are found to respond similarly against changes in reaction inlet temperature. As the inlet temperature is increased from 973 K to 1023 K, both selectivity and yield increases. Further increase of inlet temperature results in a decrease in selectivity and yield until temperature of 1123 K. After 1123 K the ethylene selectivity and yield values start to increase again.

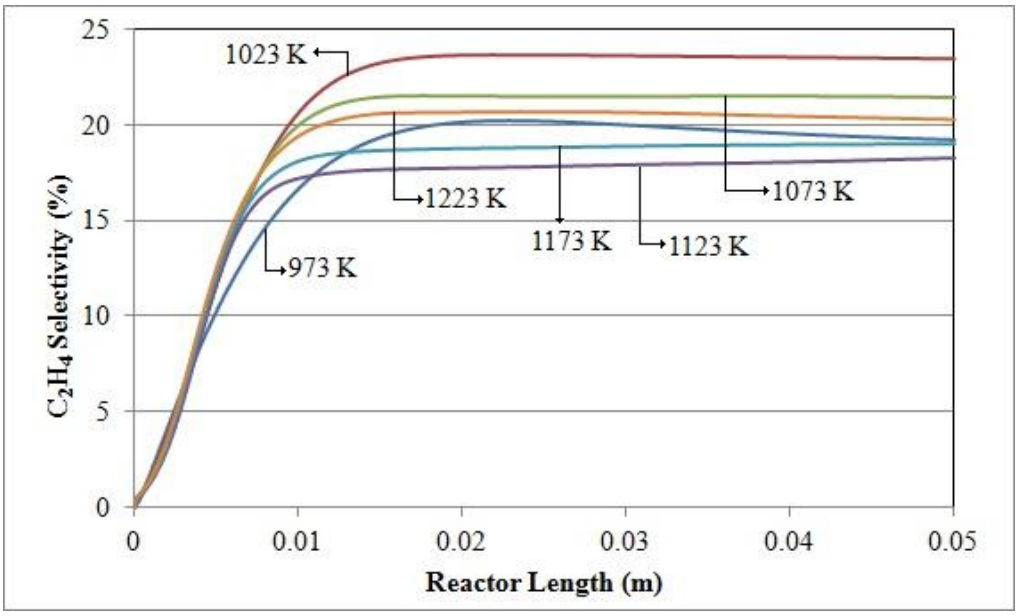

Figure 4.14. Effect of reactant inlet temperature on C_2H_4 selectivity along the reactor.

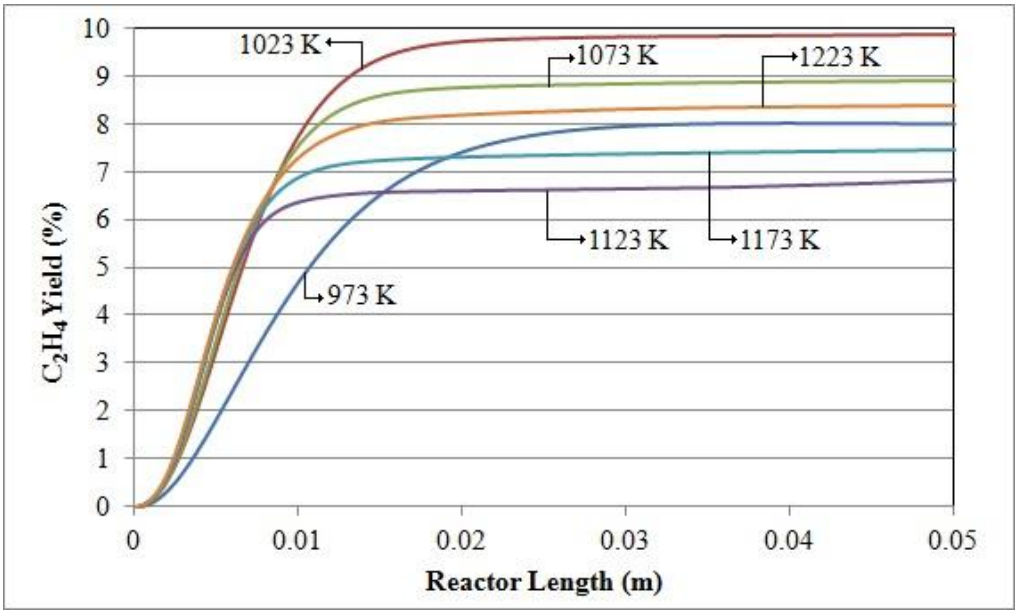

Figure 4.15. Effect of reactant inlet temperature on C_2H_4 yield along the reactor.

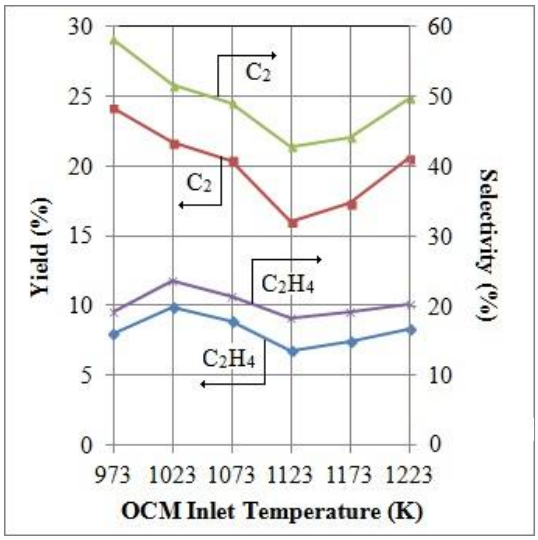

Figure 4.16. Effect of reactant inlet temperature on C_2H_4 and C_2 yields and selectivities.

The selectivity and yield outcomes of the reaction inlet parameter can be understand better if the reaction rates are investigated. Since the reaction with 973 K inlet temperature can only reach to 83% oxygen conversion, ethylene selectivity becomes low while total selectivity of C_2 products becomes the highest at 973 K. This can be proven by looking at the rates of dehydrogenation reactions of ethane (R5 and R7) in Figure A.15 and Figure A. 17 respectively. Rates of the reactions where ethylene is produced are at their lowest values at 973 K (Figure A.15 and Figure A.17). As the inlet temperature is increased up to 1123 K C_2 yield decreases (Figure 4.16). This is because oxidation of the hydrocarbons is favored at elevated temperatures as a result of higher reaction rates. But, further increase in inlet temperature speeds up the rate of ethane production (Figure A.12), while inhibiting other reactions in the mechanism, which result in an increase in C_2 selectivity and yield.

The optimum reaction inlet temperature for OCM reaction seems to be 1023 K, due to highest ethylene selectivity and yield values. The methane conversion does not affected dramatically by inlet temperature.

4.3. Effect of Cooling Channel Inlet Temperature

The importance of the cooling effect on the system is proved in a series of simulations. The steam inlet temperature is varied between 773 K and 873 K with 25 K increments. The maximum reaction temperature observed in these series of simulations is 1162 K for 873 K

cooling channel inlet temperature. Selectivity and yield of C_2 products have the maximum values as 57.7% and 22.8% respectively, at 798 K of coolant inlet temperature case. In the 823 K case, oxygen reaches complete conversion while methane conversion reaches 42%, its maximum value.

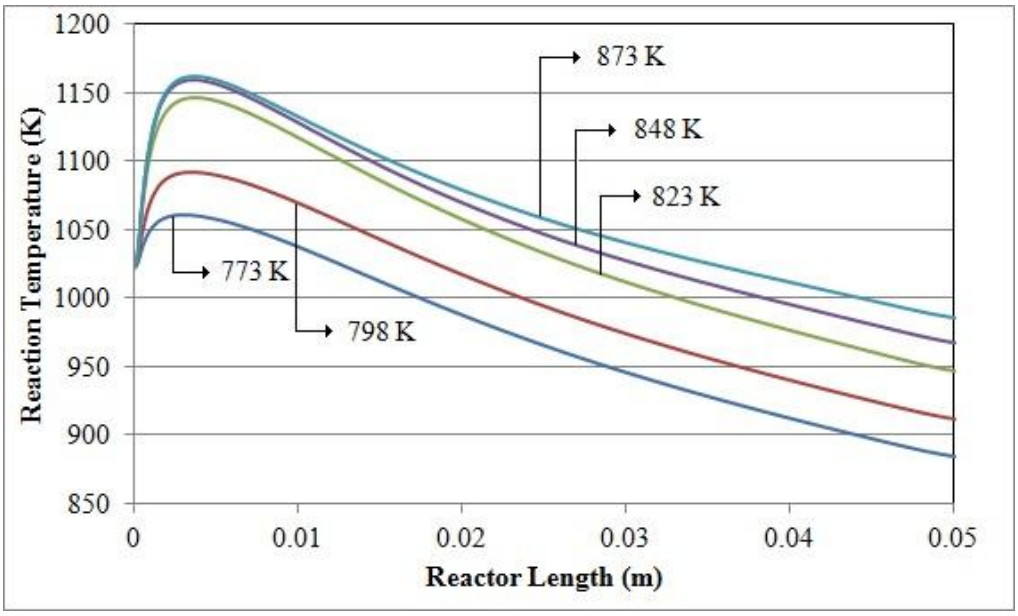

Figure 4.17. Effect of coolant inlet temperature on reaction temperature profile along the reactor.

The temperature profile of the reaction channel behaves as expected; maximum temperatures of the reaction channel increases as steam inlet temperature increases (Figure 4.17). This is because the heat loss from reaction channel is reduced due to lower temperature difference between reaction and cooling channels as the coolant inlet temperature increases. The same trend is observed in the reaction outlet temperatures due to same reason. Below 823 K of coolant inlet, temperature profile of the reaction channel is much lower from other case values due to over cooling of the entire unit cell. In the cooling channel, a similar trend in the outlet temperatures is observed. As steam inlet temperature increases, outlet temperatures of the cooling channels also increase (Figure 4.18).

An interesting finding of this parametric analysis is the temperature trends of the 848 K and 873 K of steam inlet cases. At the first 1 cm section of the reactor, the reaction channel temperature makes a maximum, where the temperature rises from 1023 K to 1162 K. At the top of this region, there is cooling steam having a temperature of 1162 K. When the steam

inlet temperature is increased from 848 K to 873 K, maximum temperature of the reaction channel does not increase and the same trend is observed in the cooling channel outlet temperature. This can be explained by looking at the oxygen conversion trends shown in Figure 4.19. For these two cases, oxygen is the limiting reactant and it reaches complete conversion in the entrance region. Due to lack of oxygen in the channel, the reaction cannot proceed so the maximum temperature or the reaction cannot increase even though average cooling channel temperature increases.

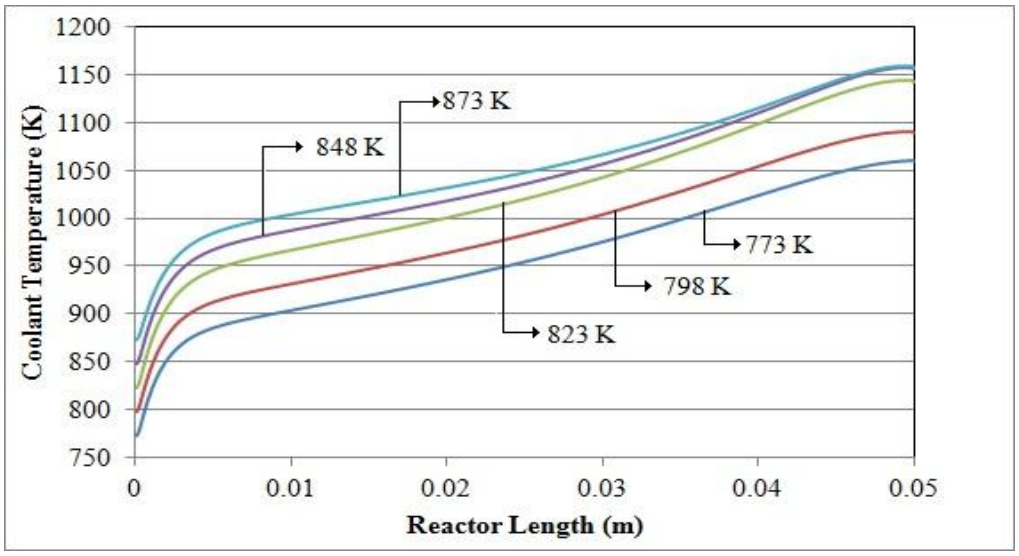

Figure 4.18. Effect of coolant inlet temperature on coolant temperature profile along the reactor.

The response of methane conversion against coolant inlet temperature is shown in Figure 4.20. Conversion trends can be explained by the changes in the reaction temperature given in Figure 4.17. A temperature rise of approximately 270 K is achieved in each case. Below 823 K of coolant inlet, however, temperature profile of the reaction channel is much lower from above values due to over cooling of the entire channel. This is why the conversion of the reactants is lower below 823 K (Figure 4.20).

From steam inlet temperature 773 K to 823 K, conversions of oxygen and methane increases gradually. The oxygen conversion is very low at steam inlet temperatures of 773K and 798 K due to over cooling of the reaction channel (Figure 4.21). In 823 K of steam inlet, oxygen reaches complete conversion while methane conversion reaches its maximum value of 42%. Further increase of coolant inlet temperature causes methane conversion to drop

slightly. As average reactor temperature increases, oxidation of C_2 products into carbon oxides increases. The increase of carbon oxides in the reactor inhibits ethane formation reaction from methane which causes a slight decrease in methane conversion at coolant temperatures higher than 823 K.

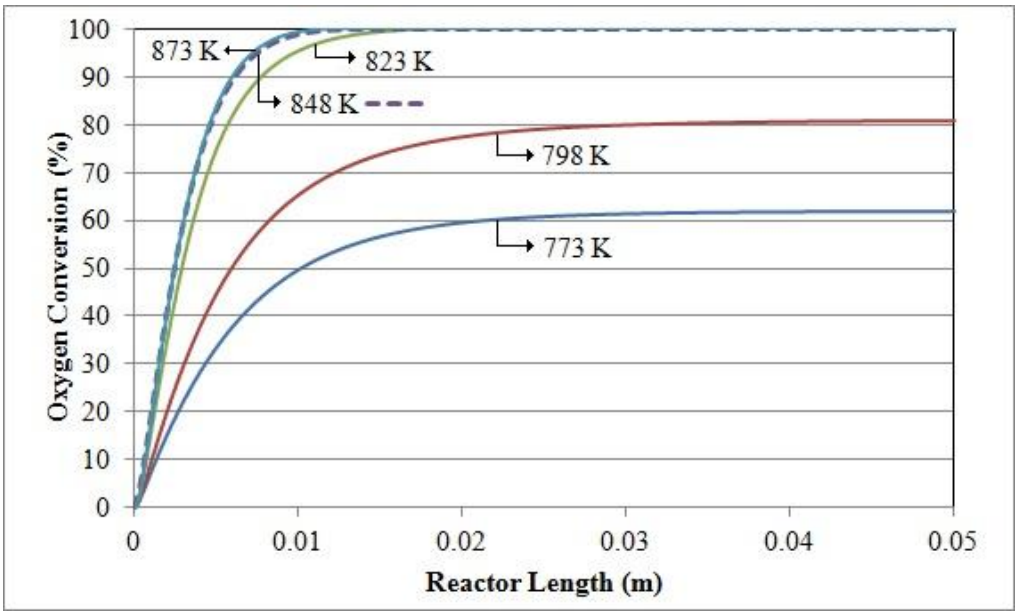

Figure 4.19. Effect of coolant inlet temperature on O_2 conversion along the reactor.

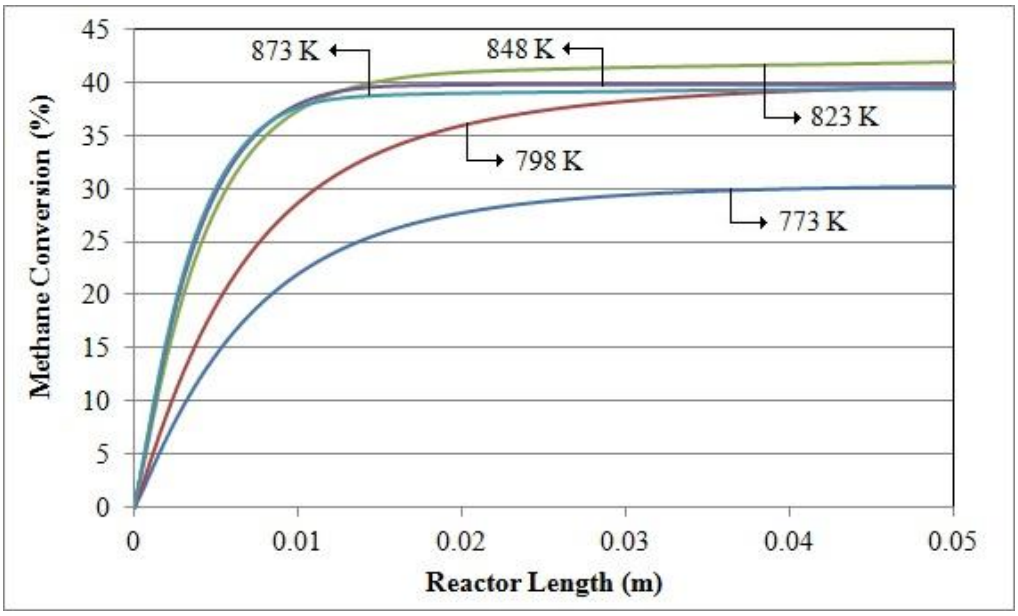

Figure 4.20. Effect of coolant inlet temperature on CH_4 conversion along the reactor.

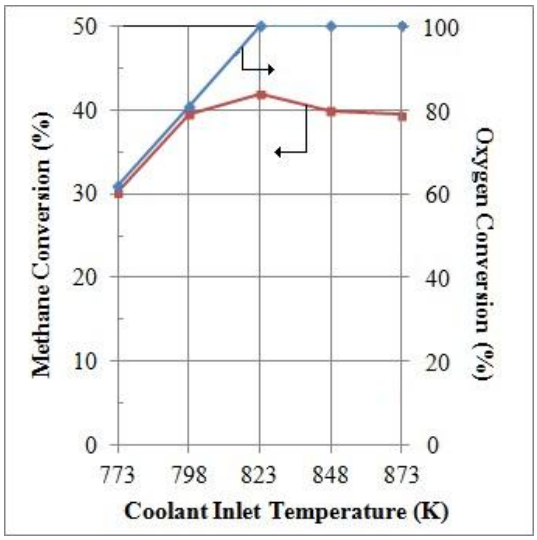

Figure 4.21. Effect of coolant inlet temperature on CH_4 and O_2 conversion.

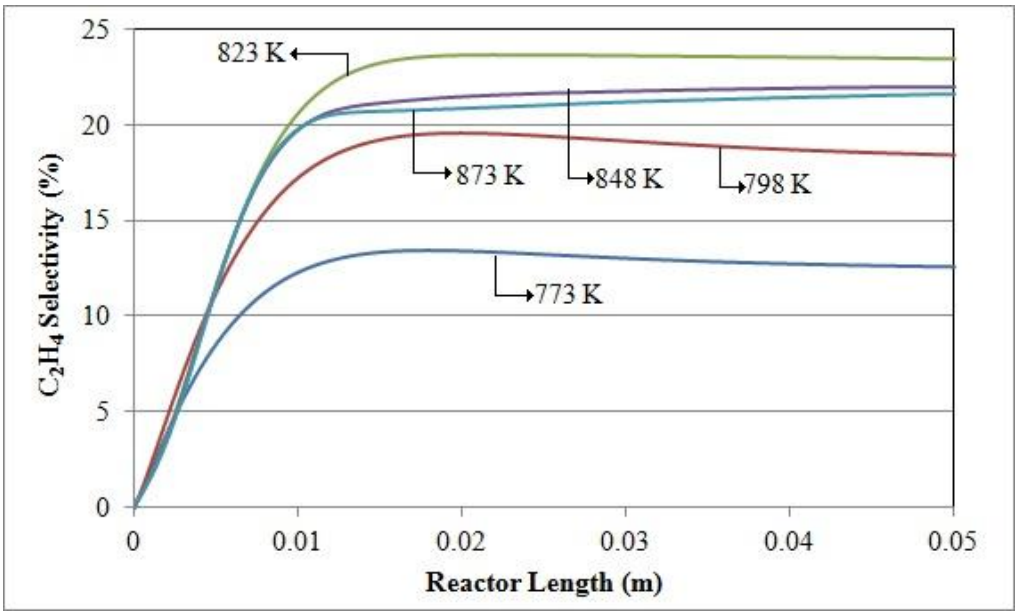

Figure 4.22. Effect of coolant inlet temperature on C_2H_4 selectivity along the reactor.

The effects of steam inlet temperature on ethylene selectivity and yield are shown in Figure 4.22 and Figure 4.23, respectively. Ethylene selectivity and yield have the same trend with the coolant inlet temperature. As steam temperature is increased from 773 K to 823 K, ethylene selectivity and yield reached their maximum values of 23.5% and 9.9%, respectively. Further increase in the steam temperature minimizes the cooling effect on the OCM reaction, which results in higher average reaction temperature, higher oxidation of C_2 hydrocarbons and lower ethylene selectivity and yield values. Another observation on ethylene selectivity is for cases of 773 K and 798 K of steam inlet. At these temperatures ethylene selectivity slightly

decreases after reaching a maximum along the reactor length (Figure 4.22). This is due to the presence of unreacted oxygen in the reaction channel, which triggers oxidation of ethylene towards the end of the reactor.

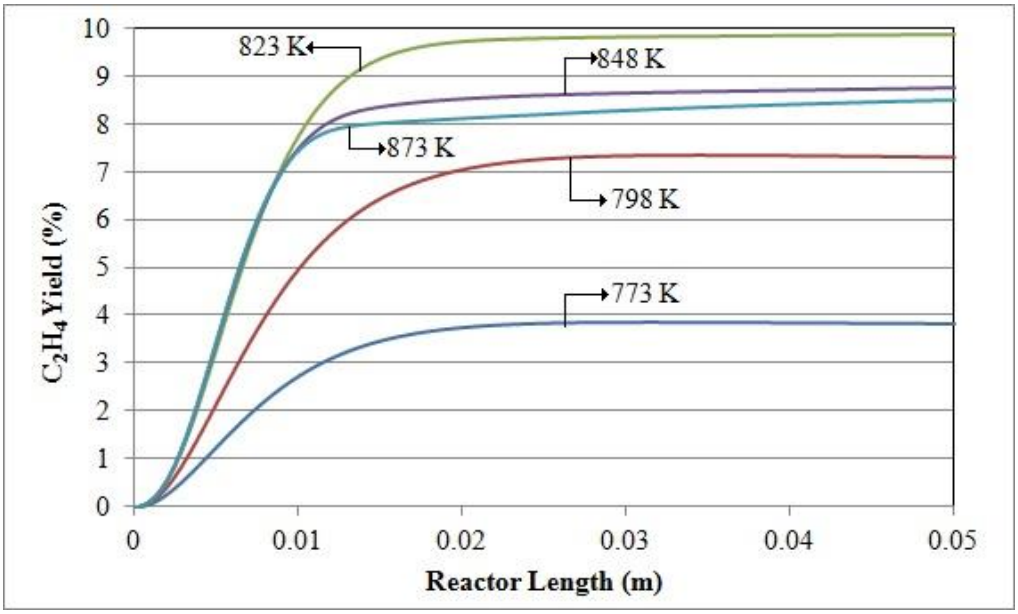

Figure 4.23. Effect of coolant inlet temperature on C_2H_4 yield along the reactor.

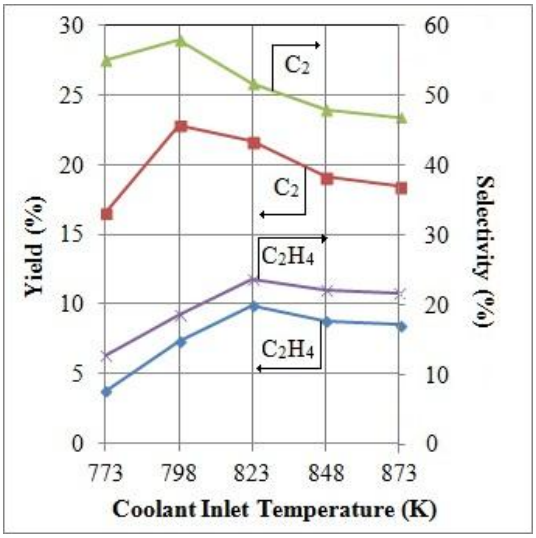

Figure 4.24. Effect of coolant inlet temperature on C_2H_4 and C_2 yields and selectivities.

Selectivity and yield of C_2 products have the maximum values of 57.7% and 22.8% respectively, at the 798 K case (Figure 4.24). Further increase in coolant temperature causes decomposition of C_2 products into carbon oxides, which decreases C_2 selectivity. On the other hand, it is observed that ethylene selectivity and yield values, 23.5% and 9.9% respectively,

are maximum at the coolant inlet temperature of 823 K, while C_2 selectivity and yield are highest at 798 K. This is because at 823 K, reaction rates of the reactions R5 and R7 in which ethylene is produced from ethane, are much higher than the rates in 798 K case (Figure A.25 and Figure A.27, respectively).

4.4. Effect of Reaction Channel Mass Flow Rate

Results of the simulations presenting the effects of reaction channel mass flow rate are summarized in this subsection. Mass flow rate of reaction channel is varied between 3 x 10^{-6} kg s^{-1} and 6 x 10^{-6} kg s^{-1}. The molar feed ratio, the catalyst weight and the channel layer thickness are kept constant. Therefore in order to change mass flow rate, linear velocity of the reactant flow is varied. The details like linear velocity values corresponding to each mass flow rate are given in Section 3.3. The operating and structural parameters with the numerical results of the simulations are summarized in appendix section in more detail.

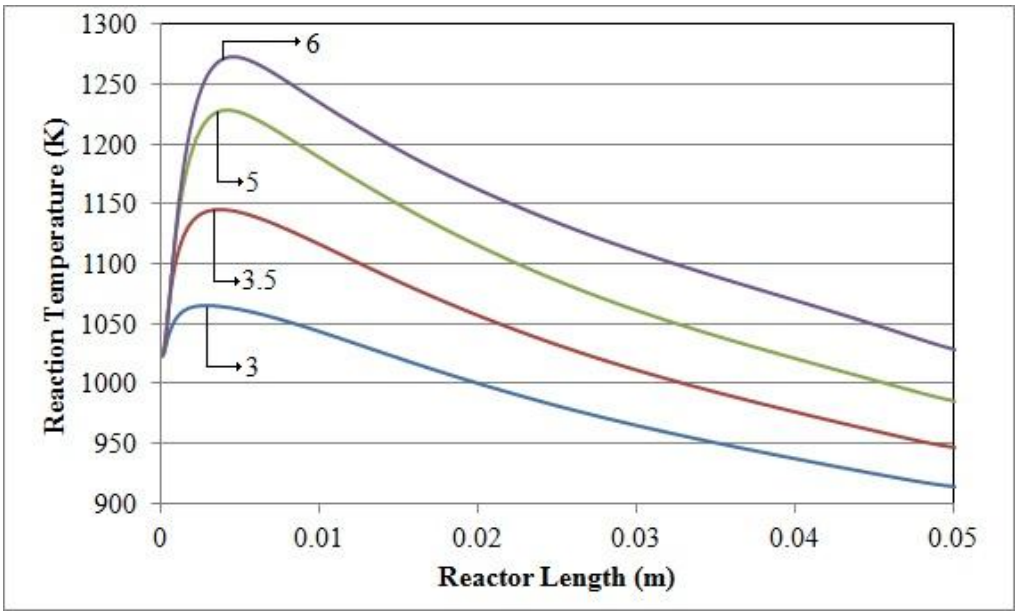

Figure 4.25. Effect of reaction channel mass flow rate on reaction temperature along the reactor.

As it is presented in Figure 4.25, the effect of reaction channel mass flow rate on temperature has a systematic pattern. As the mass flow rate is increased, the maximum and the outlet temperatures of the reaction channel are increased due to increasing heat load of the reacting flow. The maximum reaction temperature in these series of simulations is observed

for OCM mass flow rate of 6 x 10^{-6} kg s^{-1} as 1272 K which is quite higher than the temperature range of OCM found in the literature [19]. The outlet temperature of reaction channel at the same flow rate is 1027 K which is very close to inlet temperature. In this case, the heat load of the reactants dominates the cooling effect and the exit temperature cannot go below that inlet.

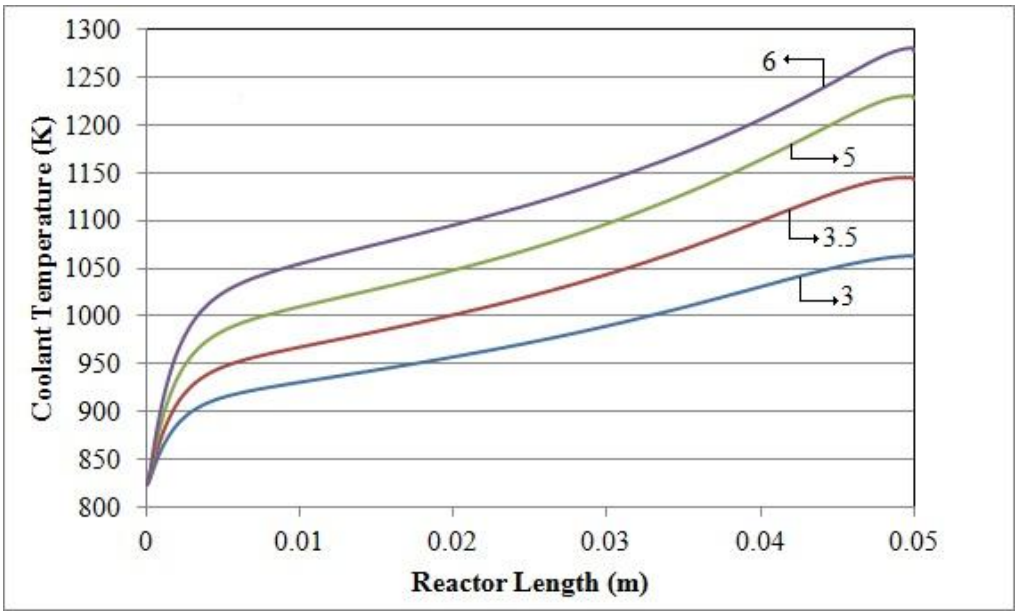

Figure 4.26. Effect of reaction channel mass flow rate on coolant temperature along the reactor.

The effect of reaction channel mass flow rate on the cooling channel temperature profile is given in Figure 4.26. A similar trend with reaction channel is also observed for cooling channel. As reactant mass flow rate increases, the outlet temperatures of steam in the cooling channel increases. The temperature difference between the inlet and outlet of the cooling channel is also increasing from ca. 240 K to 460 K as the reactant mass flow rate increases. The increase of mass flow rate result in higher heat load of reactants, which is absorbed by cooling steam. As a result, a continuously increasing trend of temperature in the cooling channel is observed.

In the mass flow rate of 3 x 10^{-6} kg s^{-1} case, oxygen conversion is 72%, the material amount in the reactor cannot compensate the heat required to reach full conversion of oxygen in the system (Figure 4.28). The conversion of methane reaches a maximum value of 42%, at 3.5 x 10^{-6} kg s^{-1} of reactant flow rate. Further increase in reactant mass flow rate decreases the

methane conversion because at high mass flow rates oxygen reaches complete conversion faster than other cases as shown in Figure 4.28 due to higher heat load of the reacting flow. Lack of oxygen in the reactor is the reason for low methane conversion at reactant mass flow rates of 5 x 10^{-6} kg s^{-1} and 6 x 10^{-6} kg s^{-1}.

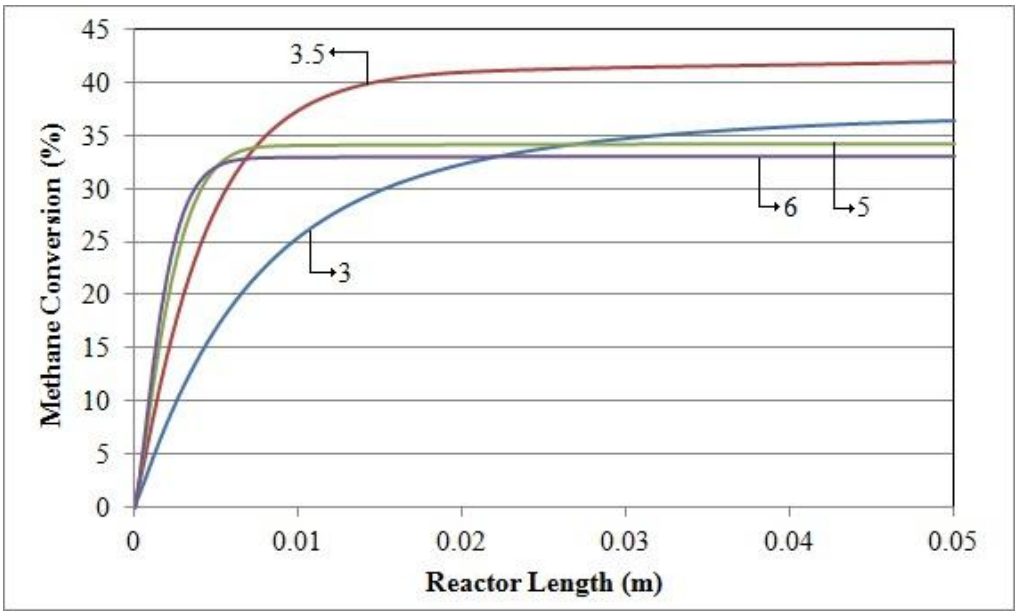

Figure 4.27. Effect of reaction channel mass flow rate on CH_4 conversion along the reactor.

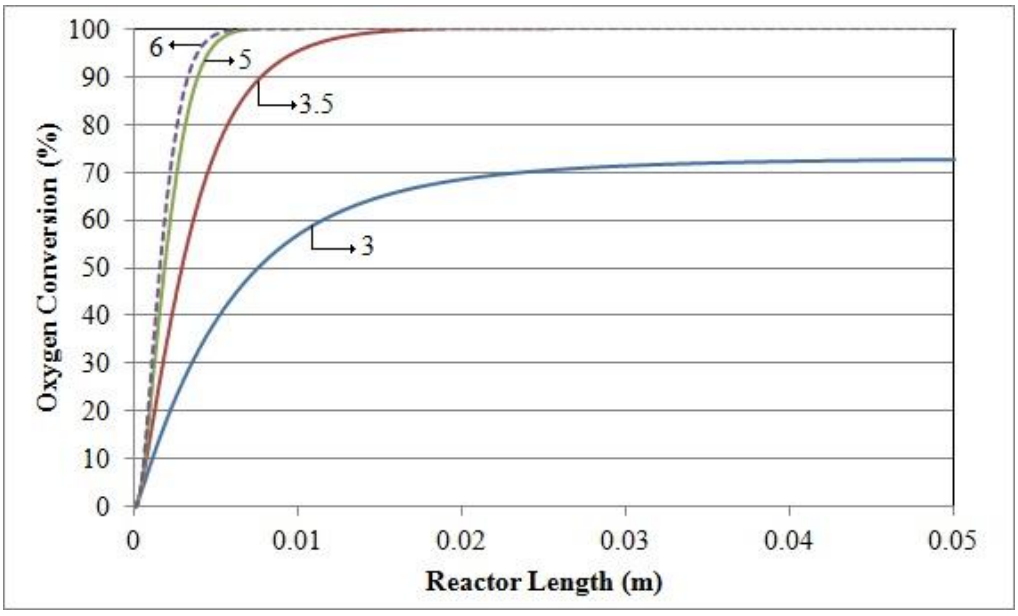

Figure 4.28. Effect of reaction channel mass flow rate on O_2 conversion along the reactor.

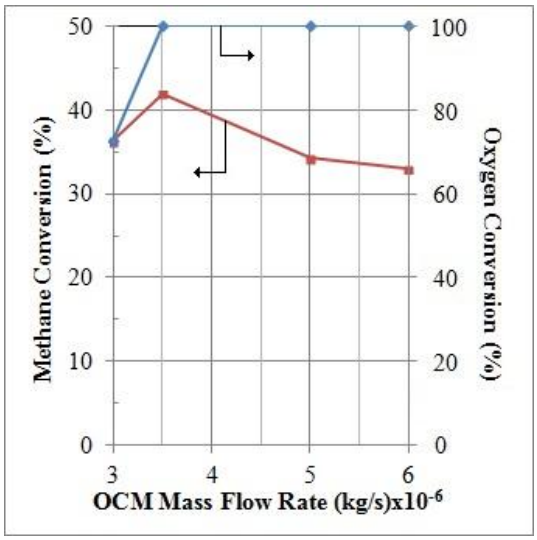

Figure 4.29. Effect of reaction channel mass flow rate on CH_4 and O_2 conversion.

The effect of reaction channel mass flow rate on ethylene selectivity and yield are presented in Figure 4.30 and Figure 4.31. The maximum ethylene selectivity and yield of 23.5% and 9.9% are achieved for 3.5 x 10^{-6} kg s^{-1} of reaction channel mass flow rate, respectively. As the reactant mass flow rate increases, heat load of the reacting flow also increases which results in higher average temperature of reaction channel. At elevated reaction temperatures oxidation of C_2 hydrocarbons becomes favorable. This explains the lower ethylene yield and selectivity at higher reaction channel mass flow rate values of 5 x 10^{-6} kg s^{-1} and 6 x 10^{-6} kg s^{-1}.

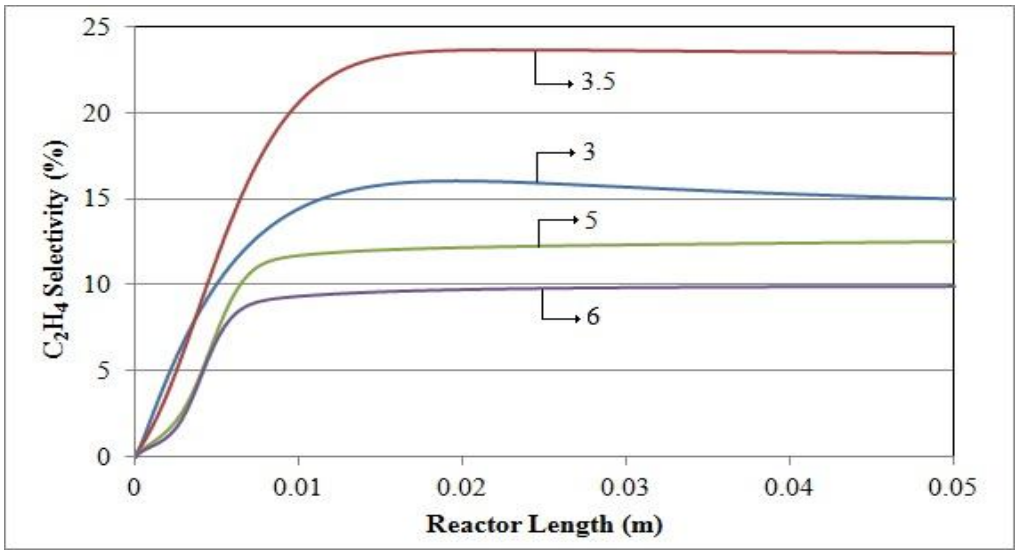

Figure 4.30. Effect of reaction channel mass flow rate on C_2H_4 selectivity along the reactor.

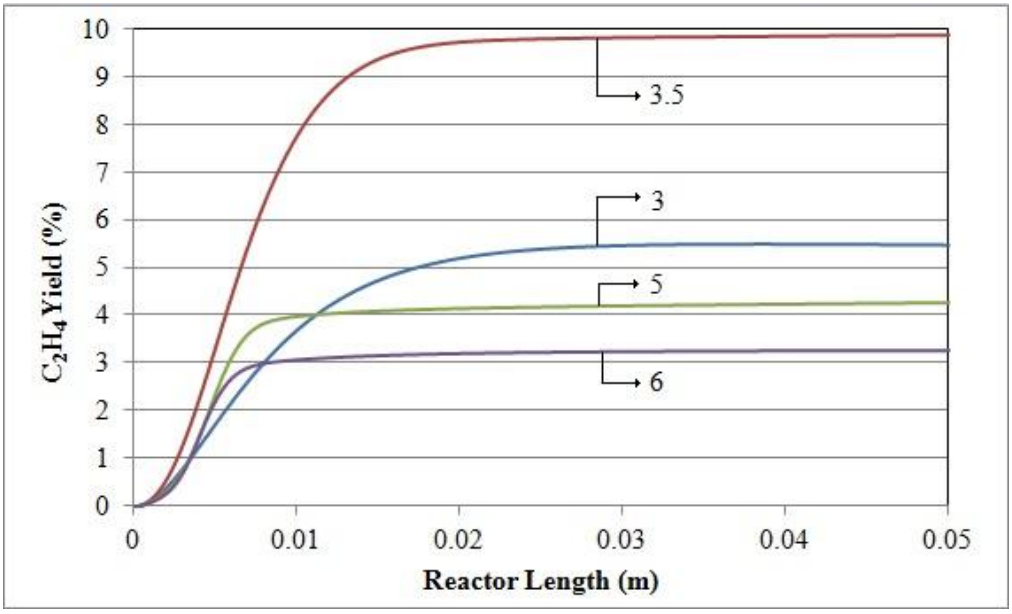

Figure 4.31. Effect of reaction channel mass flow rate on C_2H_4 yield along the reactor.

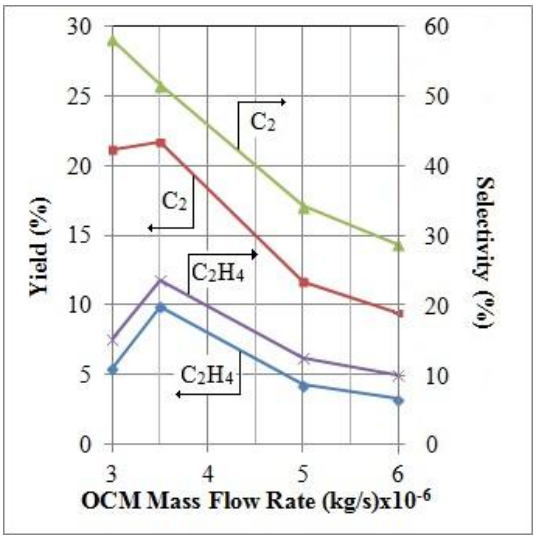

Figure 4.32. Effect of reaction channel mass flow rate on C_2H_4 and C_2 yields and selectivities.

The response of selectivity and yield values at different reaction channel mass flow rates are given in Figures 4.30-4.32. The selectivity and yield of ethylene, and yield of C_2 products are 23.5%, 9.9% and 21.6%, respectively, all of which are at their maximum values for reactant flow rate of 3.5 x 10^{-6} kg s^{-1}. Above this flow rate, ethylene selectivity decreases due to decomposition into carbon oxides. The same trend is, however, not valid for the selectivity of all C_2 products; the C_2 selectivity has a maximum value, 58%, at 3 x 10^{-6} kg s^{-1} of reactant mass flow rate and decreases with increasing flow rate (Figure 4.32). The reason

for this behavior is that at 3 x 10^{-6} kg s^{-1} of reactant flow rate, oxygen conversion is 72%. The main product of methane and oxygen is ethane in this condition, and as reactant mass flow rate is increased, the additional oxygen converted is mainly used in the decomposition of ethane into ethylene. To conclude, the optimum value of reaction channel mass flow rate seems to be 3.5 x 10^{-6} kg s^{-1} with good temperature distribution, highest methane conversion and yield values.

4.5. Effect of Cooling Channel Mass Flow Rate

Coolant mass flow rate is studied as another parameter due to the importance of residence time of steam in the reactor. The effect of coolant mass flow rate on the reaction performance is shown in Figures 4.33-4.40. Mass flow rate of cooling channel is increased gradually from 0.5 x 10^{-6} to 1.5 x 10^{-6} kg s^{-1} keeping the channel thickness constant at 6 x 10^{-4} m. The superficial velocity of cooling channel is varied in order to change the mass flow rate of the steam in the cooling channel. The details like linear velocity values corresponding to each mass flow rate are given in Section 3.3. The operation and structural parameters with the numerical results of the simulations are summarized in Appendix A in more detail.

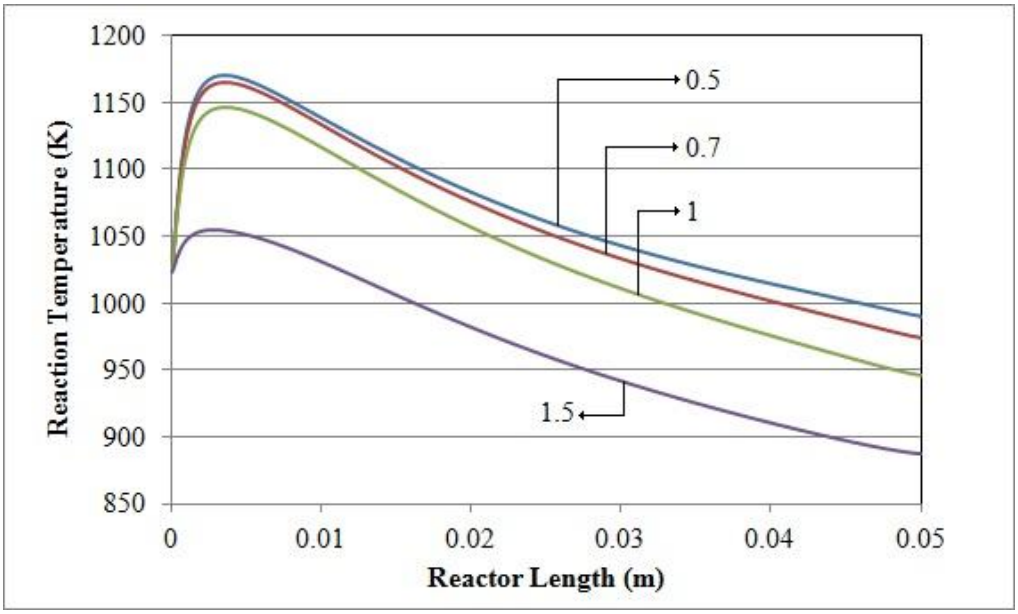

Figure 4.33. Effect of coolant mass flow rate on reaction temperature along the reactor.

Temperature profiles of the reaction channel show that increasing the coolant mass flow rate results in a decrease in outlet temperatures as well as the maximum temperatures (Figure 4.33). High amounts of steam absorb more exothermal heat from the reaction channel. Thus, average temperature of the reaction channel decreases, reducing the reaction rates at the same time.

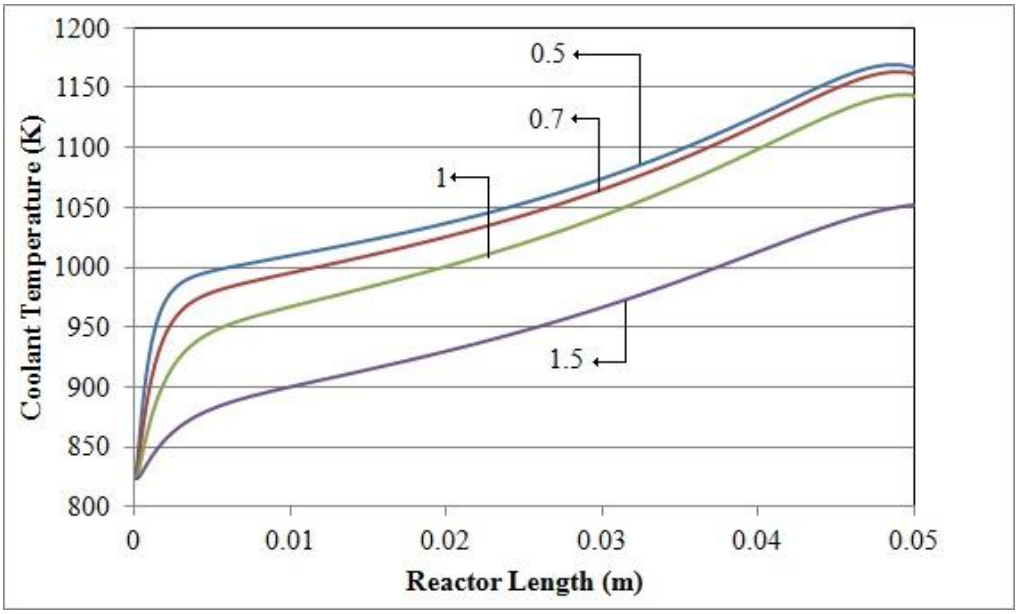

Figure 4.34. Effect of coolant mass flow rate on coolant temperature along the reactor.

The maximum reaction temperature observed in these series of simulations is 1170 K for 0.5 x 10^{-6} kg s^{-1} of coolant mass flow rate. In this flow rate, the outlet temperature of the reaction is 990 K, which is close to the inlet temperature of the reaction channel. An important detail seen from Figure 4.33 is the decreasing difference between the maximum temperatures of the different cases. As the steam flow rate decreases, the difference between the maximum temperatures and the outlet temperatures of the reactions decreases. In cases of steam mass flow rate below 0.5 x 10^{-6} kg s^{-1}, probably the outlet temperature of the reaction channel will come closer to the inlet temperature.

The effect of steam mass flow rate on the cooling channel temperature profile is given in Figure 4.34. A similar trend with reaction channel is also observed for cooling channel. As coolant mass flow rate increases, the outlet temperatures of steam in the cooling channel decrease. The temperature difference between the inlet and outlet of the cooling channel is

also decreasing from approximately 350 K to 230 K as the coolant mass flow rate increases. The results show that as the mass flow rate of cooling channel increases, steam is more likely to maintain its colder nature. Consequently, temperature of OCM reaction cannot reach higher levels, avoiding the reactions to proceed.

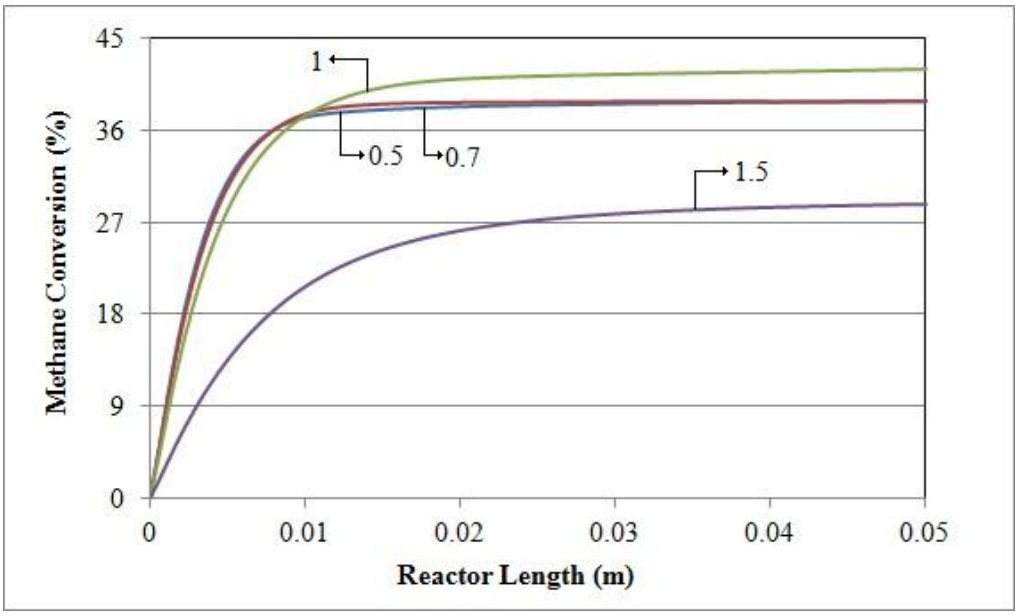

Figure 4.35. Effect of coolant mass flow rate on CH_4 conversion along the reactor.

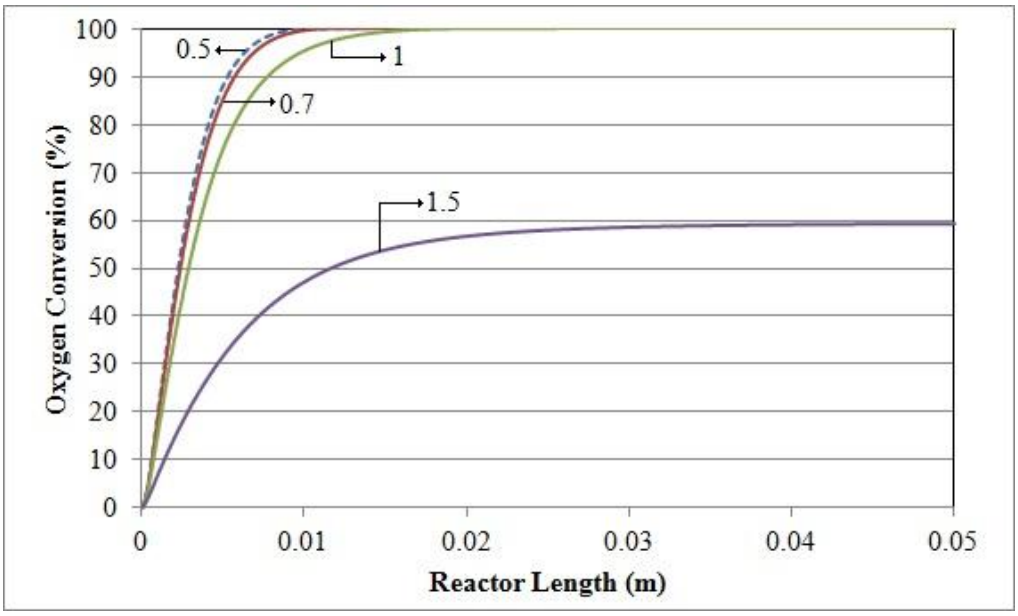

Figure 4.36. Effect of coolant mass flow rate on O_2 conversion along the reactor.

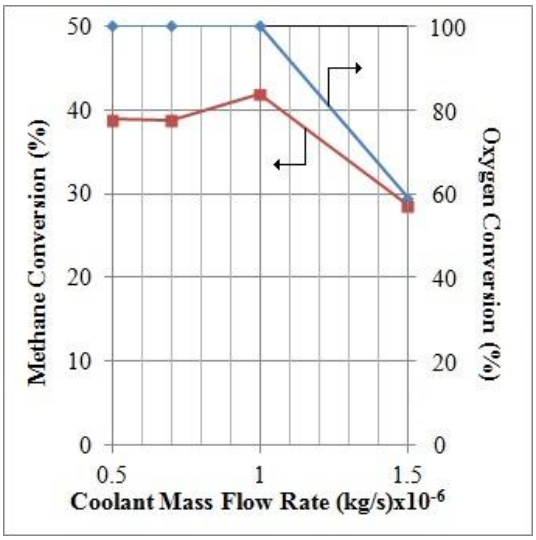

Figure 4.37. Effect of coolant mass flow rate on CH_4 and O_2 conversion.

The effect of cooling channel mass flow rate on the methane and oxygen conversions are presented in Figures 4.35-4.37. When steam mass flow rate is lower than 1 x 10^{-6} kg s^{-1} methane consuming reactions become faster, and the oxygen reaches 100% conversion more quickly in the reactor. Thus, methane conversions cannot increase further due to lack of oxygen in the reactor (Figure 4.35). When the steam flow rate is above 1 x 10^{-6} kg s^{-1}, over-cooling of the reaction channel avoids the reactions to proceed. Therefore, oxygen can only reach 60% conversion in cooling channel mass flow rate of 1.5 x 10^{-6} kg s^{-1}.

The ethylene production performance is also affected by coolant mass flow rate. Highest ethylene selectivity and yield values are obtained for steam mass flow rate of 1 x 10^{-6} kg s^{-1} as seen in Figure 4.38 and Figure 4.39. Increasing cooling channel mass flow rate up to 1 x 10^{-6} kg s^{-1} increases the ethylene yield. This means, consecutive oxidation reactions are controlled with better cooling of the reaction channel. However, further increase in steam mass flow rate results in much lower yield of ethylene. This is because the reaction mechanism cannot proceed due to over cooling of the reaction channel.

The optimum value for cooling channel mass flow rate is found to be 1 x 10^{-6} kg s^{-1} with the highest methane conversion, 42%, as well as with the highest ethylene selectivity, ethylene yield and C_2 products yield of, 23.5%, 9.9% and 21.6%, respectively. It can be observed from the Figure 4.40 that, when the steam mass flow rate is low, further oxidation of

C_2 products into carbon oxide products occurs due to higher average reaction temperatures. Thus, C_2 hydrocarbon selectivity and yield values are lower than the optimum case.

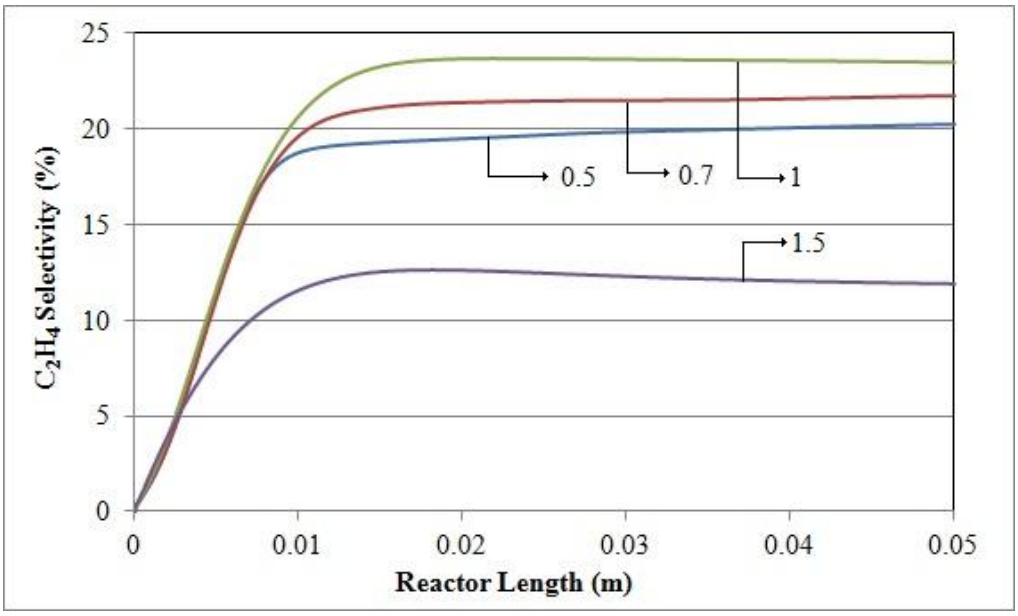

Figure 4.38. Effect of coolant mass flow rate on C_2H_4 selectivity along the reactor.

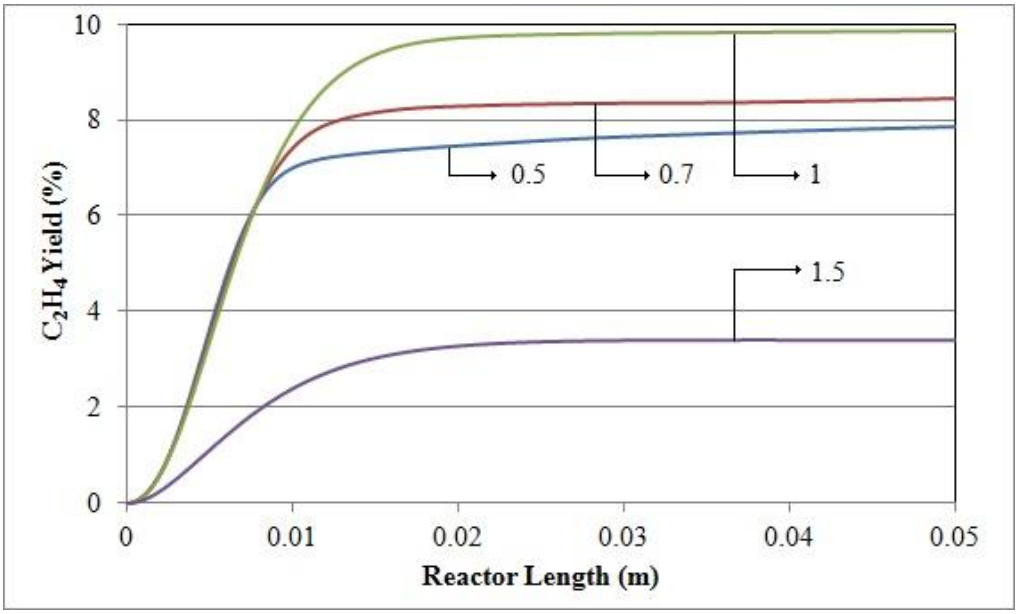

Figure 4.39. Effect of coolant mass flow rate on C_2H_4 yield along the reactor.

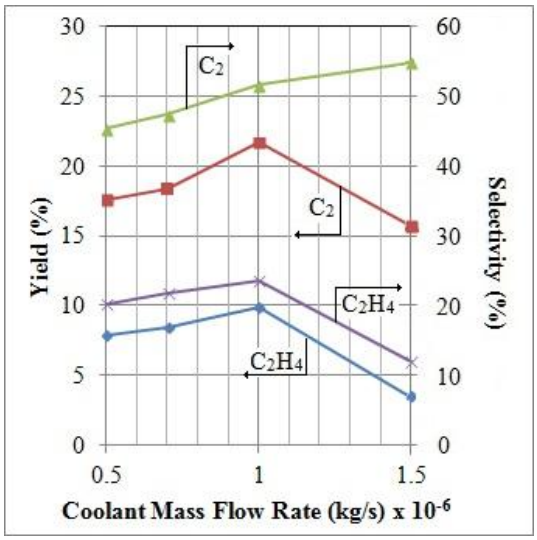

Figure 4.40. Effect of coolant mass flow rate on C_2H_4 and C_2 yields and selectivities.

Coolant mass flow rates higher than 1 x 10^{-6} kg s^{-1} also result in low C_2 yield due to low conversion of the reactants. However, as ethylene selectivity decreases, C_2 selectivity continues to increase. This simply shows that, conversion of ethane to ethylene is slower at steam flow rate of 1.5 x 10^{-6} kg s^{-1}.

4.6. Effect of Wall Material

The impact of wall material on the reaction performance is investigated. For this purpose, three different materials, alumina, AISI steel and silicon carbide, with different thermal conductivities are used in simulations. Although they have higher thermal conductivities, materials like copper and aluminum are not suitable for this system due to their mechanical properties. Since OCM reaction has high range of temperature applications, copper and aluminum are not considered as an option in this series of simulations.

The effect of wall material on temperature profiles along the reactor length is presented in Figures 4.41-4.43. Results show that as the thermal conductivity of the wall material increases, the maximum temperature of the reaction decreases while the reaction outlet temperature increases. For better interpretation of the results, heat flux through OCM catalyst washcoat to the wall is also plotted. The operation and structural parameters with the numerical results of the simulations are tabled in Appendix A in more detail.

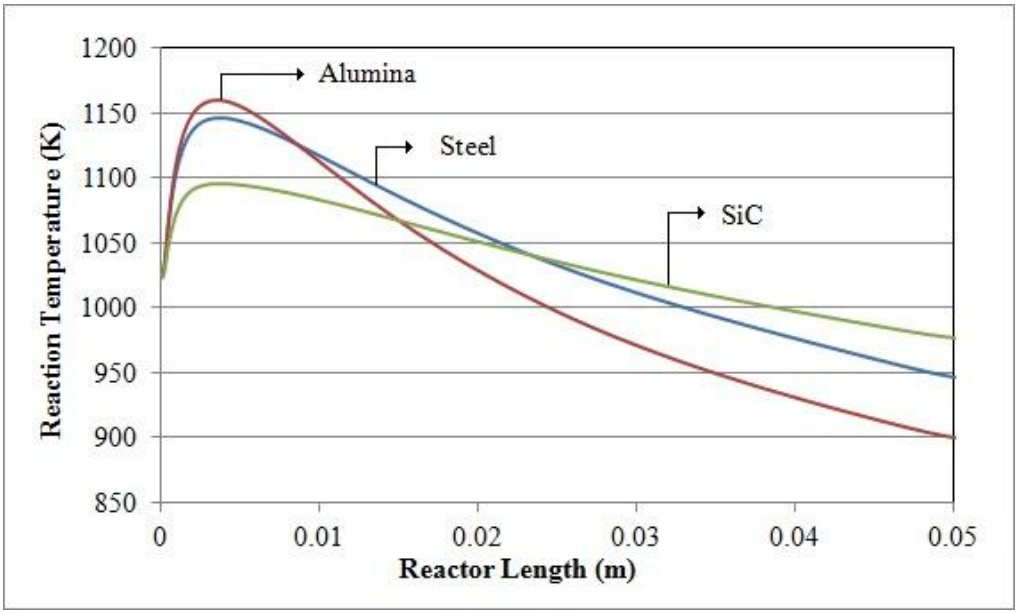

Figure 4.41. Effect of wall material on reaction channel temperature profile along the reactor (Simulated wall material types: Alumina (k_w=27 W m^{-1} K^{-1}), AISI Steel (k_w=44.5 W m^{-1} K^{-1}), Silicon carbide (k_w=87 W m^{-1} K^{-1})).

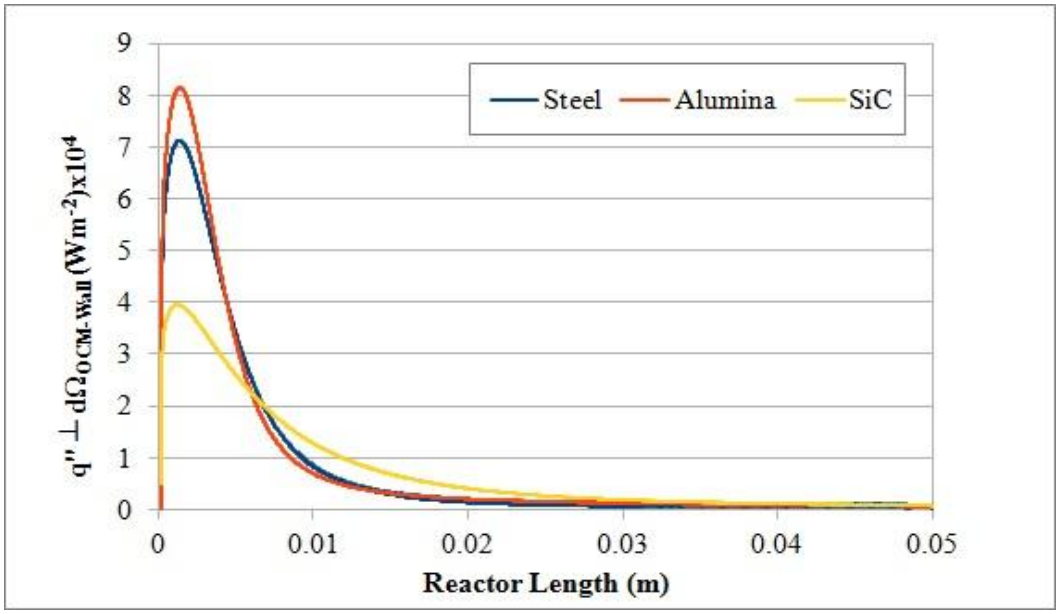

Figure 4.42. The normal component of the heat flux through the OCM washcoat-wall interface (Simulated wall material types: Alumina (k_w=27 W m^{-1} K^{-1}), AISI Steel (k_w=44.5 W m^{-1} K^{-1}), Silicon carbide (k_w=87 W m^{-1} K^{-1})).

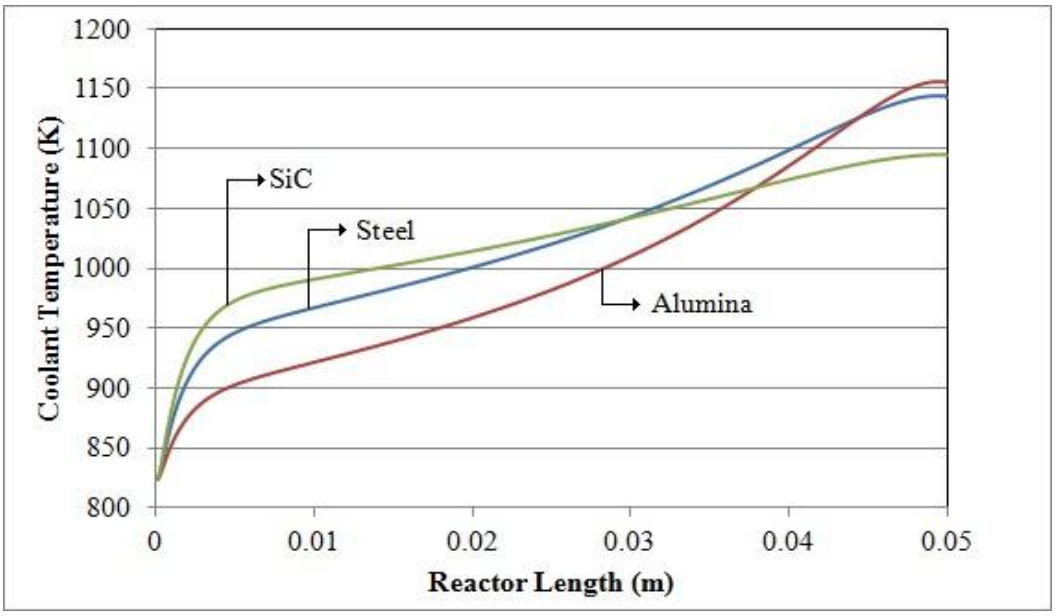

Figure 4.43. Effect of wall material on cooling channel temperature profile along the reactor (Simulated wall material types: Alumina (k_w=27 W m^{-1} K^{-1}), AISI Steel (k_w=44.5 W m^{-1} K^{-1}), Silicon carbide (k_w=87 W m^{-1} K^{-1})).

The maximum reaction temperature is observed for alumina as 1159 K. The temperature profiles become flatter when thermal conductivity of the wall material is higher. This trend can be explained by looking at the behavior of heat flux from the OCM channel to the wall along reactor length (Figure 4.42). At the very beginning of the reactor the heat flux is greatest for the material with the lowest thermal conductivity. In the region of 0.6 cm to 2 cm, it is observed that axial conduction inside the wall starts to dominate the conduction through the interface, and the wall with higher thermal conductivity facilitates higher heat flux. In the wall with highest thermal conductivity the axial conduction is improved. As a result it spreads the heat from reaction channel over the entire reactor and the temperature profile becomes flatter. The outlet temperature of the case with silicon carbide wall material is 976 K which is close to the inlet temperature of 1023 K. The advanced cooling over the reaction channel in this case, provides a ‘near-isothermal’ operating condition for OCM reaction.

While controlling the exothermal heat in the reaction channel, steam temperature increases about 270 K for silicon carbide wall material case. In Figure 4.43 the cooling channel temperature profiles for different wall materials are presented. Similar to the reaction channel temperature profile, silicon carbide wall has flatter temperature profile in the cooling

channel. As the thermal conductivity of the wall material increases, the temperature profile becomes flatter, and cooling effect on the reaction channel is enhanced.

Methane and oxygen conversion results which are presented in Figures 4.44-4.46 directly reflect the improvement of the reaction channel temperature profile. In the reactor with silicon carbide wall methane conversion is maximum at 46.8% while the oxygen reaches a conversion of 94%.

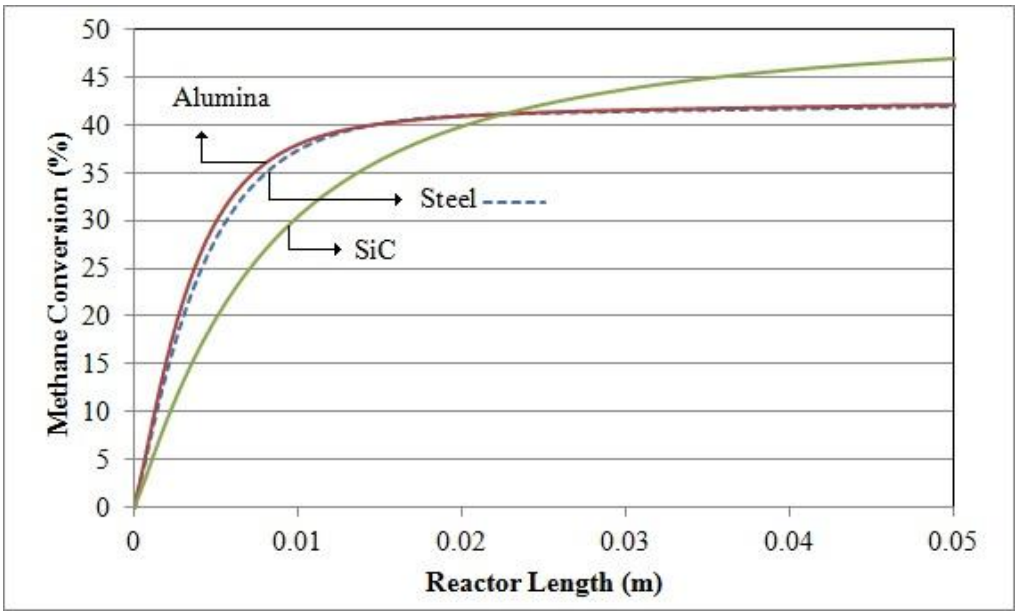

Figure 4.44. Effect of wall material on CH_4 conversion along the reactor (Simulated wall material types: Alumina (k_w=27 W m^{-1} K^{-1}), AISI Steel (k_w=44.5 W m^{-1} K^{-1}), Silicon carbide (k_w=87 W m^{-1} K^{-1})).

The effect of wall material on ethylene selectivity and yield are represented in Figure 4.47 and Figure 4.48. Highest ethylene selectivity and yield values are observed for silicon carbide wall case, as 23.9% and 11.2%, respectively. The most important observation of this subject is the extensive increase of the selectivity and yield of ethylene along the reactor length. For wall materials with lower thermal conductivities, ethylene yield values increases more quickly up to their maximum point, due to rapid reactions. However, in silicon carbide wall, the reaction continues to proceed almost until the end of the reactor, as we can also see from methane conversion result in Figure 4.44. Although the reaction temperature is lower in average, the conversion and yield values are improved in the case of silicon carbide wall.

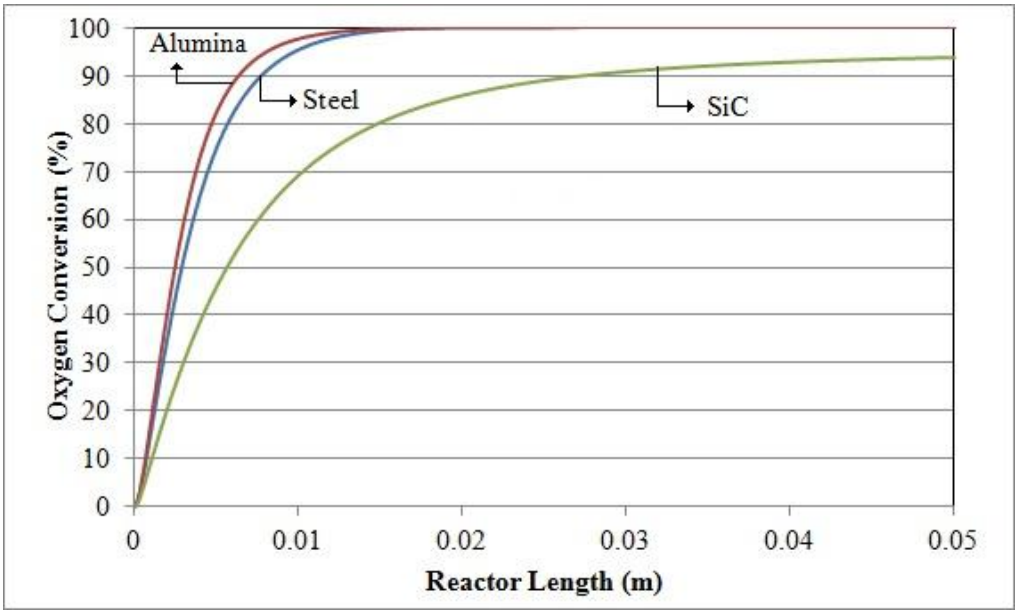

Figure 4.45. Effect of wall material on O_2 conversion along the reactor (Simulated wall material types: Alumina (k_w=27 W m^{-1} K^{-1}), AISI Steel (k_w=44.5 W m^{-1} K^{-1}), Silicon carbide (k_w=87 W m^{-1} K^{-1})).

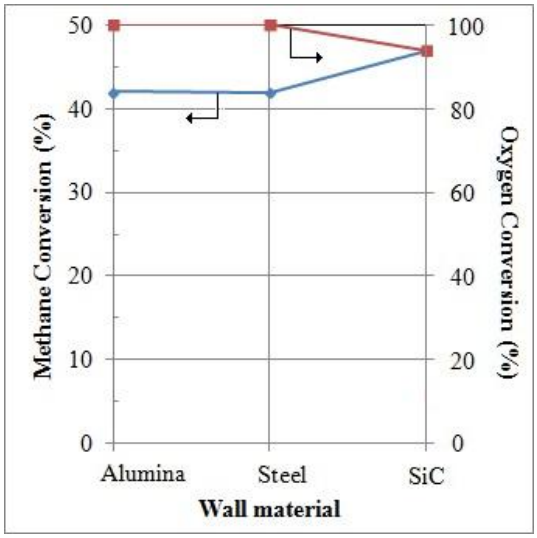

Figure 4.46. Effect of wall material on CH_4 and O_2 conversion (Simulated wall material types: Alumina (k_w=27 W m^{-1} K^{-1}), AISI Steel (k_w=44.5 W m^{-1} K^{-1}), Silicon carbide (k_w=87 W m^{-1} K^{-1})).

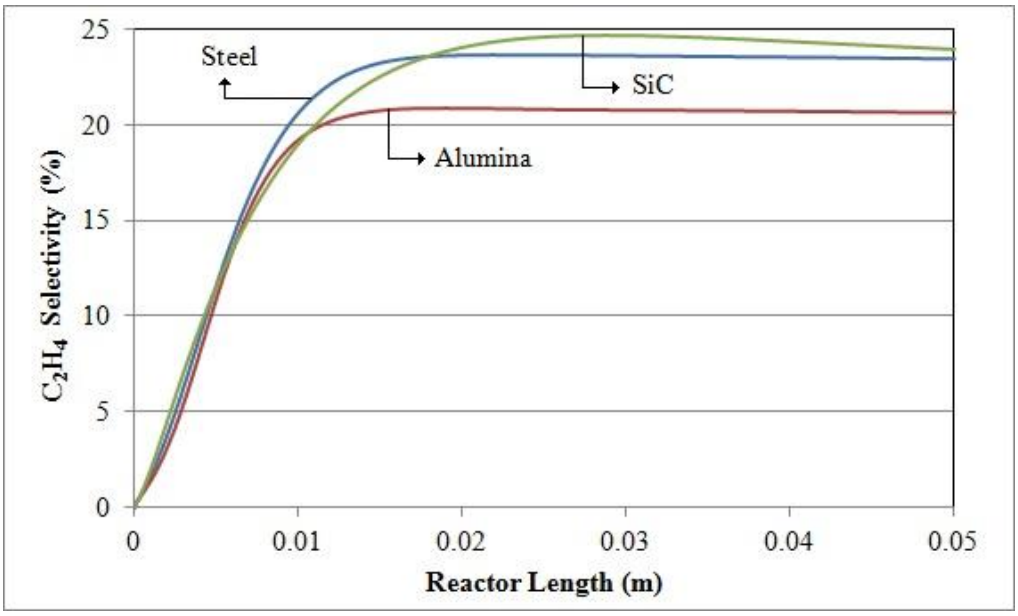

Figure 4.47. Effect of wall material on C_2H_4 selectivity along the reactor (Simulated wall material types: Alumina (k_w=27 W m^{-1} K^{-1}), AISI Steel (k_w=44.5 W m^{-1} K^{-1}), Silicon carbide (k_w=87 W m^{-1} K^{-1})).

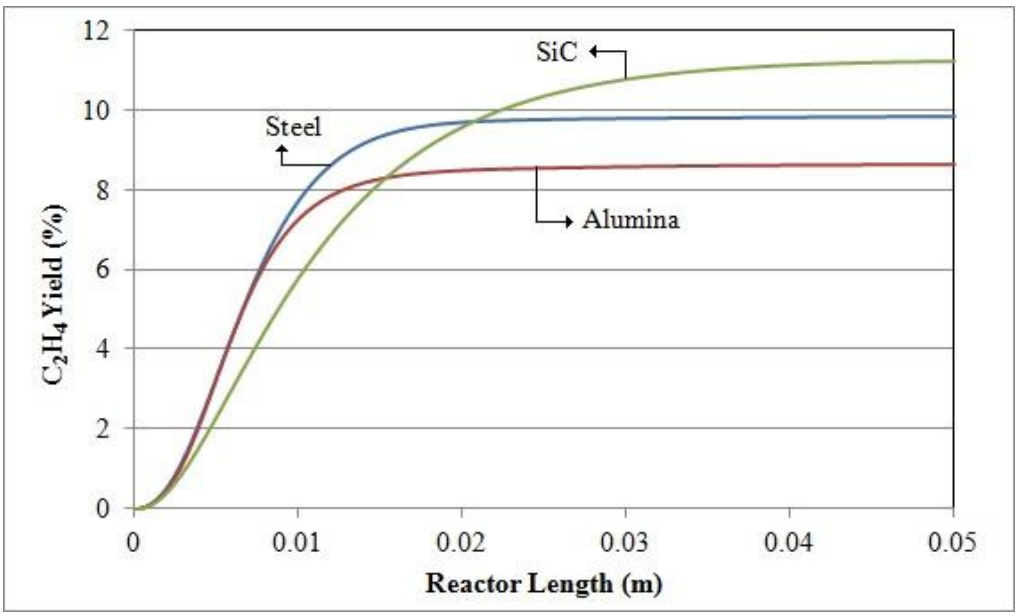

Figure 4.48 Effect of wall material on cooling C_2H_4 yield along the reactor (Simulated wall material types: Alumina (k_w=27 W m^{-1} K^{-1}), AISI Steel (k_w=44.5 W m^{-1} K^{-1}), Silicon carbide (k_w=87 W m^{-1} K^{-1})).

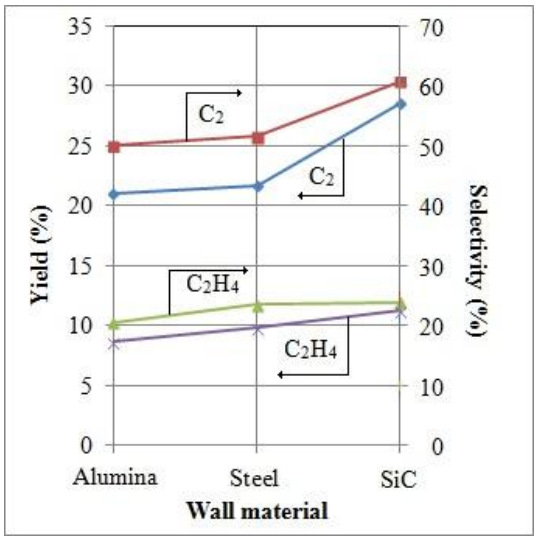

Figure 4.49. Effect of wall material on C_2H_4 and C_2 yields and selectivities (Simulated wall material types: Alumina (k_w=27 W m^{-1} K^{-1}), AISI Steel (k_w=44.5 W m^{-1} K^{-1}), Silicon carbide (k_w=87 W m^{-1} K^{-1})).

As we can see from the Figure 4.49, the C_2 hydrocarbon production is highly improved with the use of silicon carbide wall. The selectivity and yield of C_2 products increased by 18% and 32%, respectively, when silicon carbide is used instead of steel. This shows that improved reaction temperature control not only improves ethylene production but also ethane production to a large extent. The maximum values of C_2 selectivity and yield achieved are 60.8% and 23.9%, respectively for silicon carbide wall material.

4.7. Effect of Wall Thickness

Wall thickness is observed as the final parameter of the reaction performance. The thickness of the separating wall is varied between 200 and 600 μm with 100 μm increments. In this case data of the heat flux through OCM catalyst washcoat to the wall is also plotted for better interpretation of the results. The operation and structural parameters with the numerical results of the simulations are tabled in Appendix A in more detail.

The effects of the wall thickness on the reaction and cooling channel temperature profiles are shown in Figure 4.50 and Figure 4.51, respectively. It is observed that outlet temperatures of the reaction channel increases as the wall thickness increases.

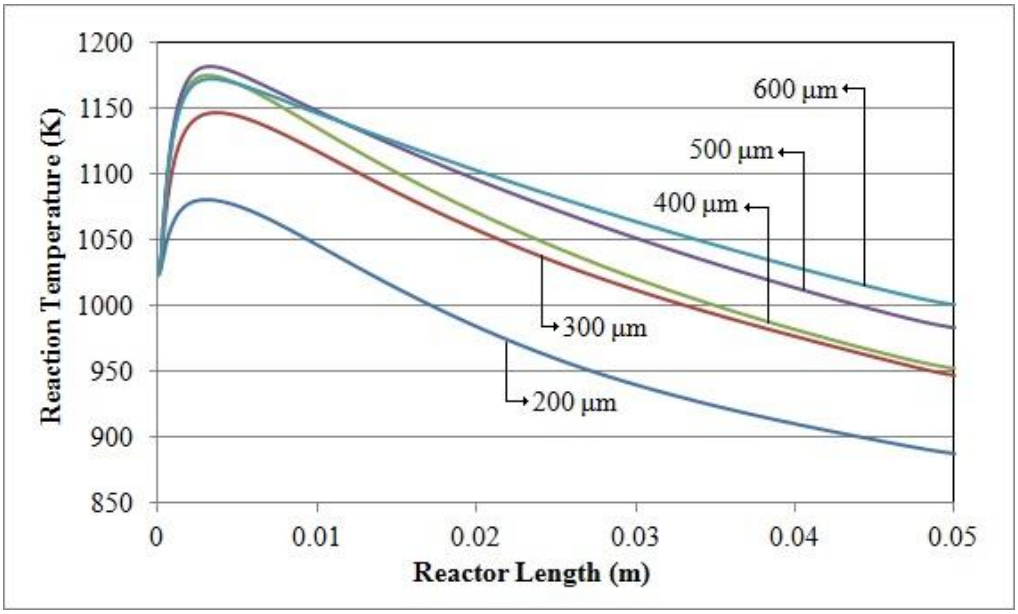

Figure 4.50. Effect of wall thickness on reaction channel temperature profile along the reactor.

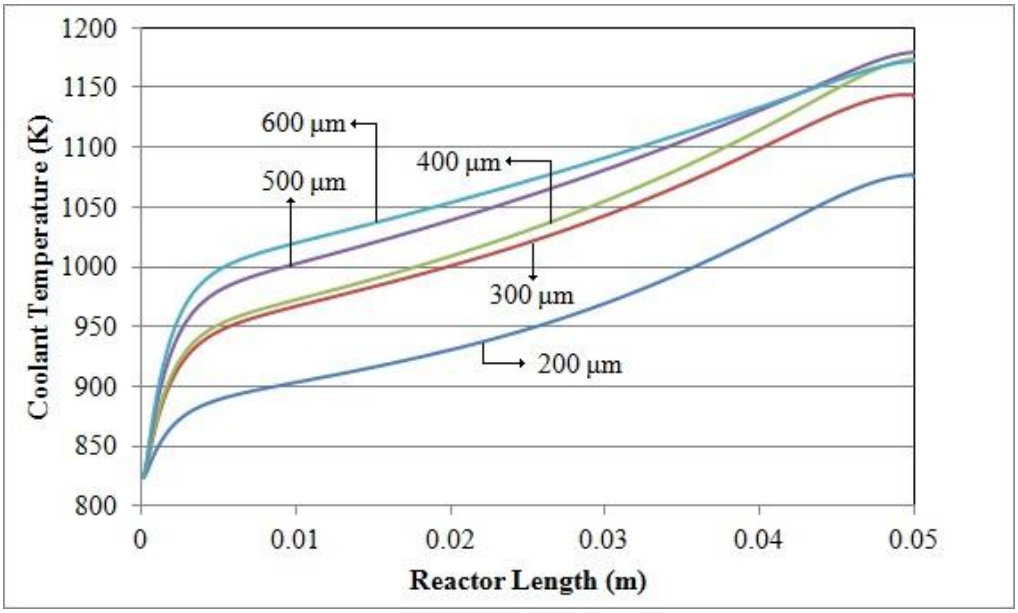

Figure 4.51. Effect of wall thickness on cooling channel temperature profile along the reactor.

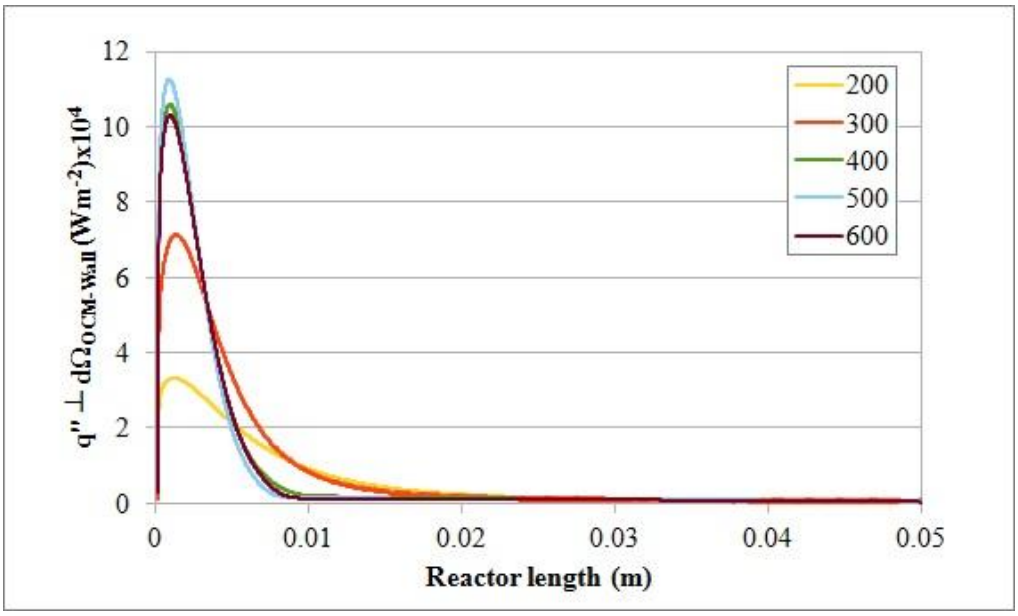

Figure 4.52. The normal component of the heat flux through the OCM washcoat-wall interface.

The effects of the wall thickness on the reaction and cooling channel temperature profiles are shown in Figure 4.50 and Figure 4.51, respectively. It is observed that outlet temperatures of the reaction channel increases as the wall thickness increases. The wall generates higher resistance between reaction and cooling channels as it gets thicker, which results in an increase in the outlet temperatures. However, the same trend is not valid for the maximum temperatures. Between wall thickness of 200 μm and 500 μm, maximum temperatures of the reaction channel increases with increasing wall thickness but when the thickness is increased to 600 μm, maximum temperature is lower than the one in 400 μm case.

This trend can be discussed by looking at heat flux through OCM washcoat and wall interface presented in Figure 4.52. At the entrance of the reaction channel, normal component of the heat flux is highest in 500 μm of wall thickness. 600 μm wall thickness does not enhance the heat transfer. When the wall thickness increases from 500 to 600 μm, the axial heat conduction becomes dominant distributing the heat along the reactor length better. As a result the maximum temperature is lower while the outlet temperature is higher in case of 600 μm wall thickness.

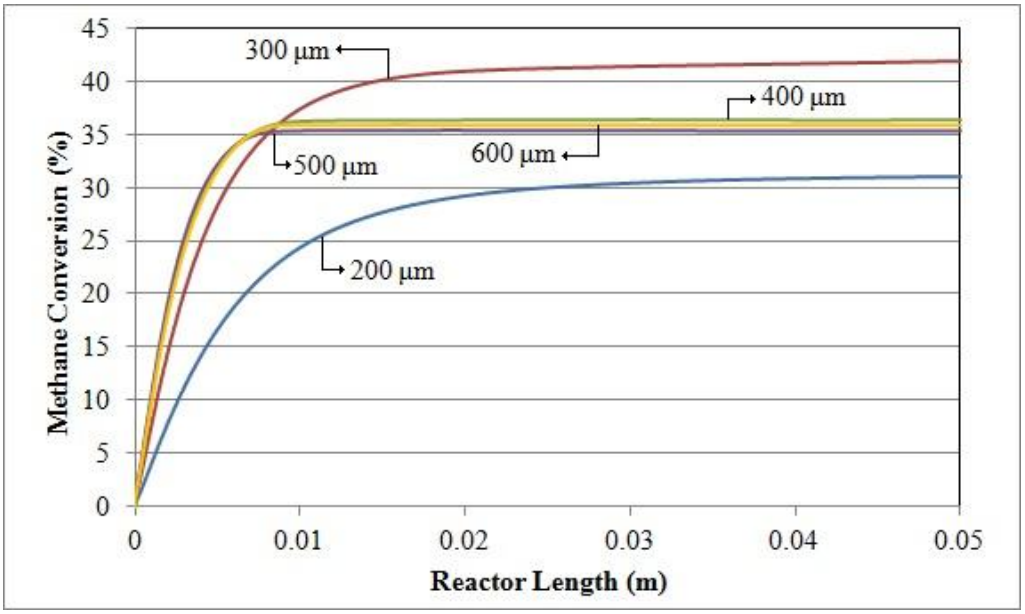

Figure 4.53. Effect of wall thickness on CH_4 conversion along the reactor.

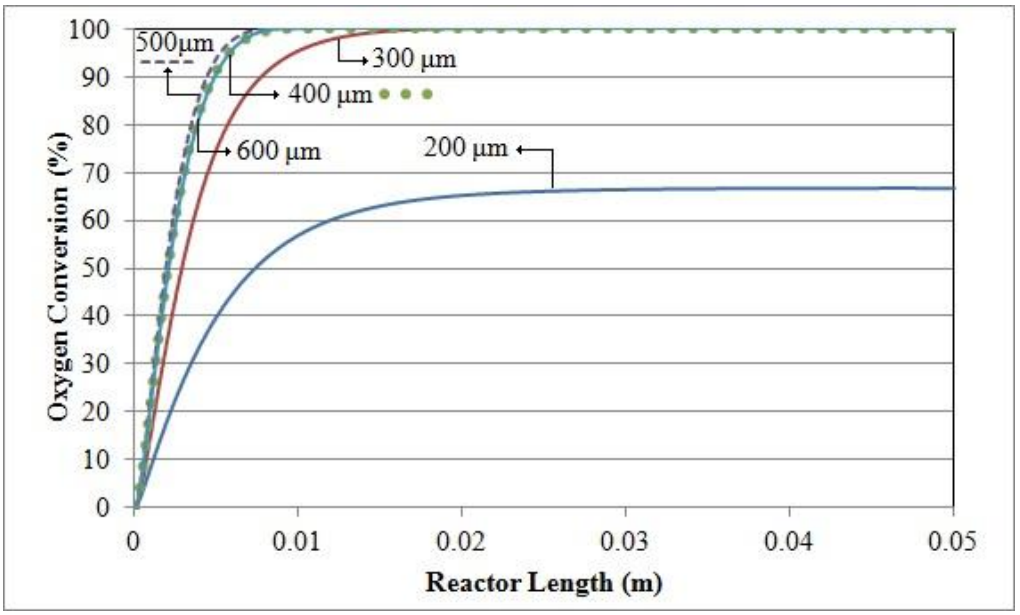

Figure 4.54. Effect of wall thickness on O_2 conversion along the reactor.

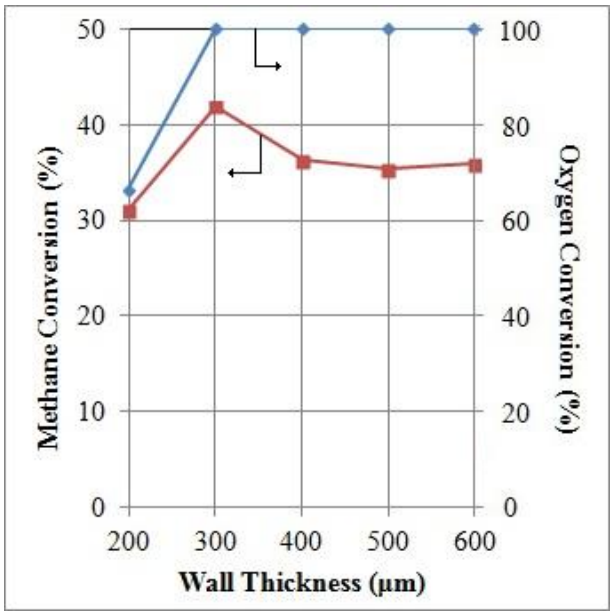

Figure 4.55. Effect of wall thickness on cooling CH_4 and O_2 conversion.

The effects of wall thickness on methane and oxygen conversions along the reactor length are presented in Figure 4.53 and Figure 4.54, respectively. Methane and oxygen conversions for cases with 400, 500 and 600 µm wall thicknesses are very close to each other. In the 200 µm case, cooling effect of steam on OCM is very high, so that reactions cannot proceed. The maximum methane conversion observed is 42% for 300 µm of wall thickness. This can be explained by looking at the heat flux trend for 300 µm wall in Figure 4.52. While other heat flux values drop immediately, the heat flux of 300 µm case is higher than other cases along the reactor which increases the conversion.

Ethylene selectivity and yield results along the reactor length which are shown in Figure 4.56 and Figure 4.57, respectively, support the previous observations about temperature profiles and conversion. Ethylene selectivity and yield have highest values of 23.5% and 9.9%, respectively for 300 µm of wall thickness case. Further increase in wall thickness decreases the cooling effect of steam on OCM reaction until 600 µm case. As explained earlier in this section, in 600 µm, the axial conduction becomes dominant which distributes the exothermal heat along the reactor better which causes a slight increase in selectivity and yield values after 500 µm case. At elevated temperatures the oxidation of all C_2 hydrocarbons is enhanced, which results in lower ethylene yield and selectivity.

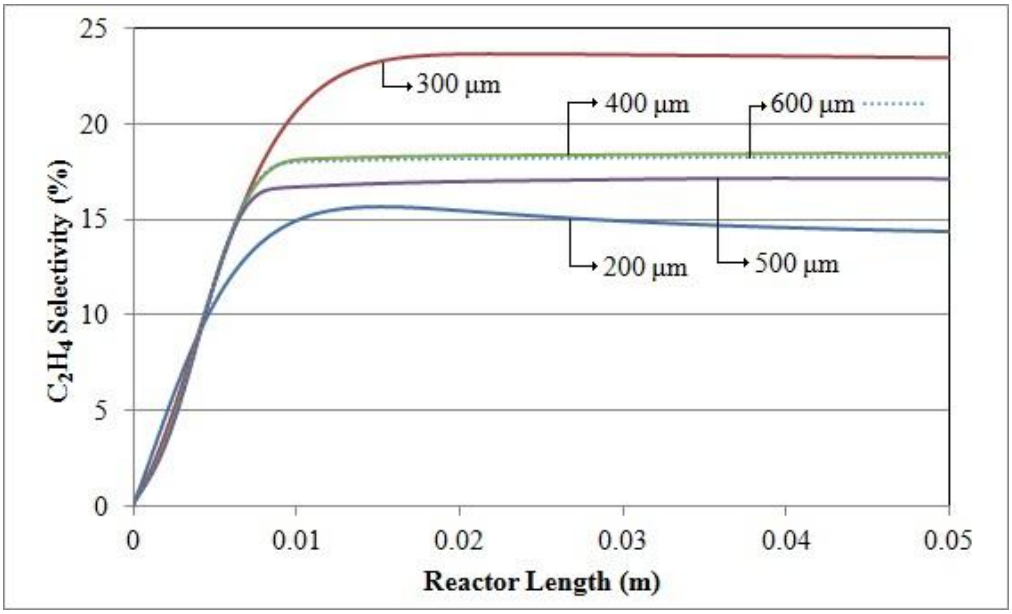

Figure 4.56. Effect of wall thickness on C_2H_4 selectivity along the reactor.

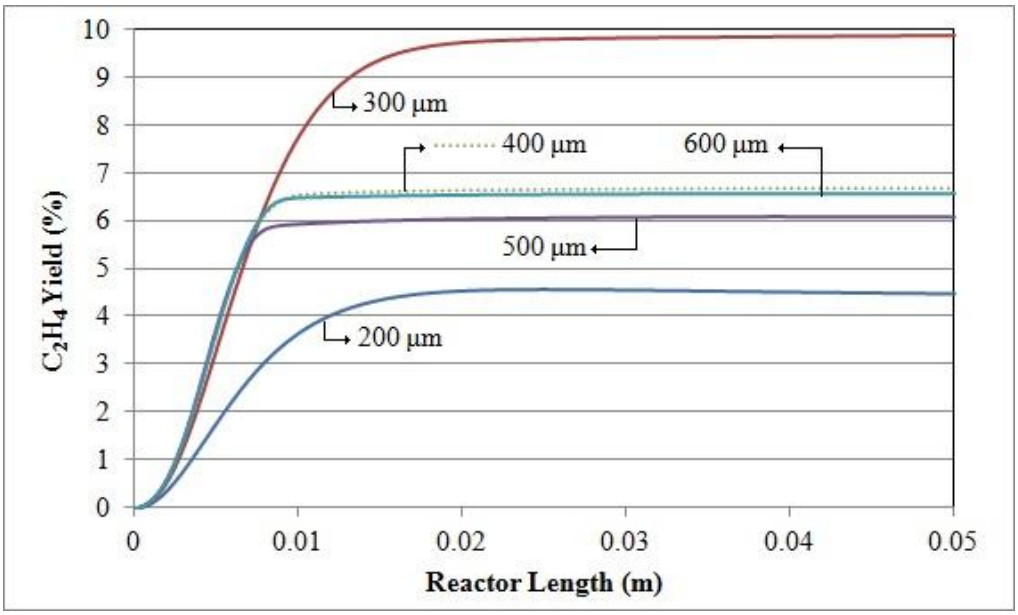

Figure 4.57. Effect of wall thickness on C_2H_4 yield along the reactor.

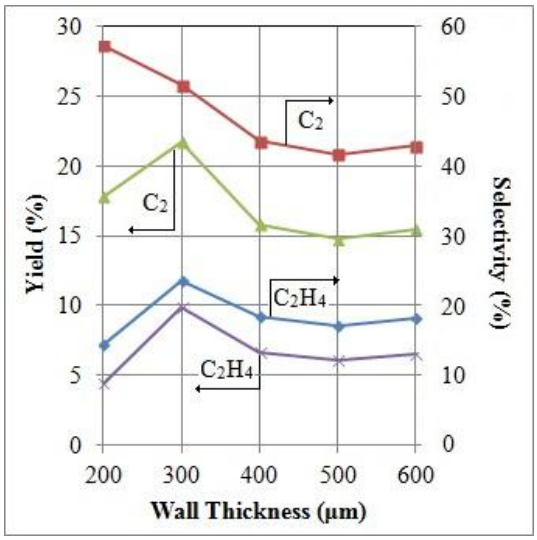

Figure 4.58. Effect of wall thickness on C_2H_4 and C_2 yields and selectivities.

The optimum wall thickness in case of reaction performance is found to be 300 µm, which favors highest methane conversion and highest C_2 and ethylene yield values as seen in Figure 4.58. When the wall thickness is 200 µm, oxygen can only reach 67% conversion due to over cooling of the reaction channel. However, the C_2 selectivity is highest due to the same reason with the reaction channel mass flow rate case: in the 200 µm wall case, main portion of the converted oxygen is used to produce ethane, limiting the ethylene production.

5. CONCLUSIONS AND RECOMMENDATIONS

5.1. Conclusions

The objectives of this study are to understand the effects of mechanical and operational conditions on OCM reaction in a microchannel reactor through a parametric study and to gain insight about the possibility of improving the reaction performance by controlling the temperature profile. The conclusions drawn from this study can be listed as follows:

- Changing the molar feed ratio of methane-to-oxygen directly influences the behavior of the reactions in OCM mechanism. As the feed ratio increases, the average reaction temperature decreases immediately due to lower release of exothermal heat. Conversion on reactants decreases, resulting in lower C_2 hydrocarbon yield.

- Reaction channel inlet temperature does not affect the temperature profile dramatically, but it is found to have an optimum value of 1023 K in terms of maximum ethylene selectivity and yield.

- Cooling channel inlet temperature has more significant effect on the reaction temperature profile when compared to reaction channel inlet temperature. Coolant inlet temperature has an optimum value of 823 K that leads to a C_2 hydrocarbon yield of 22.8%.

- The mass flow rate of the reaction channel has a significant effect on reaction temperature. Increasing the reactant mass flow rate increases the average reaction temperature due to higher heat source of the reaction. However, elevated temperatures favor the oxidation of C_2 hydrocarbons into carbon oxides.

- The cooling channel mass flow rate also affects the reaction performance significantly. Increasing the coolant mass flow rate magnify the cooling effect on the OCM reaction and regulate the temperature distribution of the reaction with an optimum value.

- The wall material has the most significant effect on the reaction temperature profile. Wall material with higher thermal conductivity has better ability to distribute the exothermal heat of OCM over the entire reactor. Flattening of the temperature profile, i.e. avoiding temperature peaks enhanced the reaction by increasing methane conversion while improving the C_2 hydrocarbon product yield at the same time, which is a challenging concept of study for OCM system.

- Thickness of the wall between the channels directly influences the temperature profile of the reaction channel. As the wall thickness increases, the average reaction temperature also increases due to reduced heat transfer through the separating wall. However above the thickness of 500 μm, axial conduction becomes dominant in the wall, which provides a better distribution of exothermal heat along the reactor.

5.2. Recommendations

The recommendations for enhancing this study for a possible future work are listed below:

- A different catalyst developed especially for microreactor applications which is more effective than lanthanum based catalysts can be used in order to improve the product selectivity.

- More comprehensive kinetics can be used in order to improve the mathematical model over a special catalyst developed for OCM reaction in microchannel reactor applications.

- Co-current or other flow modes for the fluids in the cooling and reaction channels can be applied.

- Wall materials suitable for high temperature applications with thermal conductivities higher than that of silicon carbide can be applied to see the improvement on temperature profile.

APPENDIX A: SIMULATION RESULTS IN DETAIL

Table A.1. Simulation results for feed ratio cases.

FEED RATIO (CH_4/O_2)		2	2.5	4	6	8	10
Wall material		Steel	Steel	Steel	Steel	Steel	Steel
Outlet pressure	Pa	101325	101325	101325	101325	101325	101325
OCM inlet temperature	K	1023	1023	1023	1023	1023	1023
OCM molar flow rate	ml min^{-1}	238	240	246	249	250	250
Coolant inlet temperature	K	823	823	823	823	823	823
Coolant molar flow rate	ml min^{-1}	80	80	80	80	80	80
Maximum temperature	K	1196	1146	1027	1023	1023	1023
OCM outlet temperature	K	959	946	902	888	881	877
Pressure drop	Pa	410	235	253	100	196	198
Conversion CH_4	%	43.0	42.0	19.6	11.0	7.3	5.5
Conversion O_2	%	100.0	99.9	60.3	51.7	45.9	43.8
Selectivity C_2	%	36.4	51.6	57.1	53.9	54.4	53.9
Yield C_2	%	15.6	21.6	11.2	5.9	3.9	3.0
Selectivity C_2H_4	%	16.1	23.5	8.3	3.9	2.7	1.9
Yield C_2H_4	%	7.1	9.9	1.6	0.4	0.2	0.1

Table A.2. Simulation results for reaction channel inlet temperature cases.

OCM Inlet Temperature (K)		973	1023	1073	1123	1173	1223
Wall material		Steel	Steel	Steel	Steel	Steel	Steel
Outlet pressure	Pa	101325	101325	101325	101325	101325	101325
OCM inlet temperature	K	973	1023	1073	1123	1173	1223
OCM molar flow rate	ml min^{-1}	240	240	240	240	240	240
Coolant inlet temperature	K	823	823	823	823	823	823
Coolant molar flow rate	ml min^{-1}	80	80	80	80	80	80
Maximum temperature	K	1084	1146	1160	1193	1188	1223
OCM outlet temperature	K	928	946	950	959	960	964
Pressure drop	Pa	329	235	279.8	300	193	520
Conversion CH_4	%	41.5	42	41.6	37.4	39.2	41.3
Conversion O_2	%	83.3	100	100	100	100	100
Selectivity C_2	%	58	51.6	48.9	42.7	44.1	49.7
Yield C_2	%	24.6	21.6	20.3	15.9	17.3	20.5
Selectivity C_2H_4	%	19.2	23.5	21.4	18.2	19	20.2
Yield C_2H_4	%	7.9	9.9	8.9	6.8	7.4	8.3

Table A.3. Simulation results for cooling channel inlet temperature cases.

Steam Inlet Temperature (K)		773	798	823	848	873
Wall material		Steel	Steel	Steel	Steel	Steel
Outlet pressure	Pa	101325	101325	101325	101325	101325
OCM inlet temperature	K	1023	1023	1023	1023	1023
OCM molar flow rate	ml min^{-1}	240	240	240	240	240
Coolant inlet temperature	K	773	798	823	848	873
Coolant molar flow rate	ml min^{-1}	80	80	80	80	80
Maximum temperature	K	1060	1092	1146	1159	1161
OCM outlet temperature	K	883	911	946	967	986
Pressure drop	Pa	344.4	166	235	239	239
Conversion CH_4	%	30.2	39.5	41.2	39.94	39.4
Conversion O_2	%	62	81	100	100	100
Selectivity C_2	%	54.9	57.7	51.6	47.8	46.8
Yield C_2	%	16.6	22.8	21.6	19.1	18.4
Selectivity C_2H_4	%	12.6	18.4	23.5	21.9	21.5
Yield C_2H_4	%	3.8	7.29	9.9	8.76	8.5

Table A.4. Simulation results for reaction channel mass flow rate cases.

OCM Mass Flow Rate ($kg\ s^{-1}$)x 10^6		3	3.5	5	6
Wall material		Steel	Steel	Steel	Steel
Outlet pressure	Pa	101325	101325	101325	101325
OCM inlet temperature	K	1023	1023	1023	1023
OCM molar flow rate	$ml\ min^{-1}$	207	240	345	414
Coolant inlet temperature	K	823	823	823	823
Coolant molar flow rate	$ml\ min^{-1}$	80	80	80	80
Maximum temperature	K	1065	1146	1228	1272
OCM outlet temperature	K	914	946	985	1027
Pressure drop	Pa	347	235	543	663
Conversion CH_4	%	36.4	42	34.2	33
Conversion O_2	%	72.6	99.9	100	100
Selectivity C_2	%	58.1	51.6	34.2	28.7
Yield C_2	%	21.1	21.6	11.7	9.5
Selectivity C_2H_4	%	15	23.5	12.39	9.9
Yield C_2H_4	%	5.5	9.9	4.3	3.3

Table A.5. Simulation results for cooling channel mass flow rate cases.

Steam Mass Flow Rate ($kg\ s^{-1}$) x 10^6		0.5	0.7	1	1.5
Wall material		Steel	Steel	Steel	Steel
Outlet pressure	Pa	101325	101325	101325	101325
OCM inlet temperature	K	1023	1023	1023	1023
OCM molar flow rate	$ml\ min^{-1}$	240	240	240	240
Coolant inlet temperature	K	823	823	823	823
Coolant molar flow rate	$ml\ min^{-1}$	40	60	80	120
Maximum temperature	K	1170	1164	1146	1055
OCM outlet temperature	K	989	974	946	887
Pressure drop	Pa	254	334	235	197
Conversion CH_4	%	38.9	38.8	42	28.7
Conversion O_2	%	100	100	100	59.1
Selectivity C_2	%	45.3	47.4	51.6	54.8
Yield C_2	%	17.6	18.4	21.6	15.7
Selectivity C_2H_4	%	20.2	21.7	23.5	11.9
Yield C_2H_4	%	7.8	8.4	9.9	3.4

Table A.6. Simulation results for wall material cases.

Wall material		Steel	Alumina	SiC
Outlet pressure	Pa	101325	101325	101325
OCM inlet temperature	K	1023	1023	1023
OCM molar flow rate	ml min^{-1}	240	240	240
Coolant inlet temperature	K	823	823	823
Coolant molar flow rate	ml min^{-1}	80	80	80
Maximum temperature	K	1146	1160	1095
OCM outlet temperature	K	946	900	976
Pressure drop	Pa	235	415.5	188
Conversion CH_4	%	42	41.9	46.8
Conversion O_2	%	99.9	100	94
Selectivity C_2	%	51.6	50.1	60.8
Yield C_2	%	21.6	21	28.5
Selectivity C_2H_4	%	23.5	20.6	23.9
Yield C_2H_4	%	9.9	8.6	11.2

Table A.7. Simulation results for wall thickness cases.

Wall thickness (μm)		200	300	400	500	600
Wall material		Steel	Steel	Steel	Steel	Steel
Outlet pressure	Pa	101325	101325	101325	101325	101325
OCM inlet temperature	K	1023	1023	1023	1023	1023
OCM molar flow rate	ml min^{-1}	240	240	240	240	240
Coolant inlet temperature	K	823	823	823	823	823
Coolant molar flow rate	ml min^{-1}	80	80	80	80	80
Maximum temperature	K	1247	1146	1167.6	1180	1172
OCM outlet temperature	K	921	945	958	982	997
Pressure drop	Pa	199	235	208	188	192
Conversion CH_4	%	32.2	43	37.4	35.3	35.8
Conversion O_2	%	100	99.9	100	100	100
Selectivity C_2	%	57.2	51.6	43.5	41.6	42.9
Yield C_2	%	17.7	21.6	15.8	14.7	15.4
Selectivity C_2H_4	%	14.4	23.5	18.4	17.1	18.2
Yield C_2H_4	%	4.5	9.9	6.7	5.9	6.5

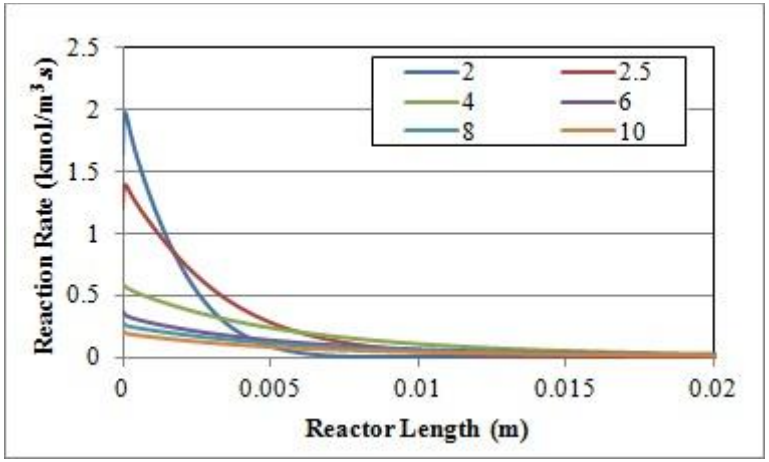

Figure A.1. Feed ratio comparison – Reaction rate of R1.

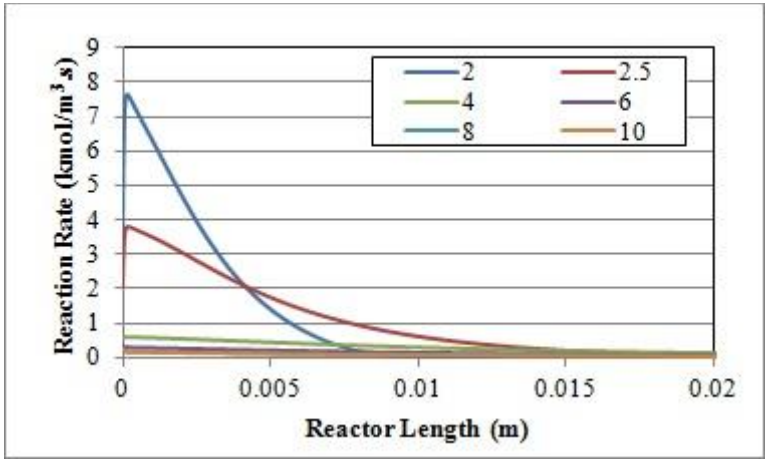

Figure A.2. Feed ratio comparison – Reaction rate of R2.

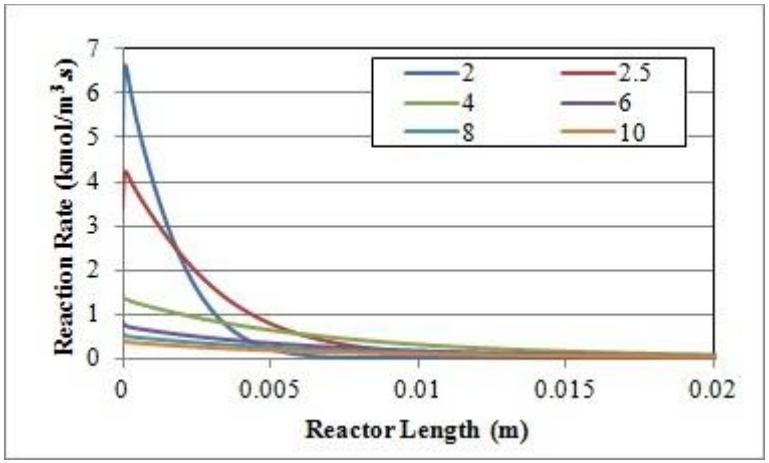

Figure A.3. Feed ratio comparison – Reaction rate of R3.

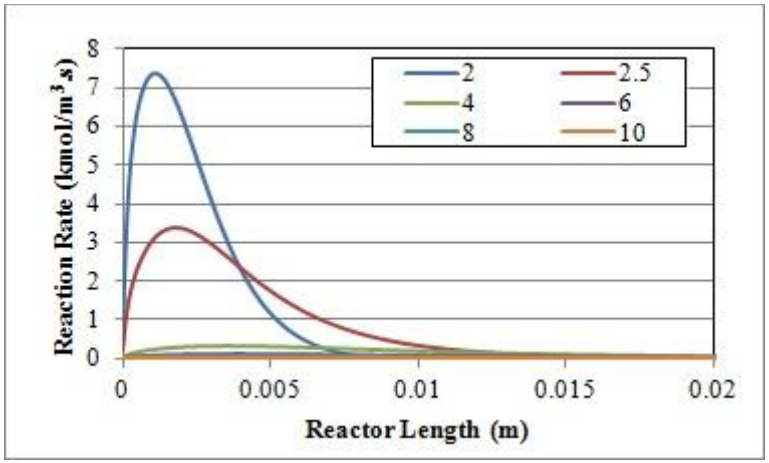

Figure A.4. Feed ratio comparison – Reaction rate of R4.

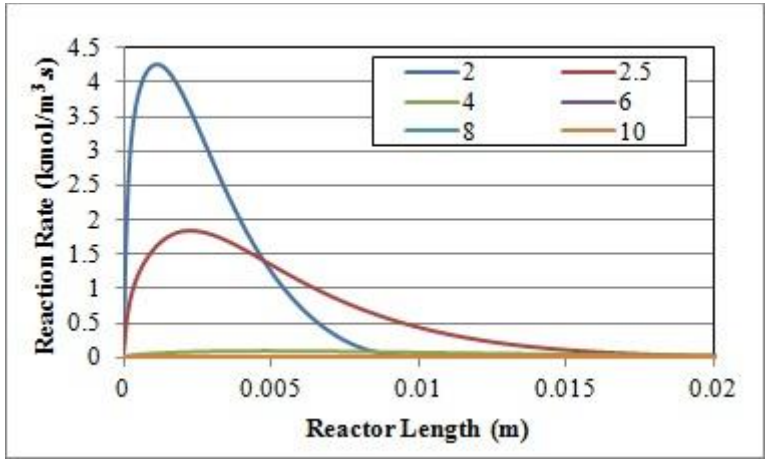

Figure A.5. Feed ratio comparison – Reaction rate of R5.

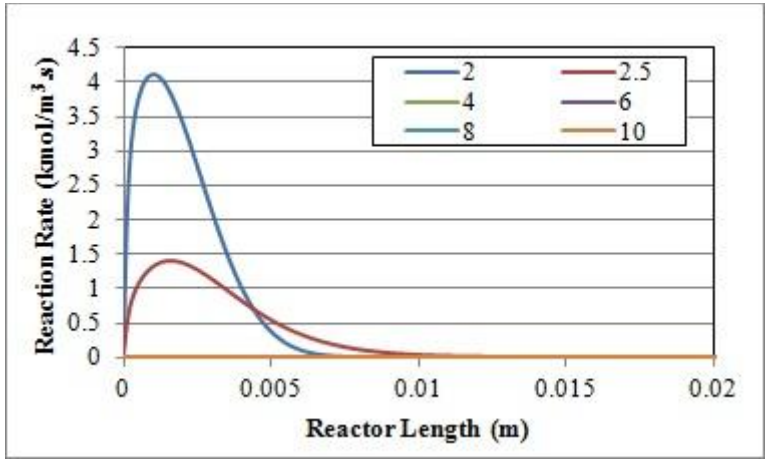

Figure A.6. Feed ratio comparison – Reaction rate of R6.

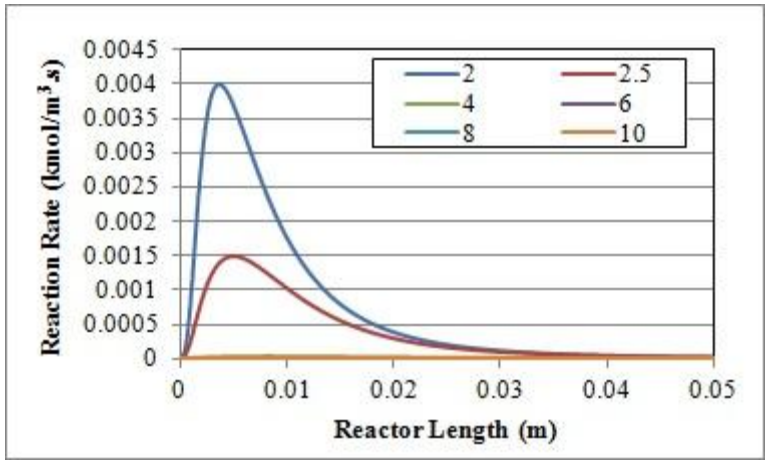

Figure A.7. Feed ratio comparison – Reaction rate of R7.

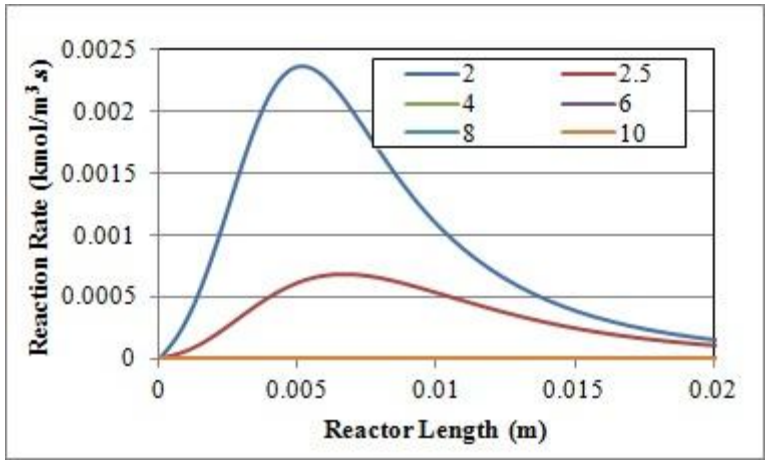

Figure A.8. Feed ratio comparison – Reaction rate of R8.

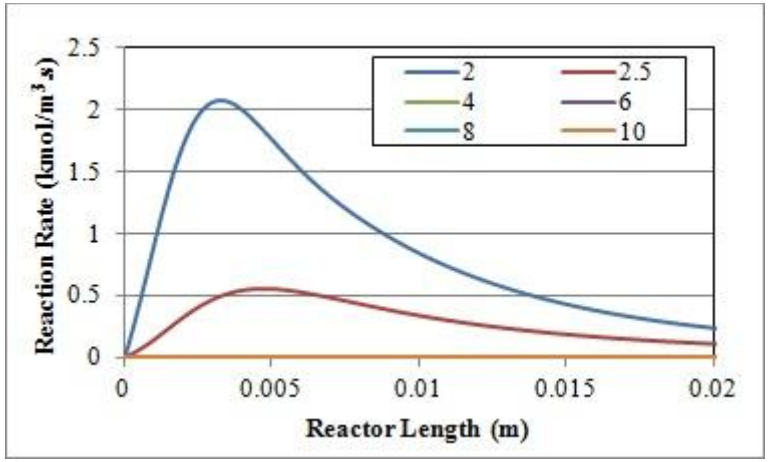

Figure A.9. Feed ratio comparison – Reaction rate of R9.

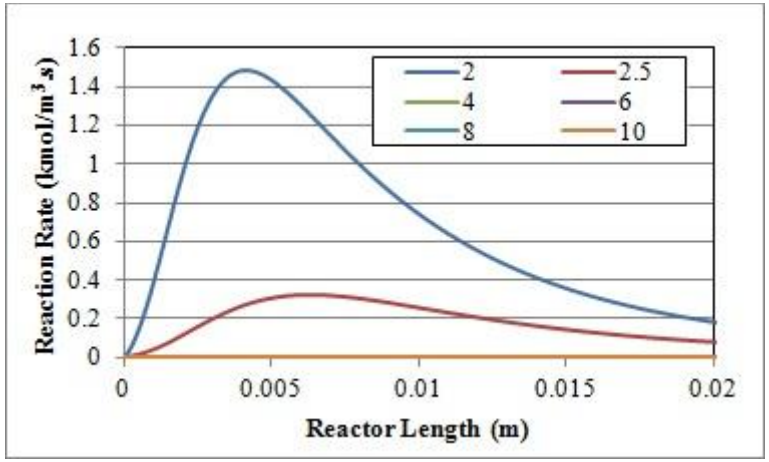

Figure A.10. Feed ratio comparison – Reaction rate of R10.

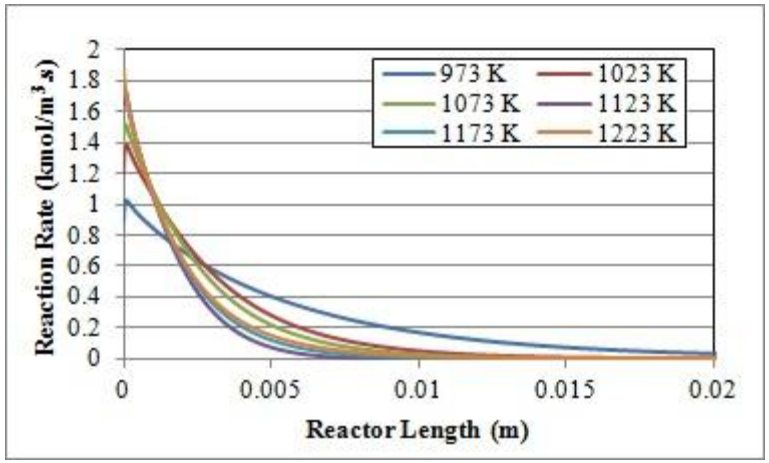

Figure A.11. OCM inlet temperature cases – Reaction rate of R1.

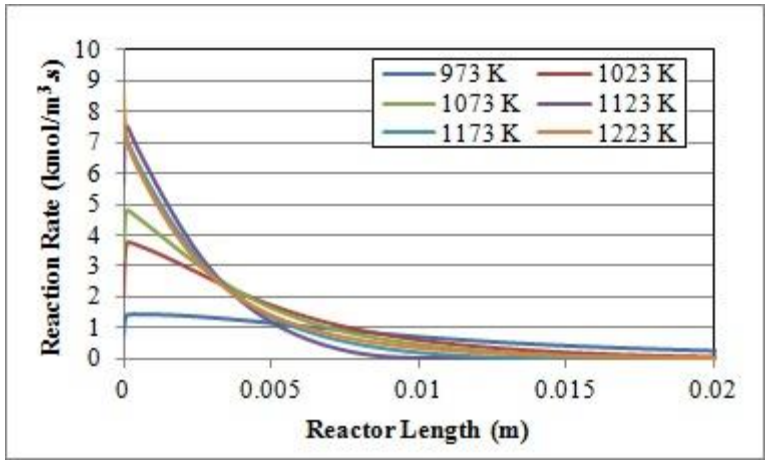

Figure A.12. OCM inlet temperature cases – Reaction rate of R2.

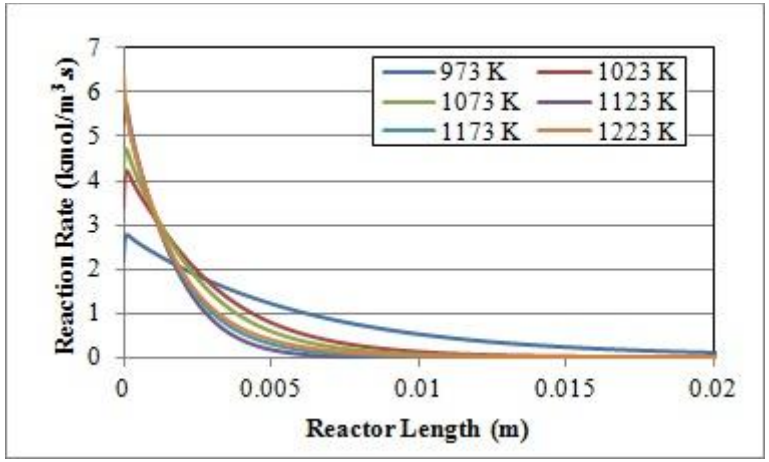

Figure A.13. OCM inlet temperature cases – Reaction rate of R3.

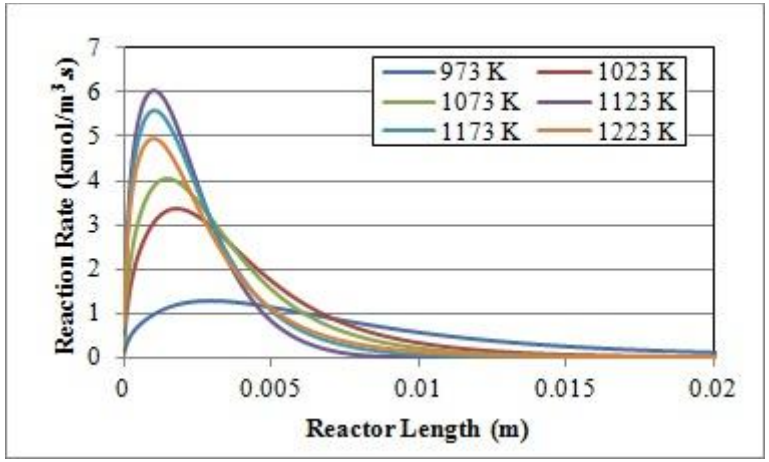

Figure A.14. OCM inlet temperature cases – Reaction rate of R4.

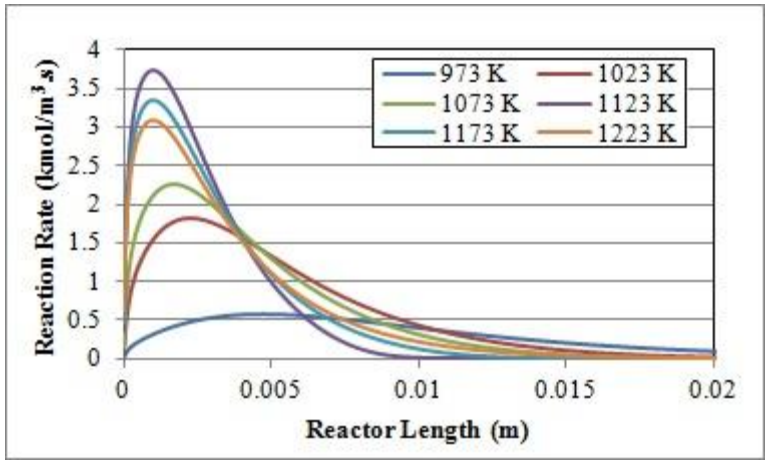

Figure A.15. OCM inlet temperature cases – Reaction rate of R5.

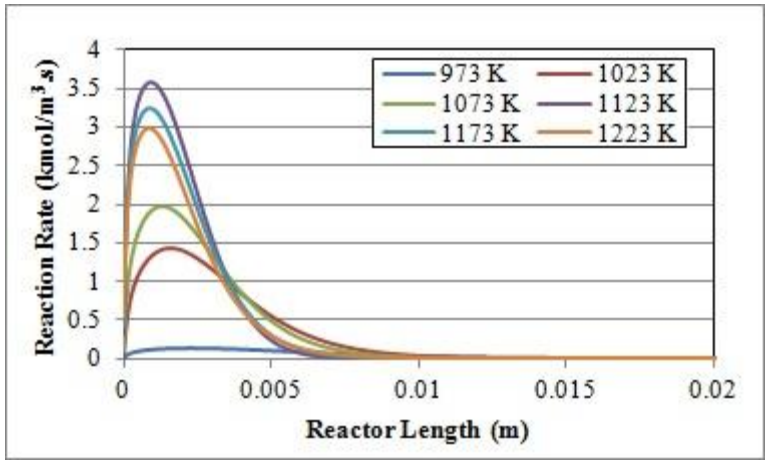

Figure A.16. OCM inlet temperature cases – Reaction rate of R6.

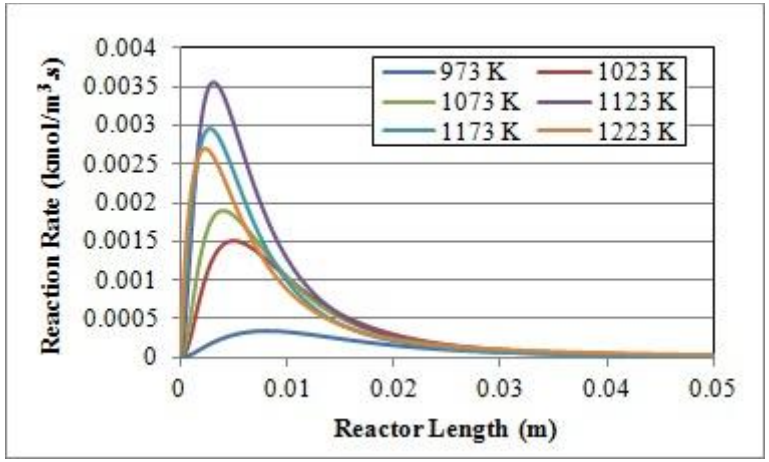

Figure A.17. OCM inlet temperature cases – Reaction rate of R7.

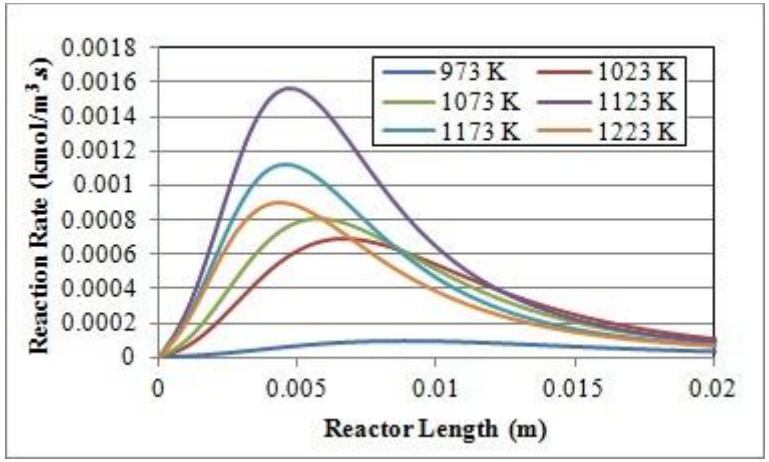

Figure A.18. OCM inlet temperature cases – Reaction rate of R8.

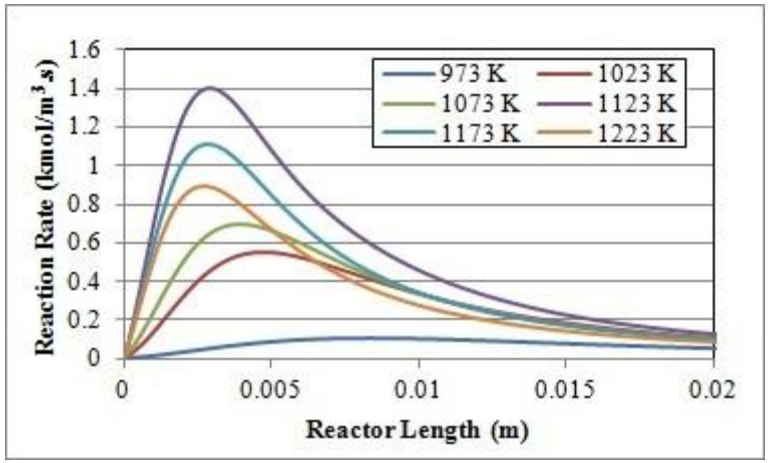

Figure A.19. OCM inlet temperature cases – Reaction rate of R9.

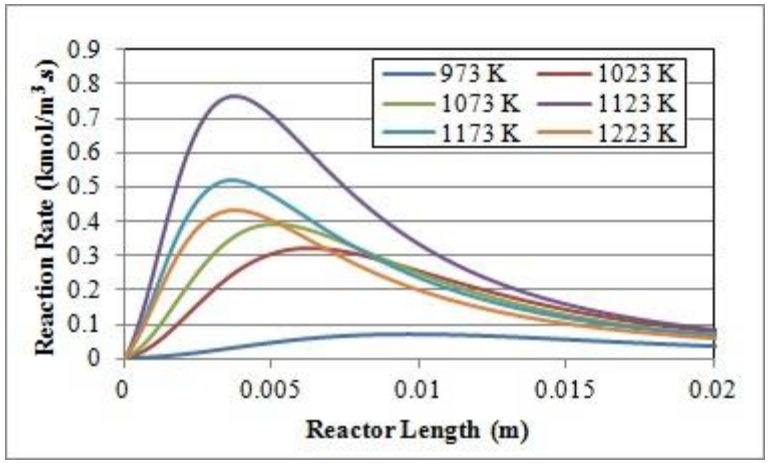

Figure A.20. OCM inlet temperature cases – Reaction rate of R10.

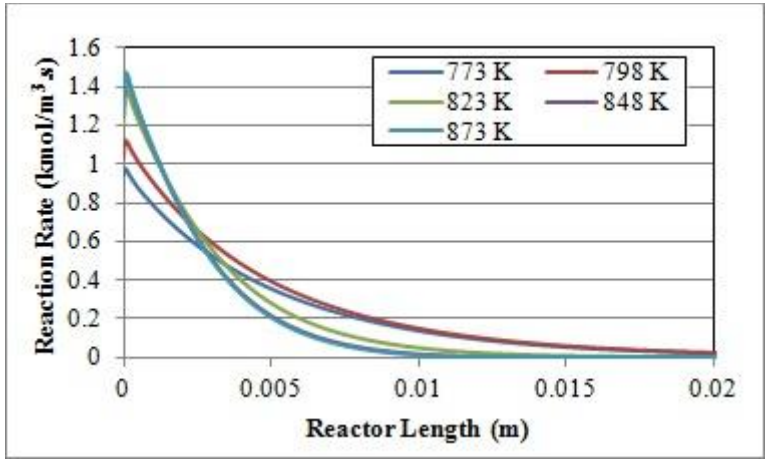

Figure A.21. Steam inlet temperature comparison-Reaction rate of R1.

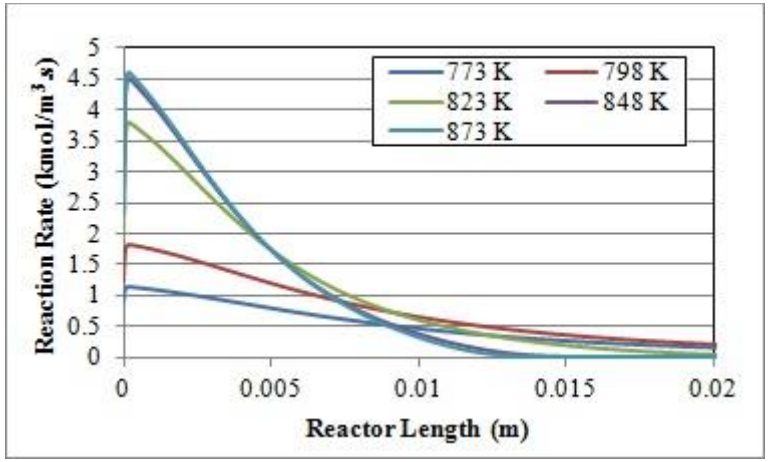

Figure A.22. Steam inlet temperature comparison–Reaction rate of R2.

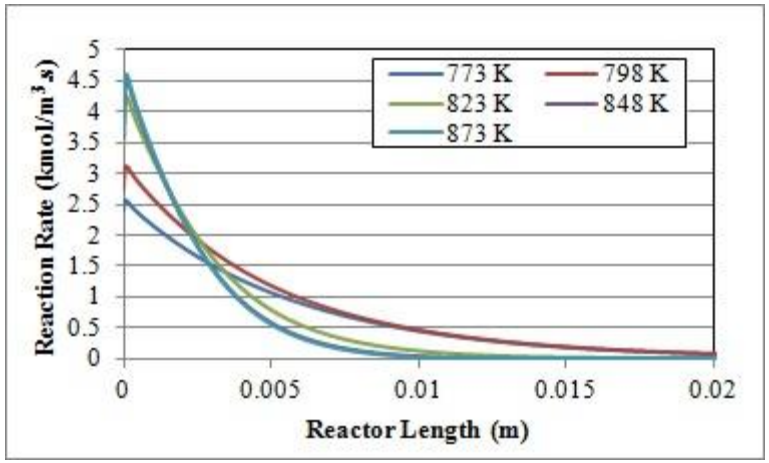

Figure A.23. Steam inlet temperature comparison–Reaction rate of R3.

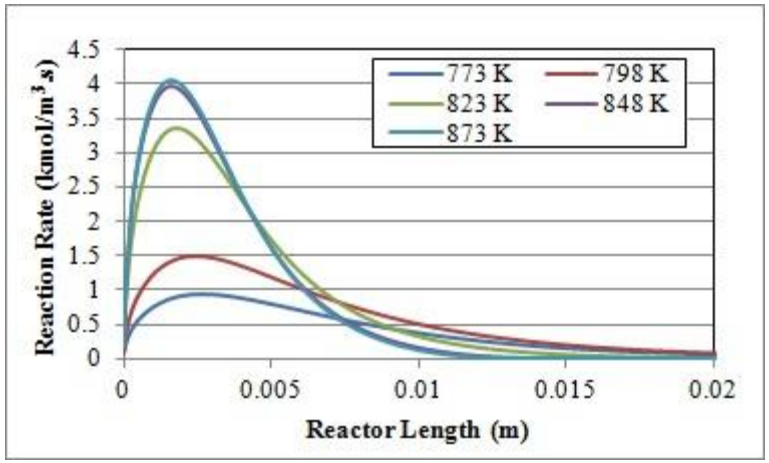

Figure A.24. Steam inlet temperature comparison–Reaction rate of R4.

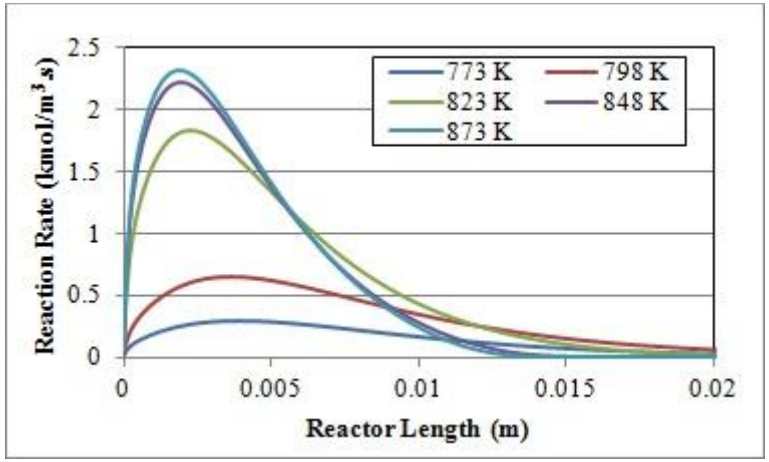

Figure A.25. Steam inlet temperature comparison–Reaction rate of R5.

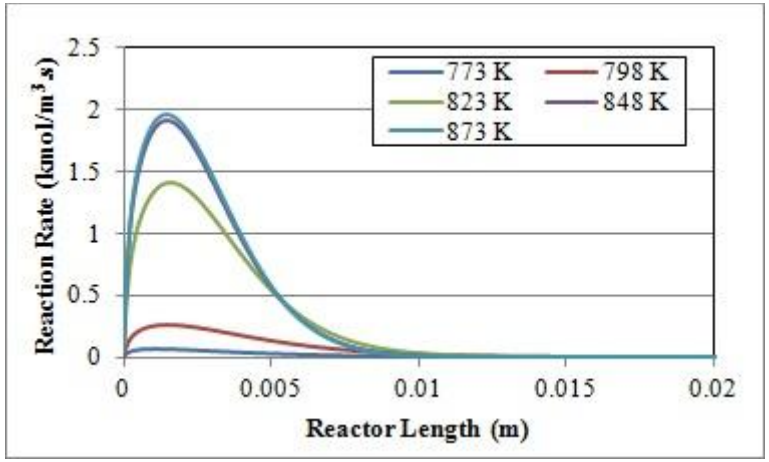

Figure A.26. Steam inlet temperature comparison–Reaction rate of R6.

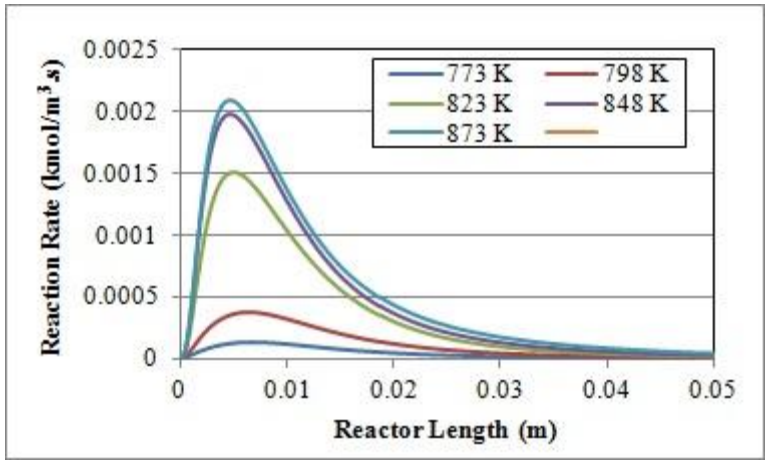

Figure A.27. Steam inlet temperature comparison–Reaction rate of R7.

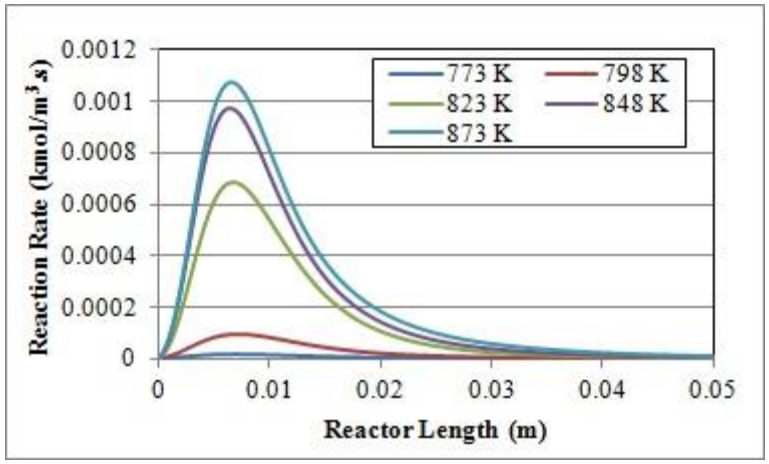

Figure A.28. Steam inlet temperature comparison–Reaction rate of R8.

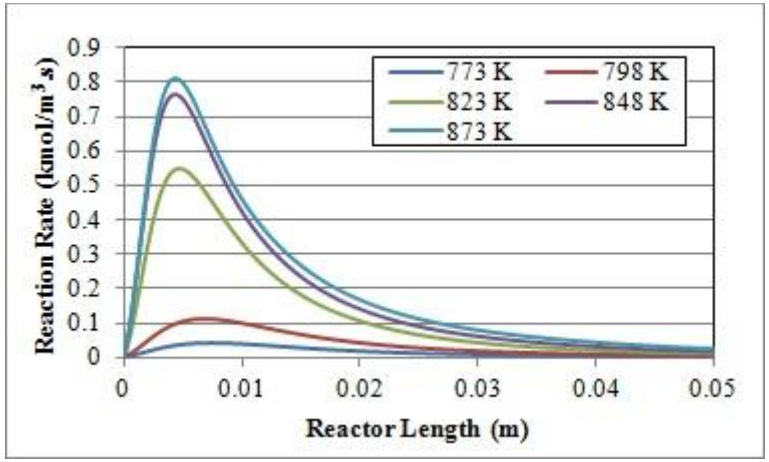

Figure A.29. Steam inlet temperature comparison–Reaction rate of R9.

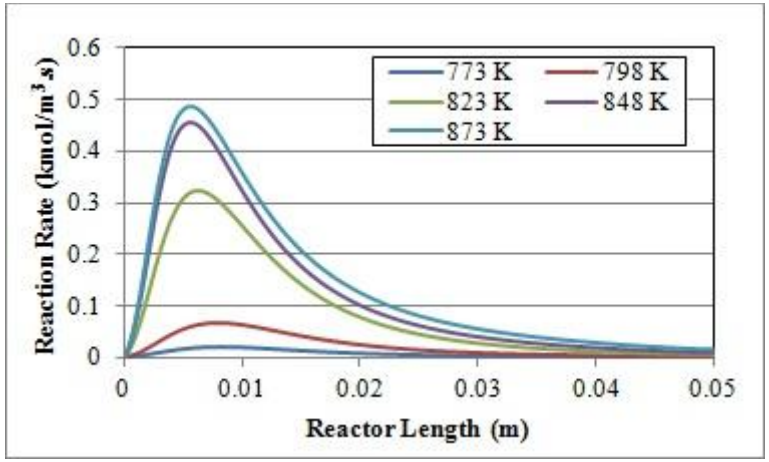

Figure A.30.Steam inlet temperature comparison-Reaction rate of R10.

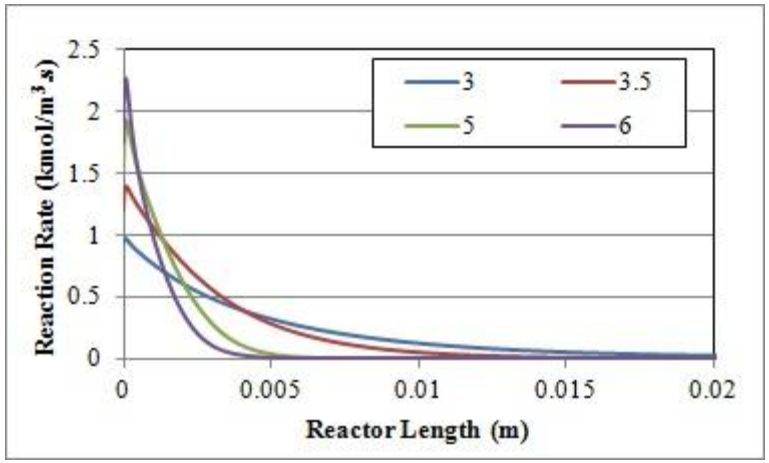

Figure A.31. OCM mass flow rate comparison – Reaction rate of R1.

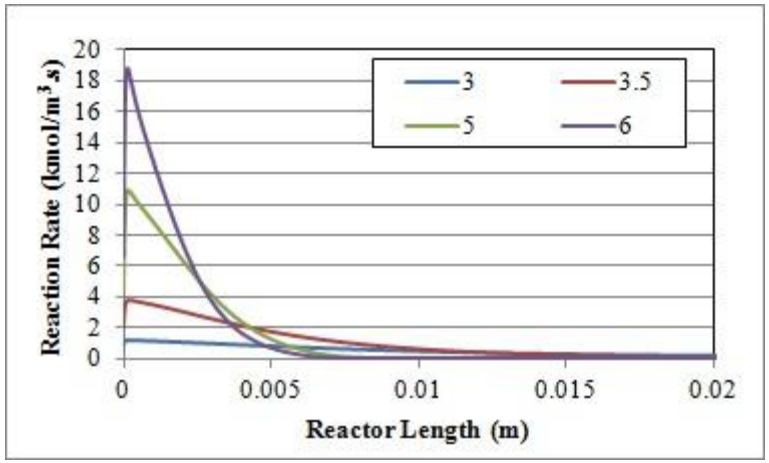

Figure A.32. OCM mass flow rate comparison – Reaction rate of R2.

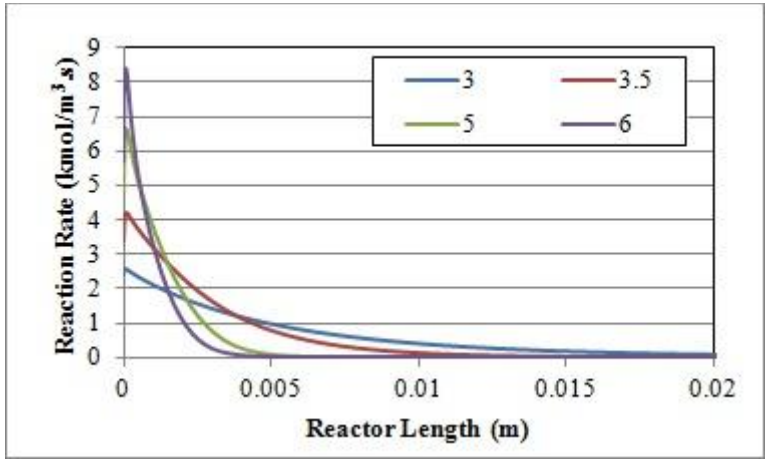

Figure A.33. OCM mass flow rate comparison – Reaction rate of R3.

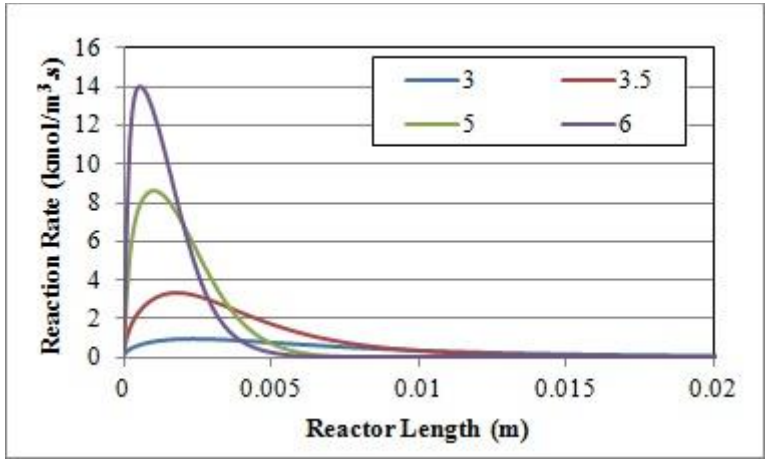

Figure A.34. OCM mass flow rate comparison – Reaction rate of R4.

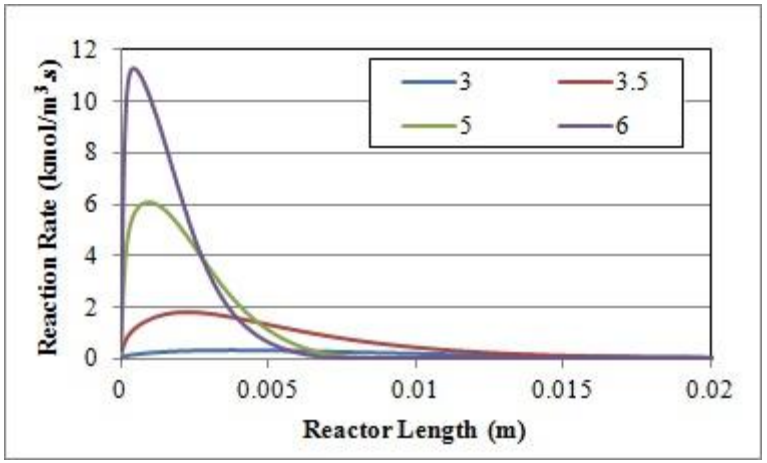

Figure A.35. OCM mass flow rate comparison – Reaction rate of R5.

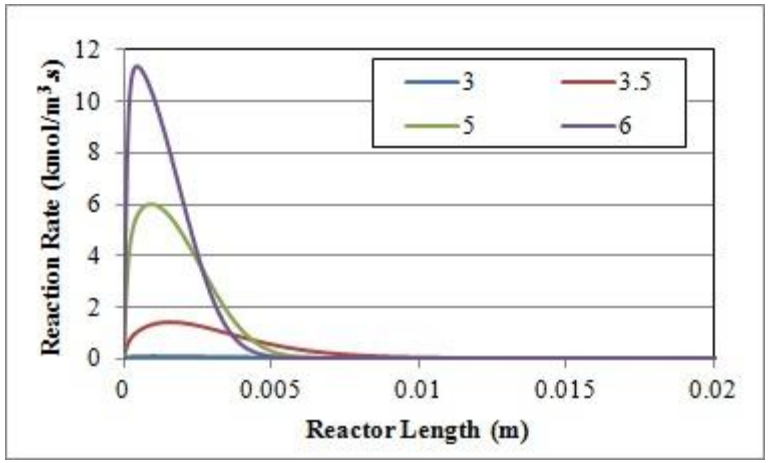

Figure A.36. OCM mass flow rate comparison – Reaction rate of R6.

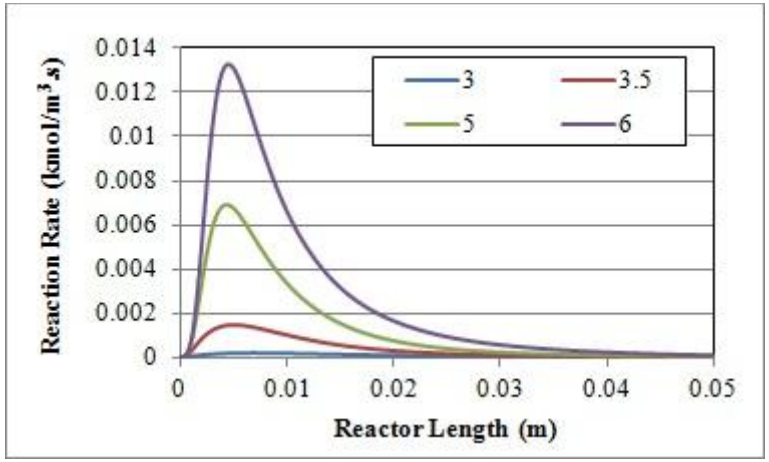

Figure A.37. OCM mass flow rate comparison – Reaction rate of R7.

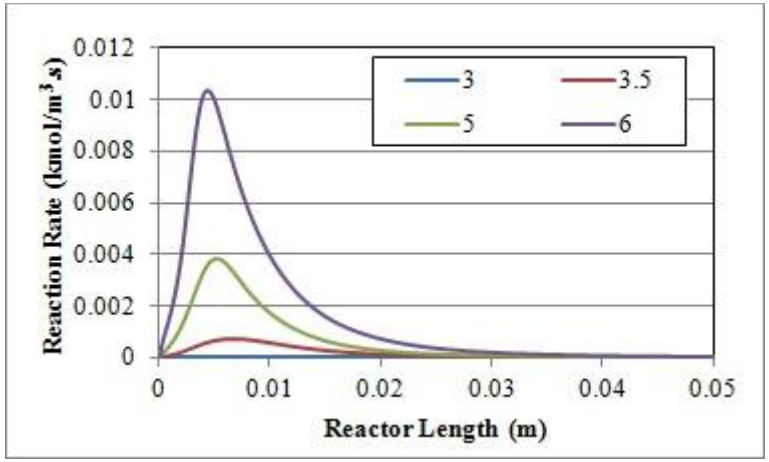

Figure A.38. OCM mass flow rate comparison – Reaction rate of R8.

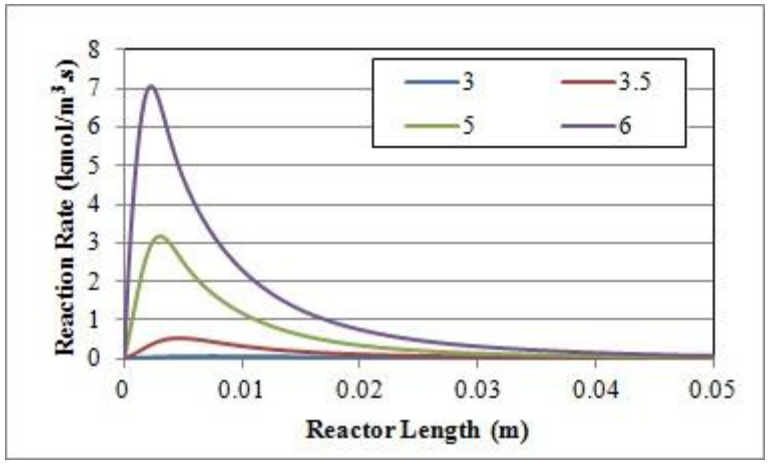

Figure A.39. OCM mass flow rate comparison – Reaction rate of R9.

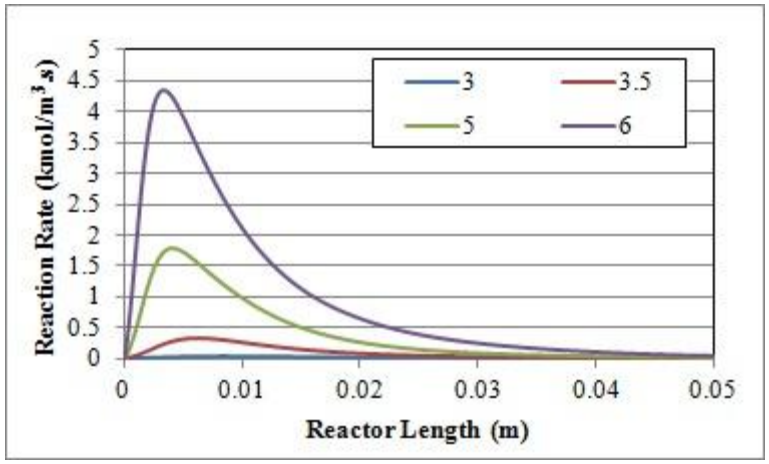

Figure A.40. OCM mass flow rate comparison – Reaction rate of R10.

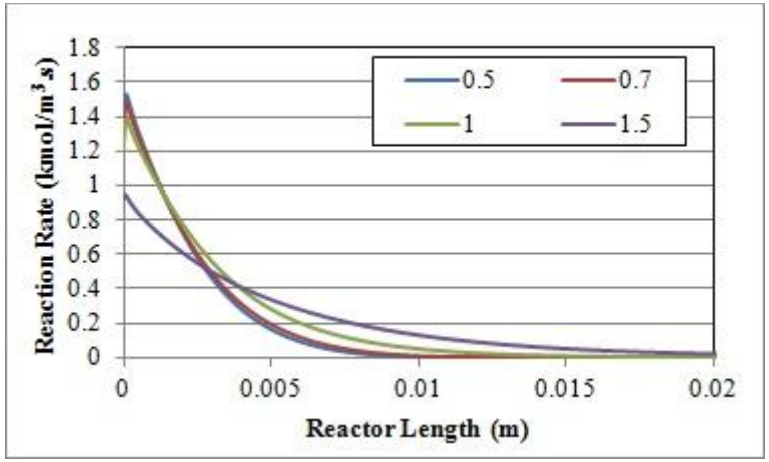

Figure A.41. Steam mass flow rate comparison – Reaction rate of R1.

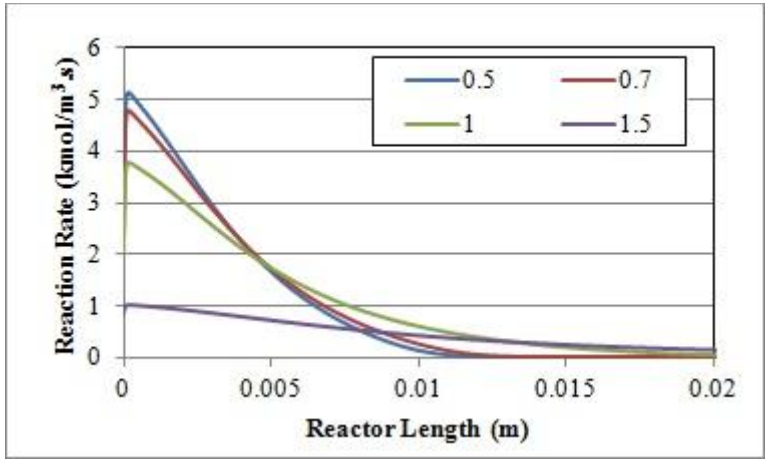

Figure A.42. Steam mass flow rate comparison – Reaction rate of R2.

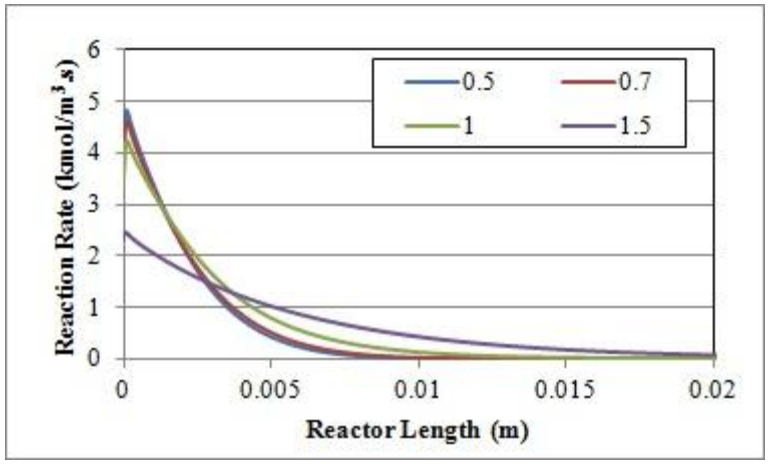

Figure A.43. Steam mass flow rate comparison – Reaction rate of R3.

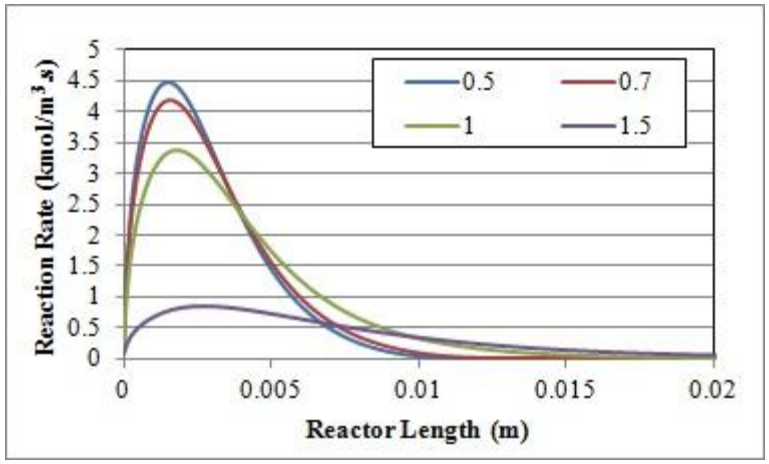

Figure A.44. Steam mass flow rate comparison – Reaction rate of R4.

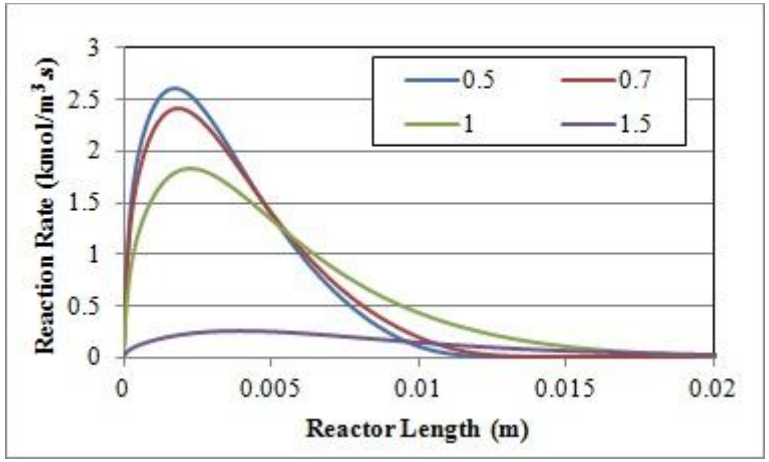

Figure A.45. Steam mass flow rate comparison – Reaction rate of R5.

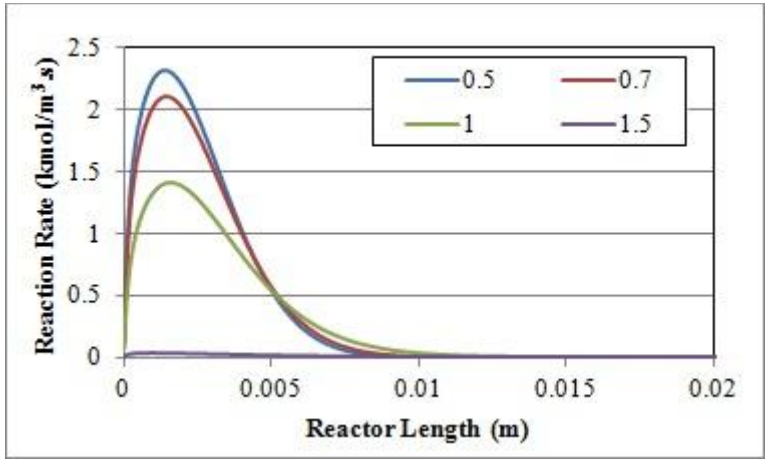

Figure A.46. Steam mass flow rate comparison – Reaction rate of R6.

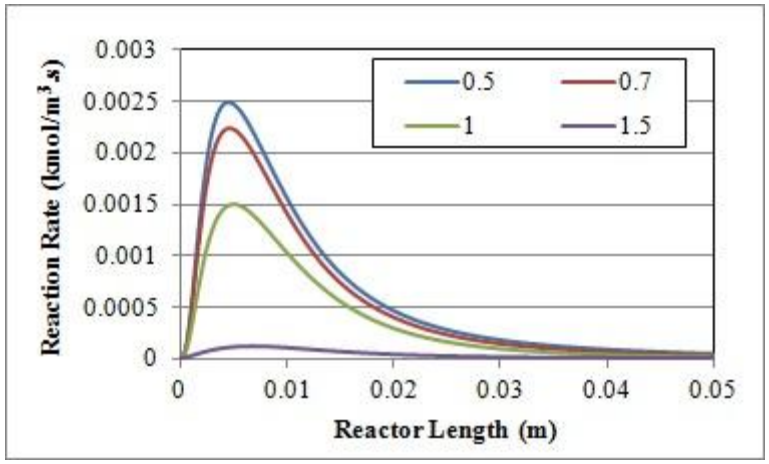

Figure A.47. Steam mass flow rate comparison – Reaction rate of R7.

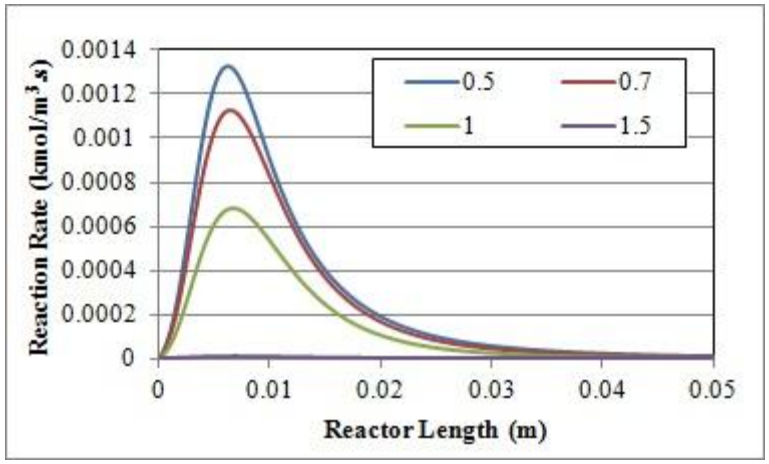

Figure A.48. Steam mass flow rate comparison – Reaction rate of R8.

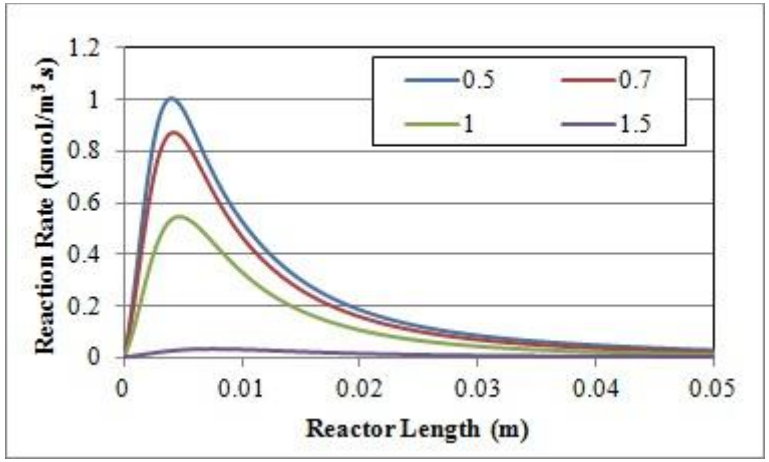

Figure A.49. Steam mass flow rate comparison – Reaction rate of R9.

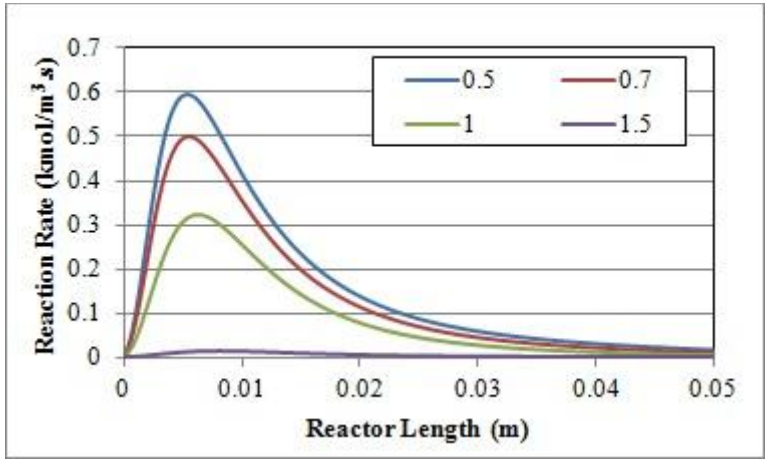

Figure A.50. Steam mass flow rate comparison – Reaction rate of R10.

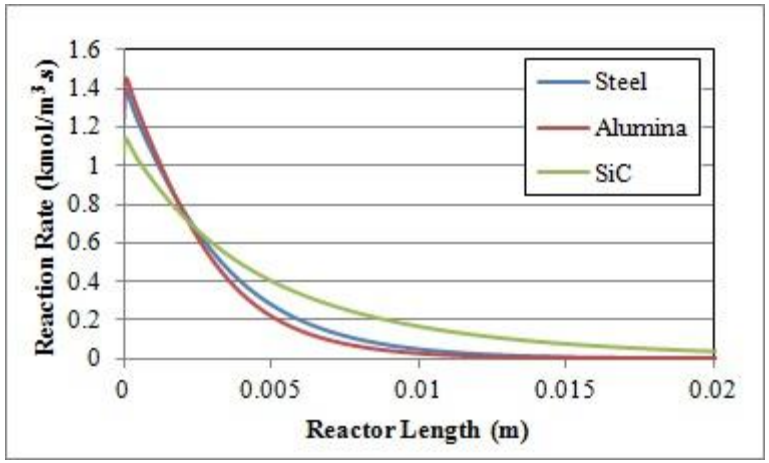

Figure A.51. Wall material comparison – Reaction rate of R1.

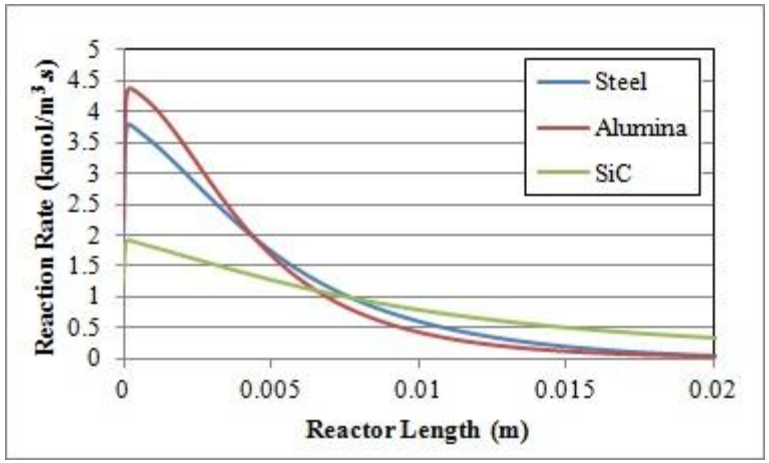

Figure A.52. Wall material comparison – Reaction rate of R2.

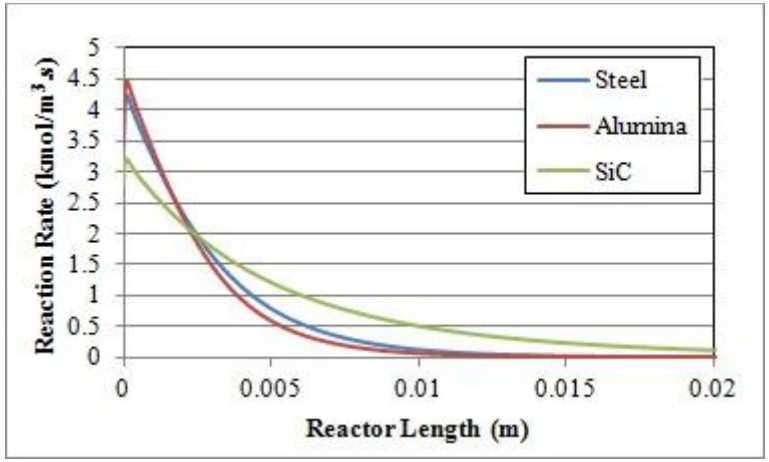

Figure A.53. Wall material comparison – Reaction rate of R3.

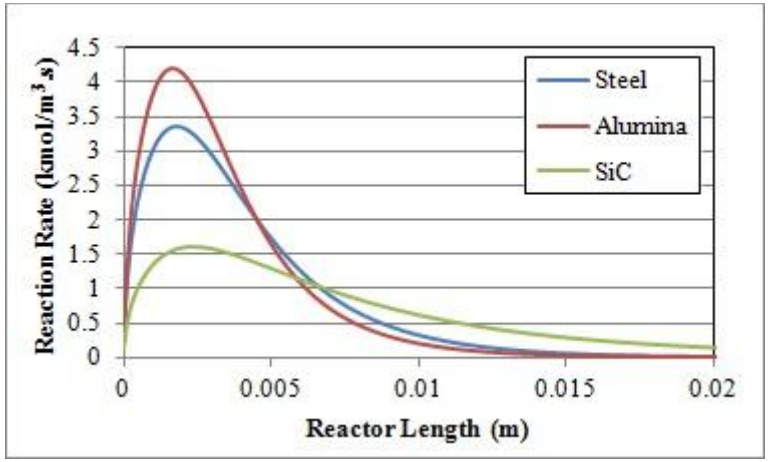

Figure A.54. Wall material comparison – Reaction rate of R4.

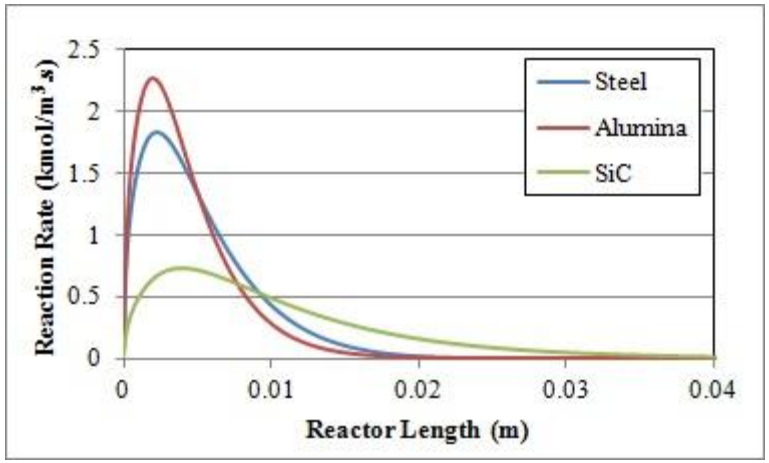

Figure A.55. Wall material comparison – Reaction rate of R5.

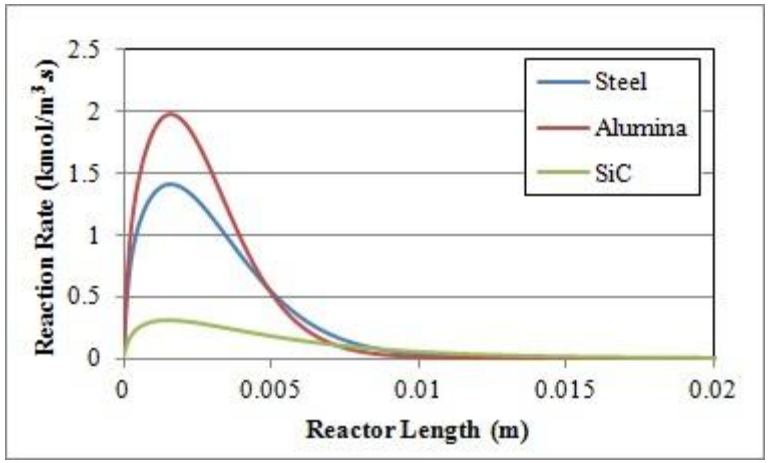

Figure A.56. Wall material comparison – Reaction rate of R6.

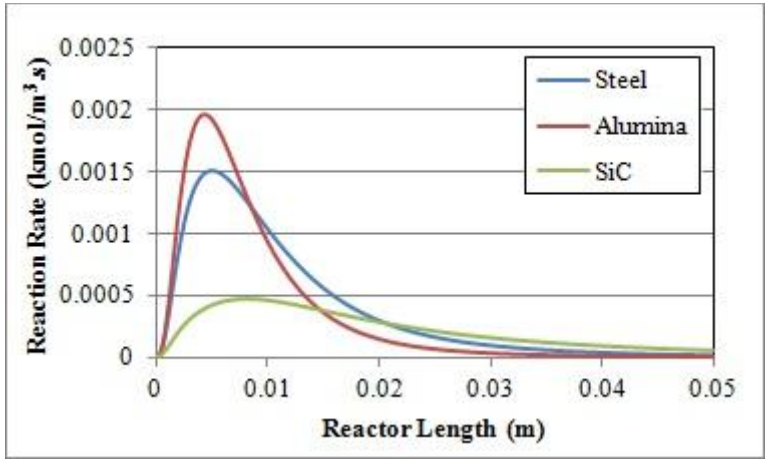

Figure A.57. Wall material comparison – Reaction rate of R7.

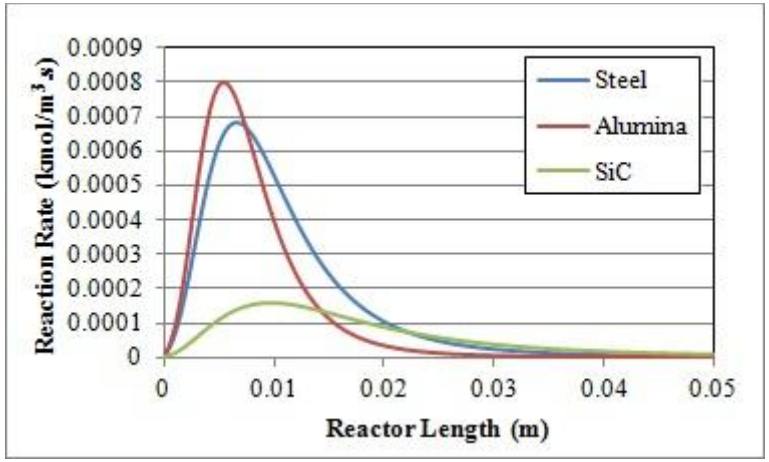

Figure A.58. Wall material comparison – Reaction rate of R8.

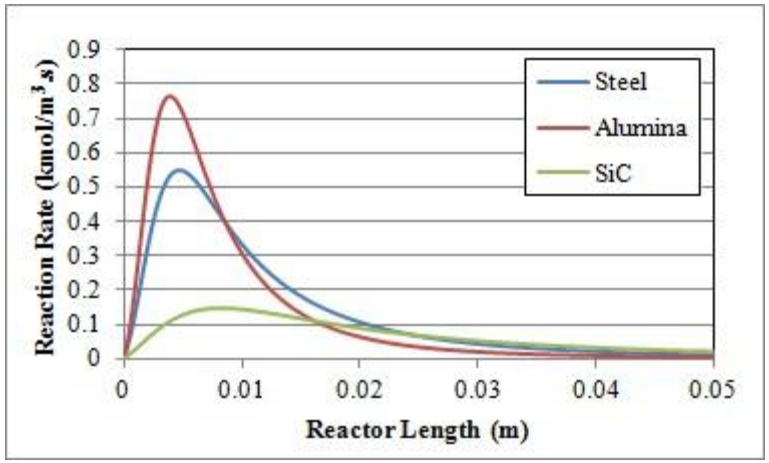

Figure A.59. Wall material comparison – Reaction rate of R9.

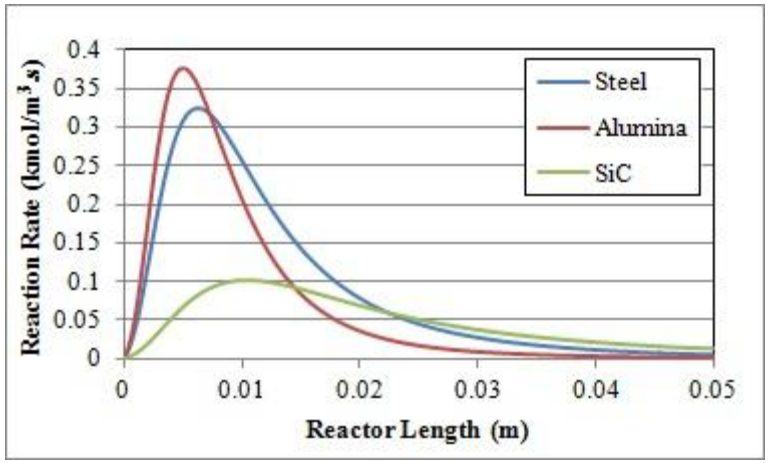

Figure A.60. Wall material comparison – Reaction rate of R10.

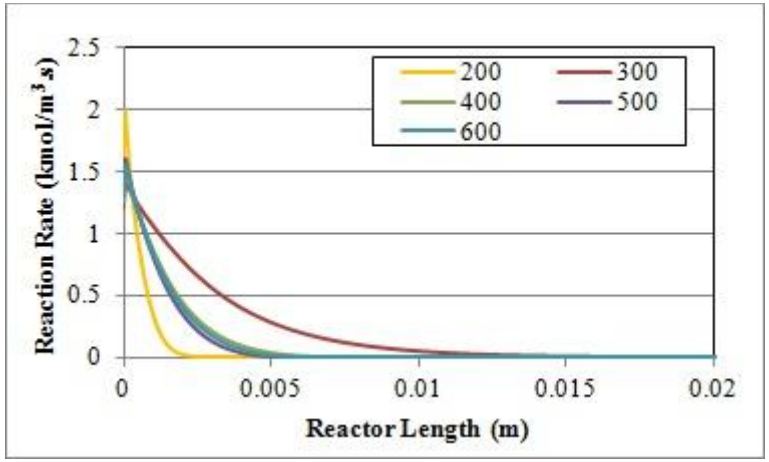

Figure A.61. Wall thickness comparison – Reaction rate of R1.

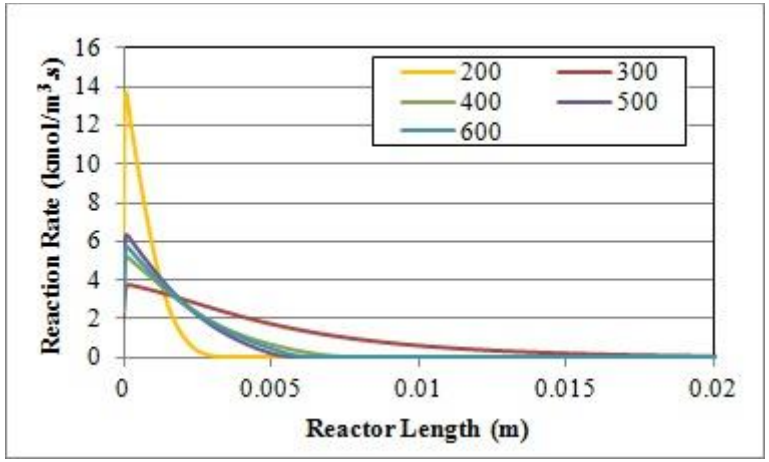

Figure A.62. Wall thickness comparison – Reaction rate of R2.

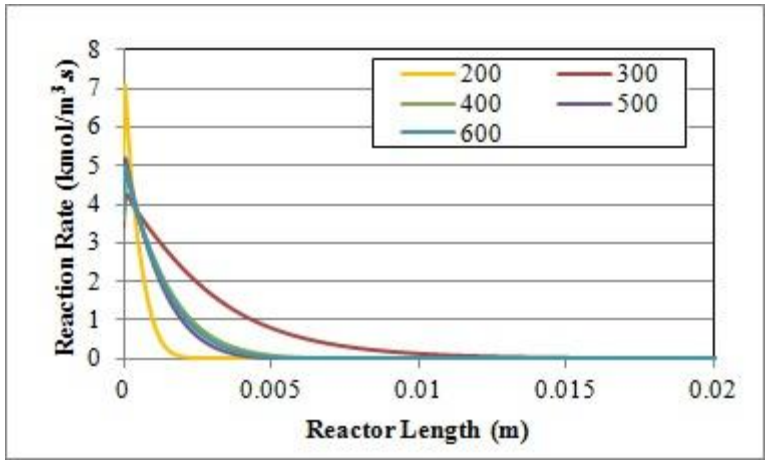

Figure A.63. Wall thickness comparison – Reaction rate of R3.

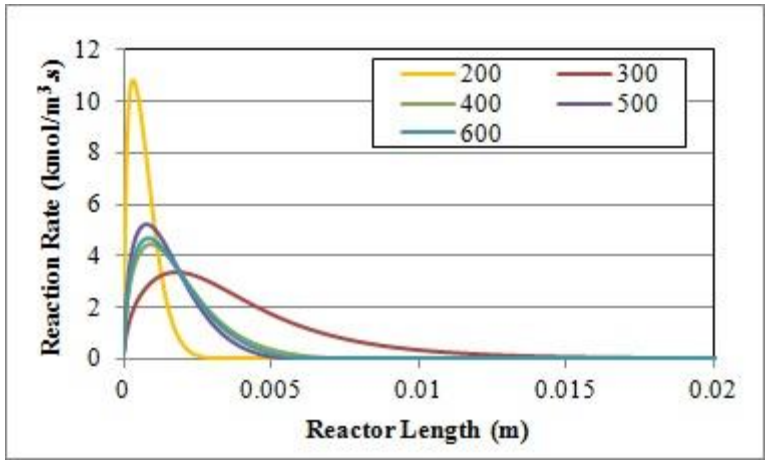

Figure A.64. Wall thickness comparison – Reaction rate of R4.

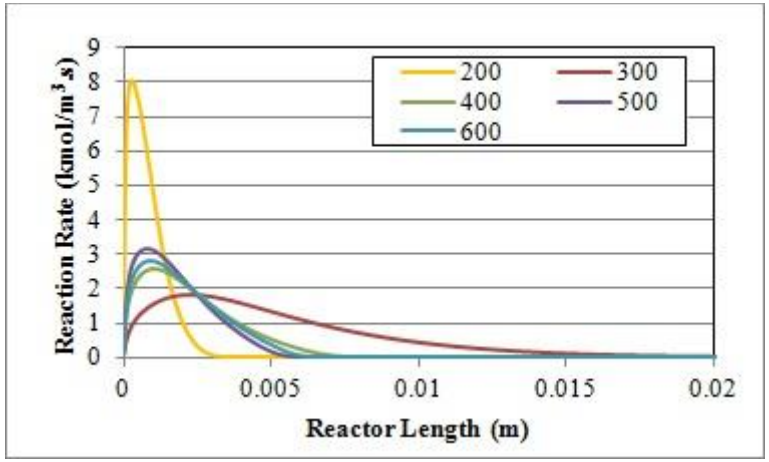

Figure A.65. Wall thickness comparison – Reaction rate of R5.

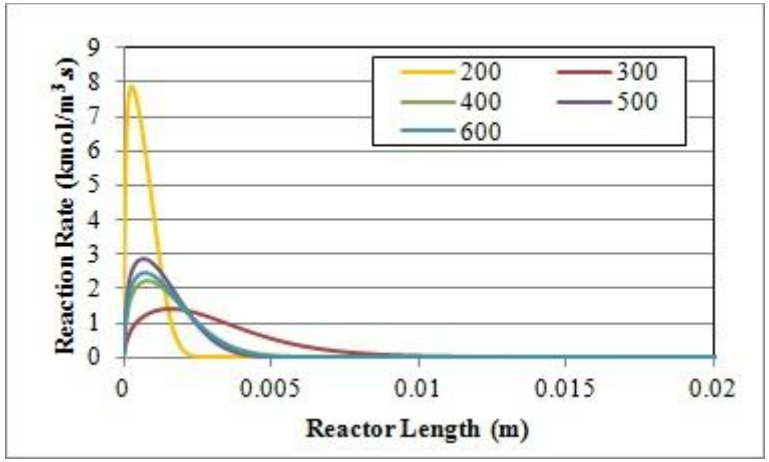

Figure A.66. Wall thickness comparison – Reaction rate of R6.

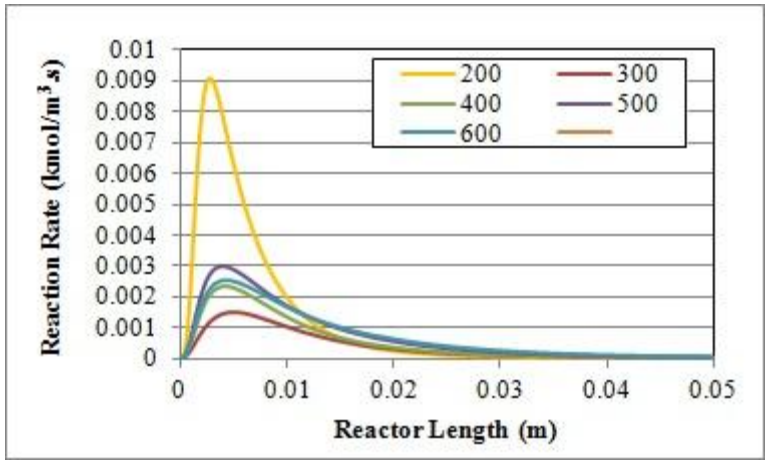

Figure A.67. Wall thickness comparison – Reaction rate of R7.

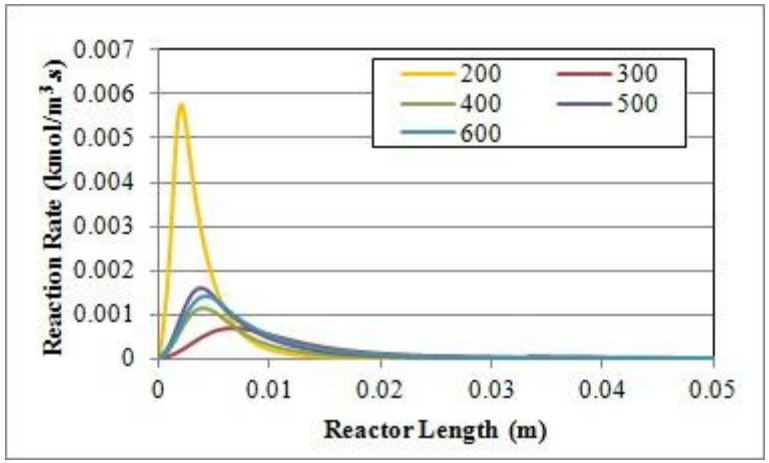

Figure A.68. Wall thickness comparison – Reaction rate of R8.

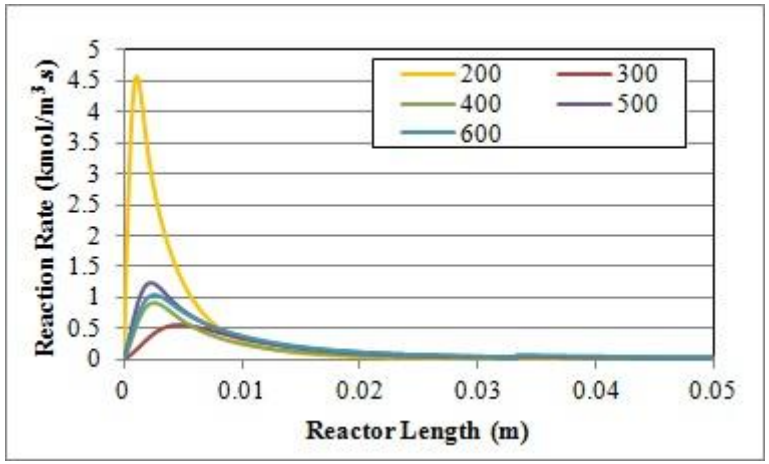

Figure A.69. Wall thickness comparison – Reaction rate of R9.

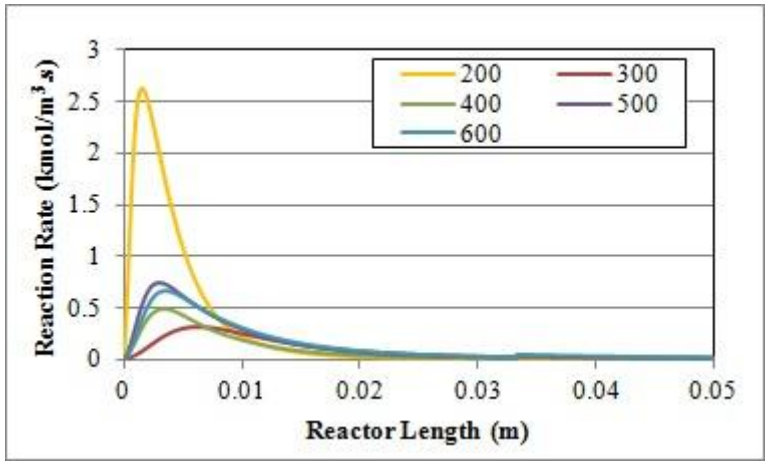

Figure A.70. Wall thickness comparison – Reaction rate of R10.

REFERENCES

1. Owen, N. A., O. R. Inderwildi and D. A. King, "The Status of Conventional World Oil Reserves-Hype or Cause for Concern?", *Energy Policy*, Vol. 38, pp. 4743-4749, 2010.

2. Baerns, M. and E. V. Kondratenko, *Handbook of Heterogeneous Catalysis*, 2nd Edition, Wiley-VCH, Section 13.17, pp. 3010-3023, 2008.

3. Ehrfeld, W., V. Hessel and V. Haverkamp, *Microreactors: New Technology for Modern Chemistry*, Wiley-VCH, 2001.

4. Charpentier, J.C., "In the Frame of Globalization and Sustainability, Process Intensification, a Path to the Future of Chemical and Process Engineering (Molecules into Money) ", *Chemical Engineering Journal*, Vol. 134, pp. 84-92, 2007.

5. Hessel, V., H. Löwe, A. Müller, G. Kolb, *Chemical Micro Process Engineering: Processes and Applications*, Wiley-VCH, 2005.

6. Kiwi-Minsker, L., A. Renken, "Microstructured Reactors for Catalytic Reactions", *Catalysis Today*, Vol. 110, pp. 2-14, 2005.

7. Buddoo, S., N. Siyakatshana, B. Zeelie, J. Dudas, "Study of the Pyrolysis of 2-Pinanol in Tubular and Microreactor Systems with Reaction Kinetics and Modeling", *Chemical Engineering and Processing*, Vol. 48, pp. 1419-1426, 2009.

8. Frauhammer, J., G. Kolios, G. Eigenberger, "Efficient Reactor Concepts for Coupling of Endothermic and Exothermic Reactions", *Chemical Engineering Science*, Vol. 57, pp. 1505-1510, 2002.

9. Karakaya, M., *Experimental and Quantitative Analysis of Multiphase Catalytic Reactions under Microfluidic Flow Conditions and Geometries*, PhD Thesis, Boğaziçi University, 2012.

10. Zanfir, M., A. Garviilidis, "Modelling of a Catalytic Plate Reactor for Dehydrogenation-Combustion Coupling", *Chemical Engineering Science*, Vol. 56, pp. 2671-2683, 2001.

11. Avci, A. K., G. Gümüşlü, "Parametric Analysis of Fischer-Tropsch Synthesis in a Catalytic Microchannel Reactor", *AIChE Journal*, Vol. 58, pp. 227-235, 2012.

12. Lerou, J.J., A. L. Tonkovich, L. Silva, S. Perry, J. McDaniel, "Microchannel Reactor Architecture Enables Greener Processes", *Chemical Engineering Science*, Vol. 65, pp. 380-385, 2010.

13. Keller, G. E., M. M., Bhasin, "Synthesis of Ethylene via Oxidative Coupling of Methane: I. Determination of Active Catalysts", *Journal of Catalysis*, Vol. 73, pp. 9-19, 1982.

14. Gesser, H.D., N.R. Hunter, "A review of C-1 Conversion Chemistry", *Catal. Today*, Vol.42, pp. 183–189, 1998.

15. Matherne, J. L., G. L. Culp, "Direct Conversion of Methane to C2's and Liquid Fuels Process Economics" in: E.E. World (Ed.) *Methane conversion by Oxidative Processes Fundamental and Engineering Aspects*, Van Nostrand Reinhold Catalysis Series, New York, pp. 463-482, 1992.

16. Schuurman, Y., T. Serres, L. Dreibine, "Synthesis of Enamel-Protected Catalysts for Microchannel Reactors: Application to Methane Oxidative Coupling", *Chemical Engineering Journal*, Vol. 213, pp. 31-40, 2012.

17. Iwamatsu, E., K-I. Aika, "Kinetic Analysis of the Oxidative Coupling of Methane Over Na+-Doped MgO", *Journal of Catalysis*, Vol. 117, pp. 416-431, 1989.

18. Lehmann, L., M. Baerns, "Kinetic Studies of the Oxidative Coupling of Methane Over a NaOH/CaO Catalyst", *Journal of Catalysis*, Vol. 135, pp. 467-480, 1992.

19. Stansch, Z., Mleczko, L., Baerns, M., "Comprehensive Kinetics of Oxidative Coupling of Methane over the La_2O_3/CaO Catalyst", *Ind. Eng. Chem. Res.*, Vol. 36 pp. 2568-2579, 1997.

20. Schweer, D., L. Mleczko, M. Baerns, "OCM in a Fixed-Bed Reactor: Limits and Perspectives", *Catal. Today*, Vol. 21, pp. 357-369, 1994.

21. Pannek, U., L. Mleczko, "Comprehensive Model of Oxidative Coupling of Methane in a Fluidized-Bed Reactor", *Chem. Eng. Sci.*, Vol. 51, pp. 3575-3590, 1996.

22. Pannek, U., L. Mleczko, "Effect of Scale-up on the Performance of a Fluidized-Bed Reactor for the Oxidative Coupling of Methane", *Chem. Eng. Sci*., Vol. 52, pp. 2429-2434, 1997.

23. Kruglov, A. V., C. M. Bjkorklund, R. W. Carr, "Optimization of the Simulated Countercurrent Moving Bed Chromatographic Reactor for the Oxidative Coupling of Methane", *Chemical Engineering Science*, Vol. 51, pp. 2945-2950, 1996.

24. Kao, Y.K., L. Lei, Y.S. Lin, "Effect of Scale-up on the Performance of a Fluidized-Bed Reactor for the Oxidative Coupling of Methane", *Ind. Eng. Chem. Res.*, Vol. 36, pp. 3583-3593, 1997.

25. Zeng, Y., Y. S. Lin, "Oxygen Permeation and Oxidative Coupling of Methane in Yttria Doped Bismuth Oxide Membrane Reactor", *Journal of Catalysis,* Vol.193, pp. 58-64, 2000.

26. Kiatkittipong, W., T. Tagawa, S. Goto, A. Assabumrungat, K. Silpasup, P. Praserthdam, "Comparative Study of Oxidative Coupling of Methane Modeling in Various Types of Reactor.", *Chemical Engineering Journal*, Vol. 115, pp. 63-71, 2005.

27. Tiemersma, T. P., A. S. Chaudhari, F. Galluci, J. A. M. Kuipers, M. Van Sint Annaland, "Integrated Autothermal Oxidative Coupling and Seam Reforming of

Methane. Part 1: Design of a Dual-Function Catalyst Particle", *Chemical Engineering Science,* Vol. 82, pp. 200-214, 2012.

28. Tiemersma, T. P., A. S. Chaudhari, F. Galluci, J. A. M. Kuipers, M. Van Sint Annaland, "Integrated Autothermal Oxidative Coupling and Steam Reforming of Methane. Part 2: Development of a Packed Bed Membrane Reactor with a Dual-Function Catalyst", *Chemical Engineering Science,* Vol. 82, pp. 232-245, 2012.

29. Yaws, C., *Yaws' Handbook of Thermodynamic Properties for hydrocarbons and Chemicals*, William Andrew, Norwich, New York, 2009.

30. Donald, A. N., A. Bejan, *Convection in Porous Media, 3rd edition,* Springer, New York, 2006.